Julius-Maximilians-
UNIVERSITÄT
WÜRZBURG

Graduate School
Science & Technology

Numerical Simulations of Heavy Fermion Systems: From He-3 Bilayers to Topological Kondo Insulators

Inaugural-Dissertation
zur Erlangung der Doktorwürde der
Graduate School of Science and Technology (GSST)
der
Julius-Maximilians-Universität Würzburg

Vorgelegt von M. Sc. Jan Werner
aus Würzburg
am 03. Dezember 2014

Julius-Maximilians-
UNIVERSITÄT
WÜRZBURG

Graduate School
Science & Technology

Gutachter/-innen / Mitglieder des Promotionskomitees

Vorsitzender des Promotionsprüfungsverfahrens:
Prof. Dr. Bernd Engels (Universität Würzburg)

Prüfer im Promotionskolloquium und Betreuer im Promotionskomitee:
1. Prüfer: *Prof. Dr. Fakher F. Assaad* (Universität Würzburg)
2. Prüfer: *Prof. Dr. Matthias Bode* (Universität Würzburg)
3. Prüfer: *PD Dr. Achim Schöll* (Universität Würzburg)

Gutachter der Dissertation:
1. Gutachter: *Prof. Dr. Fakher F. Assaad* (Universität Würzburg)
2. Gutachter: *Prof. Dr. Matthias Bode* (Universität Würzburg)

Tag des Promotionskolloquiums: 27. März 2015

Abstract

Even though heavy fermion systems have been studied for a long time, a strong interest in heavy fermions persists to this day. While the basic principles of local moment formation, Kondo effect and formation of composite quasiparticles leading to a Fermi liquid, are understood, there remain many interesting open questions. A number of issues arise due to the interplay of heavy fermion physics with other phenomena like magnetism and superconductivity.

In this regard, experimental and theoretical investigations of He-3 can provide valuable insights. He-3 represents a unique realization of a quantum liquid. The fermionic nature of He-3 atoms, in conjunction with the absence of long-range Coulomb repulsion, makes this material an ideal model system to study Fermi liquid behavior.

Bulk He-3 has been investigated for quite some time. More recently, it became possible to prepare and study layered He-3 systems, in particular single layers and bilayers. The possibility of tuning various physical properties of the system by changing the density of He-3 and using different substrate materials makes layers of He-3 an ideal quantum simulator for investigating two-dimensional Fermi liquid phenomenology.

In particular, bilayers of He-3 have recently been found to exhibit heavy fermion behavior. As a function of temperature, a crossover from an incoherent state with decoupled layers to a coherent Fermi liquid of composite quasiparticles was observed. This behavior has its roots in the hybridization of the two layers. The first is almost completely filled and subject to strong correlation effects, while the second layer is only partially filled and weakly correlated. The quasiparticles are formed due to the Kondo screening of localized moments in the first layer by the second-layer delocalized fermions, which takes place at a characteristic temperature scale, the coherence scale T_{coh}.

T_{coh} can be tuned by changing the He-3 density. In particular, at a certain critical filling, the coherence scale is expected to vanish, corresponding to a divergence of the quasiparticle effective mass, and a breakdown of the Kondo effect at a quantum critical point. Beyond the critical point, the layers are decoupled. The first layer is a local moment magnet, while the second layer is an itinerant overlayer.

However, already at a filling smaller than the critical value, preempting the critical point, the onset of a finite sample magnetization was observed. The character of this intervening phase remained unclear.

Motivated by these experimental observations, in this thesis the results of model calculations based on an extended Periodic Anderson Model are presented. The three particle ring exchange, which is the dominant magnetic exchange process in layered He-3, is included in

the model. It leads to an effective ferromagnetic interaction between spins on neighboring sites. In addition, the model incorporates the constraint of no double occupancy by taking the limit of large local Coulomb repulsion.

By means of Cellular DMFT, the model is investigated for a range of values of the chemical potential μ and inverse temperature $\beta = 1/T$. The method is a cluster extension to the Dynamical Mean-Field Theory (DMFT), and allows to systematically include non-local correlations beyond the DMFT. The auxiliary cluster model is solved by a hybridization expansion CTQMC cluster solver, which provides unbiased, numerically exact results for the Green's function and other observables of interest.

As a first step, the onset of Fermi liquid coherence is studied. At low enough temperature, the self-energy is found to exhibit a linear dependence on Matsubara frequency. Meanwhile, the spin susceptibility crossed over from a Curie-Weiss law to a Pauli law. Both observations serve as fingerprints of the Fermi liquid state.

The heavy fermion state appears at a characteristic coherence scale T_{coh}. This scale depends strongly on the density. While it is rather high for small filling, for larger filling T_{coh} is increasingly suppressed. This involves a decreasing quasiparticle residue $Z \sim T_{\text{coh}}$ and an enhanced mass renormalization $m^*/m \sim {T_{\text{coh}}}^{-1}$. Extrapolation leads to a critical filling, where the coherence scale is expected to vanish at a quantum critical point. At the same time, the effective mass diverges. This corresponds to a breakdown of the Kondo effect, which is responsible for the formation of quasiparticles, due to a vanishing of the effective hybridization between the layers.

Taking only single-site DMFT results into account, the above scenario seems plausible. However, paramagnetic DMFT neglects the ring exchange interaction completely. In order to improve on this, Cellular DMFT simulations are conducted for small clusters of size $N_c = 2$ and 3. The results paint a different physical picture. The ring exchange, by favoring a ferromagnetic alignment of spins, competes with the Kondo screening. As a result, strong short-range ferromagnetic fluctuations appear at larger values of μ. By lowering the temperature, these fluctuations are enhanced at first. However, for $T < T_{\text{coh}}$ they are increasingly suppressed, which is consistent with Fermi liquid coherence. However, beyond a certain threshold value of μ, fluctuations persist to the lowest temperatures. At the same time, while not apparent in the DMFT results, the total occupation n increases quite strongly in a very narrow range around the same value of μ. The evolution of n with μ is always continuous, but hints at a discontinuity in the limit $N_c \to \infty$. This first-order transition breaks the Kondo effect. Beyond the transition, a ferromagnetic state in the first layer is established, and the second layer becomes a decoupled overlayer.

These observations provide a quite appealing interpretation of the experimental results. As a function of chemical potential, the Kondo breakdown quantum critical point is preempted by a first-order transition, where the layers decouple and the first layer turns into a ferromagnet. In the experimental situation, where the filling can be tuned directly, the discontinuous transition is mirrored by a phase separation, which interpolates between the Fermi liquid ground state at lower filling and the magnetic state at higher filling. This is precisely the range of the intervening phase found in the experiments, which is characterized by an onset of a finite sample magnetization.

Besides the interplay of heavy fermion physics and magnetic exchange, recently the spin-orbit coupling, which is present in many heavy fermion materials, attracted a lot of interest. In the presence of time-reversal symmetry, due to spin-orbit coupling, there is the possibility of a topological ground state.

It was recently conjectured that the energy scale of spin-orbit coupling can become dominant in heavy fermion materials, since the coherence scale and quasiparticle bandwidth are rather small. This can lead to a heavy fermion ground state with a nontrivial band topology; that is, a topological Kondo insulator (TKI). While being subject to strong correlation effects, this state must be adiabatically connected to a non-interacting, topological state.

The idea of the topological ground state realized in prototypical Kondo insulators, in particular SmB_6, promises to shed light on some of the peculiarities of these materials, like a residual conductivity at the lowest temperatures, which have remained unresolved so far.

In this work, a simple two-band model for two-dimensional topological Kondo insulators is devised, which is based on a single Kramer's doublet coupled to a single conduction band. The model is investigated in the presence of a Hubbard interaction as a function of interaction strength U and inverse temperature β. The bulk properties of the model are obtained by DMFT, with a hybridization expansion CTQMC impurity solver. The DMFT approximation of a local self-energy leads to a very simple way of computing the topological invariant.

The results show that with increasing U the system can be driven through a topological phase transition. Interestingly, the transition is between distinct topological insulating states, namely the Γ-phase and M-phase. This appearance of different topological phases is possible due to the symmetry of the underlying square lattice. By adiabatically connecting both interacting states with the respective non-interacting state, it is shown that the transition indeed drives the system from the Γ-phase to the M-phase.

A different behavior can be observed by pushing the bare position of the Kramer's doublet to higher binding energies. In this case, the non-interacting starting point has a trivial band topology. By switching on the interaction, the system can be tuned through a quantum phase transition, with a closing of the band gap. Upon reopening of the band gap, the system is in the Γ-phase, i. e. a topological insulator. By increasing the interaction strength further, the system moves into a strongly correlated regime. In fact, close to the expected transition to the M phase, the mass renormalization becomes quite substantial. While absent in the paramagnetic DMFT simulations conducted, it is conceivable that instead of a topological phase transition, the system undergoes a time-reversal symmetry breaking, magnetic transition.

The regime of strong correlations is studied in more detail as a function of temperature, both in the bulk and with open boundary conditions. A quantity which proved very useful is the bulk topological invariant N_s, which can be generalized to finite interaction strength and temperature. In particular, it can be used to define a temperature scale T^* for the onset of the topological state. Rescaling the results for N_s, a nice data collapse of the results for different values of U, from the local moment regime to strongly mixed valence, is obtained. This hints at T^* being a universal low energy scale in topological Kondo insulators. Indeed, by comparing T^* with the coherence scale extracted from the self-energy mass renormalization, it is found that both scales are equivalent up to a constant prefactor. Hence, the scale T^* obtained from the temperature dependence of topological properties, can be used as an independent measure for Fermi liquid coherence. This is particularly useful in the experimentally relevant mixed valence regime, where charge fluctuations cannot be neglected. Here, a separation of the energy scales related to spin and charge fluctuations is not possible.

The importance of charge fluctuations becomes evident in the extent of spectral weight transfer as the temperature is lowered. For mixed valence, while the hybridization gap emerges, a substantial amount of spectral weight is shifted from the vicinity of the Fermi level to the lower Hubbard band. In contrast, this effect is strongly suppressed in the local moment regime.

In addition to the bulk properties, the spectral function for open boundaries is studied as a function of temperature, both in the local moment and mixed valence regime. This allows an investigation of the emergence of topological edge states with temperature. The method used here is the site-dependent DMFT, which is a generalization of the conventional DMFT to inhomogeneous systems. The hybridization expansion CTQMC algorithm is used as impurity solver.

By comparison with the bulk results for the topological quantity N_s, it is found that the temperature scale for the appearance of the topological edge states is T^*, both in the mixed valence and local moment regime.

Zusammenfassung

Obwohl Heavy-Fermion-Systemen bereits seit vielen Jahrzehnten intensiv untersucht werden, ist auch heute ein großes Interesse an Heavy Fermions vorhanden. Obwohl die grundlegenden Konzepte wie die Ausbildung lokaler Momente, der Kondo-Effekt und die zur Entstehung einer Fermi-Flüssigkeit führenden, kohärenten Quasiteilchen gut verstanden sind, gibt es weiterhin viele offene Fragestellungen. Diese ergeben sich u.a. aus dem Zusammenspiel von Heavy Fermions mit anderen Phänomenen wie Magnetismus und Supraleitung.

In dieser Hinsicht können Untersuchungen an He-3 sehr wertvolle Einsichten liefern. Das liegt darin begründet, dass He-3 eine einzigartige Realisierung einer Quanten-Flüssigkeit darstellt. Da He-3-Atome Fermionen sind, und da die langreichweitige Coulomb-Abstoßung keine Rolle spielt, ist dieses Material in idealer Weise dazu geeignet, um Fermi-Flüssigkeiten zu studieren.

In drei Dimensionen wird He-3 bereits seit Längerem untersucht. Vor Kurzem gelang es dann auch, Schichtsysteme aus He-3 zu erzeugen und zu untersuchen. Damit ergibt sich die Möglichkeit, die Phänomenologie zweidimensionaler Fermi-Flüssigkeiten detailliert zu untersuchen. He-3-Schichtsysteme stellen einen idealen Quanten-Simulator für diese Systeme dar, da sich durch Variation der He-3-Konzentration und durch die Wahl verschiedener Substratmaterialien unterschiedliche Eigenschaften der Fermi-Flüssigkeit gezielt einstellen lassen.

So wurde in He-3-Doppellagen ein Heavy-Fermion-Verhalten nachgewiesen. In Abhängigkeit der Temperatur wurde ein kontinuierlicher Übergang von einem inkohärenten Zustand mit entkoppelten Lagen zu einer kohärenten Fermi-Flüssigkeit aus Quasiteilchen mit gemischtem Charakter beobachtet. Dieses Verhalten hat seinen Ursprung in der Hybridisierung der beiden Lagen. Die erste Lage ist beinahe vollständig gefüllt und von starken Korrelationseffekten beeinflusst, während die zweite Lage nur teilgefüllt ist und Korrelationen eine geringe Rolle spielen. Die Quasiteilchen entstehen bei der Kondo-Abschirmung der lokalisierten Momente der ersten Lage durch die delokalisierten Fermionen der zweiten Lage, die bei einer charakteristischen Temperatur-Skala, der Kohärenz-Skala T_{coh} stattfindet.

Durch das Verändern der Dichte von He-3-Atomen lässt sich T_{coh} variieren. Dabei zeigte sich, dass bei einer kritischen Dichte ein Verschwinden der Kohärenzskala zu erwarten ist. Dies korrespondiert mit einer Divergenz der effektiven Masse der Quasiteilchen, und einem Zusammenbrechen des Kondo-Effekts an einem quantenkritischen Punkt. Jenseits dieses kritischen Punktes sind die Lagen vollständig entkoppelt. Die erste Lage ist ein Magnet von lokalen Momenten, während die zweite Lage einen itineranten Overlayer darstellt.

Allerdings wurde bereits bei einer Dichte, die kleiner ist als der kritische Wert, die Herausbildung einer endlichen Magnetisierung der Probe beobachtet. Der Charakter dieser Zwischenphase, die dem kritischen Punkt voraus geht, blieb allerdings ungeklärt.

In dieser Arbeit werden Resultate von Modellrechnungen eines erweiterten Periodischen Anderson Modell vorgestellt, die von den experimentellen Beobachtungen motiviert wurden. Dabei ist der Ringaustausch dreier Teilchen, also der dominante magnetische Austauschmechanismus in Schichtsystemen aus He-3, im Modell explizit enthalten. Dieser führt zu einer effektiv ferromagnetischen Wechselwirkung zwischen Spins auf benachbarten Gitterplätzen. Zudem berücksichtigt das Modell die Bedingung, dass keine Doppelbesetzung von Gitterplätzen auftritt, indem der Grenzfall einer sehr großen lokalen Coulomb-Abstoßung angenommen wird.

Mit Hilfe der Cellular DMFT wird das Modell als Funktion der Parameter chemisches Potential μ und inverse Temperature $\beta = 1/T$ untersucht. Diese Methode stellt eine Cluster-Erweiterung der Dynamical Mean-Field Theory (DMFT) dar, und erlaubt es, auf systematische Weise nichtlokale Korrelationen zu berücksichtigen, die über die DMFT-Approximation hinaus gehen. Für die Lösung der in jedem Iterationsschritt auftretenden Cluster-Modelle wird ein CTQMC-Cluster-Löser eingesetzt, der auf der Hybridisierungentwicklung basiert. Dieser liefert unverzehrte, numerisch exakte Ergebnisse für die Greensche Funktion und andere Observablen.

In einem ersten Schritt wird die Entstehung der kohärenten Fermi-Flüssigkeitsphase untersucht. Bei ausreichend tiefer Temperatur zeigt die Selbst-Energie in Matsubara-Frequenzen eine lineare Frequenzabhängigkeit. Gleichzeitig findet in der Spin-Suszeptibilität ein Übergang von einem Verhalten nach Curie-Weiss-Gesetz zu einem Pauli-Verhalten statt. Beide Beobachtungen sind eindeutige Hinweise auf einen Fermi-Flüssigkeitszustand.

Heavy Fermions bilden sich unterhalb der Kohärenz-Skala T_{coh} aus. Diese hängt stark von der He-3-Dichte ab. T_{coh} ist bei kleiner Füllung recht hoch, wird bei größerer Füllung allerdings zunehmend unterdrückt. Dies bedingt ein abnehmendes Quasiteilchen-Gewicht $Z \sim T_{\mathrm{coh}}$ und eine zunehmende Massenrenormierung $m^*/m \sim {T_{\mathrm{coh}}}^{-1}$. Durch Extrapolation erhält man einen quantenkritischen Punkt, an dem die Kohärenzskala verschwindet. Gleichzeitig divergiert hier die effektive Masse. Dies entspricht dem Zusammenbrechen des Kondo-Effekts, der für die Entstehung der Quasiteilchen verantwortlich ist, da die effektive Hybridisierung zwischen den Lagen verschwindet.

Berücksichtigt man nur Ergebnisse von paramagnetischer DMFT, so erscheint das obige Szenario plausibel. Allerdings wird in diesem Fall der Ringaustausch komplett vernachlässigt. Um diese Situation zu verbessern, werden Simulationen mit Hilfe von Cellular DMFT an kleinen Clustern der Größen $N_c = 2$ and 3 durchgeführt. Die Ergebnisse zeichnen ein anderes physikalisches Bild. Der Ringaustausch konkurriert mit der Kondoabschirmung der lokalen Momente, da er eine ferromagnetische Ausrichtung der Spins bevorzugt. Daraus resultieren auf kurzen Längenskalen für steigendes μ starke ferromagnetische Fluktuationen. Mit sinkender Temperatur werden diese zunächst verstärkt, dann für $T < T_{\mathrm{coh}}$ allerdings zunehmend unterdrückt. Dies ist konsistent mit einer kohärenten Fermi-Flüssigkeit. Bei Überschreiten eines gewissen Schwellwertes für μ bestehen die starken Fluktuationen bis zu den tiefsten Temperaturen, die in der Simulation erreicht wurden. Gleichzeitig, zeigt sich ein starker Anstieg der Gesamtbesetzung n in einem engen Fenster um denselben Schwellwert von μ. Dieses Verhalten fehlt in den DMFT-Resultaten vollständig. Die Entwicklung von n mit μ ist stets kontinuierlich, weist allerdings auf eine Diskontinuität im Grenzfall $N_c \to \infty$ hin. Dieser Übergang erster Ordnung lässt den Kondo-Effekt abrupt zusammenbrechen. Jenseits des Übergangs ist in der ersten Lage ein ferromagnetischer Zustand ausgebildet, während die zweite Lage ein davon entkoppelter Overlayer wird.

Diese Ergebnisse erlauben eine sehr überzeugende Interpretation der experimentellen Resultate. Als Funktion des chemischen Potentials findet vor dem erwarteten quantenkritische Punkt des Zusammenbrechens des Kondo-Effekts ein Übergang erster Ordnung statt, bei dem die Lagen entkoppeln, und in der ersten Lage ein ferromagnetischen Zustand entsteht. Im Experiment wird allerdings direkt die Füllung eingestellt. In dieser Situation tritt anstelle des diskontinuierlichen Phasenübergang eine Phasenseparation auf, die zwischen dem Grundzustand einer Fermi-Flüssigkeit bei niedrigerer Dichte und dem magnetischen Zustand bei größerer Dichte interpoliert. Dieser Bereich ist aber gerade die im Experiment beobachtete Zwischenphase, die durch die Ausbildung einer endlichen Probenmagnetisierung charakterisiert ist.

Neben dem Zusammenspiel von Heavy Fermions und magnetischem Austausch erregte die Spin-Bahn-Kopplung, die in vielen Heavy-Fermion-Materialien relevant ist, ein zunehmendes Interesse. Bei Vorliegen von Zeitumkehr-Symmetrie ergibt sich aufgrund von Spin-Bahn-Kopplung die Möglichkeit eines topologischen Grundzustandes.

Kürzlich wurde daher vermutet, dass Spin-Bahn-Kopplung in Heavy-Fermion-Materialien eine dominante Rolle spielt, da die Kohärenzskala und die Breite der Quasiteilchen-Bänder sehr klein sind. Dies kann zu einem Grundzustand von Heavy Fermions mit einer nicht-trivialen Topologie der Bandstruktur führen, also einem topologischen Kondo-Isolator. Obwohl dieser Zustand von starken Korrelationseffekte gekennzeichnet ist, muss er dennoch adiabatisch mit einem nichtwechselwirkenden, topologischen Zustand verbunden sein.

Die Idee, dass ein topologischer Grundzustand in typischen Kondo-Isolatoren realisiert sein könnte, insbesondere in SmB_6, lässt hoffen, dass sich dadurch einige Eigenheiten dieser Materialien erklären lassen. So zeigen einige dieser Materialien eine Rest-Leitfähigkeit bei sehr tiefen Temperaturen, die sich bisher nicht erklären ließ.

In dieser Arbeit wird ein einfaches Zwei-Band-Modell für topologische Kondo-Isolatoren in zwei Dimensionen entwickelt, das auf einem Kramerschen Dublett aufbaut, das an lediglich ein Leitungsband gekoppelt ist. Dieses Modell wird als Funktion der Stärke der Hubbard-

Wechselwirkung U und der inversen Temperatur β untersucht. Die Bulk-Eigenschaften des Modells werden mit Hilfe von DMFT untersucht, mit einem CTQMC-Störstellen-Löser auf Basis der Hybridisierungsentwicklung. Dabei ergibt sich aufgrund der Approximation einer lokalen Selbst-Energie eine sehr einfache Möglichkeit, die topologische Invariante zu berechnen.

Die Ergebnisse zeigen, dass das System mit steigendem U einen topologischen Phasenübergang durchläuft. Interessanterweise findet der Übergang zwischen unterschiedlichen topologischen Zuständen statt, nämlich zwischen der Γ-Phase und der M-Phase. Das Auftreten verschiedener topologischer Phasen wird durch die Symmetrie des zugrundeliegenden Quadratgitters bedingt. Indem die beiden Zustände mit Wechselwirkungen adiabatisch mit den jeweiligen nichtwechselwirkenden Zuständen verbunden werden, ist gezeigt, dass der wechselwirkungsgetriebene Phasenübergang tatsächlich von der Γ-Phase zur M-Phase führt.

Ein anderes Verhalten kann beobachtet werden, wenn die energetische Lage des Kramerschen Dubletts zu größeren Bindungsenergien verschoben wird. In diesem Fall weist der nichtwechselwirkende Startpunkt eine topologisch triviale Bandstruktur auf. Durch das Einschalten der Wechselwirkung kann das System durch einen Quanten-Phasenübergang geführt werden, bei dem sich die Bandlücke schließt. Nach dem erneuten Öffnen der Bandlücke befindet sich das System allerdings in der Γ-Phase, d.h. in einem topologisch nichttrivialen Zustand. Wird die Stärke der Wechselwirkung weiter erhöht, bewegt sich das System in ein stark korreliertes Regime. Tatsächlich ist die Massenrenormierung in der Nähe des erwarteten Übergangs zur M-Phase sehr groß. Daher ist es vorstellbar, dass anstelle des erwarteten topologischen Phasenübergangs eine Brechung der Zeitumkehr-Symmetrie aufgrund eines magnetischen Übergangs stattfindet, auch wenn dies in paramagnetischen DMFT-Simulationen nicht realisiert ist.

Das Regime starker Korrelationen wird in Abhängigkeit von der Temperatur näher untersucht, sowohl im Bulk als auch mit offenen Randbedingungen. Eine in diesem Zusammenhang sehr nützliche Größe ist die topologische Invariante N_s, die sich auf wechselwirkende Systeme bei endlicher Temperatur verallgemeinern lässt. Insbesondere lässt sich damit eine Temperaturskala T^* definieren, die das Entstehen des topologischen Zustandes als Funktion der Temperatur beschreibt. Durch Reskalieren der Ergebnisse für N_s wird ein guter Datenkollaps der Resultate für unterschiedliche Werte von U erreicht, die sich vom Regime lokaler Momente bis hin zu stark gemischter Valenz erstrecken. Dies deutet darauf hin, dass T^* eine universelle Niederenergieskala in topologischen Kondo-Isolatoren ist. Tatsächlich zeigt ein Vergleich von T^* mit der Kohärenzskala, die sie aus der Massenrenormierung aufgrund der Selbst-Energie ergibt, dass beide Skalen bis auf einen konstanten Faktor äquivalent sind. Daher kann T^*, dass sich aus der Temperaturabhängigkeit topologischer Eigenschaften ableitet, als unabhängige Größe für die Kohärenz einer Fermi-Flüssigkeit herangezogen werden. Dies erweist sich im experimentell relevanten Regime gemischter Valenz als besonders nützlich, wo

Ladungsfluktuationen nicht vernachlässigt werden können. Eine Separation der Energieskalen von Ladungs- und Spinfluktuationen ist in diesem Fall anders nicht möglich.

Die Bedeutung von Ladungsfluktuationen zeigt sich in dem Ausmaß des Transfers von spektralem Gewicht, der beim Absinken der Temperatur stattfindet. Bei gemischter Valenz wird mit der Ausbildung der Hybridisierungslücke ein erheblicher Anteil spektralen Gewichts aus der Umgebung der Fermienergie in das untere Hubbard-Band verschoben. Im Regime lokaler Momente ist dieser Effekt hingegen stark unterdrückt.

Neben Bulk-Eigenschaften wird die Spektralfunktion bei offenen Rändern als Funktion der Temperatur untersucht, sowohl für lokale Momente als auch gemischte Valenz. Dadurch lässt sich die Entstehung topologischer Randzustände als Funktion der Temperatur studieren. Die hier eingesetzte Methode ist die gitterplatzabhängige DMFT. Diese ist eine Erweiterung der DMFT auf inhomogene Systeme. Zudem wird hier erneut ein Störstellen-Löser auf Basis der Hybridisierungsentwicklung eingesetzt.

Ein Vergleich der so erzielten Ergebnisse mit den Bulk-Resultaten für die topologische Größe N_s zeigt, dass die Temperaturskala für das Auftreten der topologischen Randzustände gerade T^* ist, sowohl für lokale Momente als auch gemischte Valenz.

Contents

1 Models and Numerical Methods for Heavy Fermions

1.1 Heavy Fermions

1.1.1 Introduction

Strongly correlated electron systems have attracted a lot of interest over the last decades. Heavy fermions are a particular class of systems, where the strong renormalization of quasiparticles due to interactions leads to interesting phenomena.

In heavy fermion materials, the result of strong correlation effects is an effective quasiparticle mass, which is orders of magnitude larger than the mass of a free electron or band electrons in conventional metals [48].

As a consequence of this large mass renormalization, the energy scale at which heavy fermion physics comes into play, the coherence scale T_{coh} is very low. While T_{coh} is the only low-temperature scale in heavy fermions, which results in universal behavior of physical observables, at higher temperatures other energy scales can come into play. Out of this, a complicated temperature dependence of physical properties results, which reflects the different energy scales dominating in different temperature regimes.

In Sec. 1.1.2, the basics of Fermi liquid theory are presented. It provides a remarkably accurate description of the properties of many metals, and serves as the basic concept to build on in the subsequent sections. This is followed in Sec. 1.1.3 by a discussion of the Kondo effect. This phenomenon gives rise to the interesting properties of heavy fermions. The most important aspects of heavy fermions are reviewed in Sec. 1.1.4. Finally, in Sec. 1.1.5 the Periodic Anderson Model is introduced as the principal model for the microscopic description of heavy fermion systems.

1.1.2 Fermi Liquid Theory

In the absence of interactions, a macroscopic ensemble of fermions comprises a Fermi gas. It is governed only by an external potential and fermionic statistics: Due to the Pauli exclusion principle, two or more particles are forbidden to occupy the same state. For temperature T and chemical potential μ, a state with energy ε is occupied with probability

$$n(\varepsilon) = \left(1 + \exp\left(\frac{\varepsilon - \mu}{k_B T}\right)\right)^{-1} = f(\varepsilon), \tag{1.1.1}$$

i. e. according to the Fermi-Dirac distribution $f(\varepsilon)$. Hence, at zero temperature, all states up to the Fermi energy $E_F = \mu(T = 0)$, i. e. with momentum k smaller than the Fermi momentum k_F, are occupied. In vacuum, the wavefunctions Ψ are plane waves with momentum k and a quadratic dispersion $\varepsilon(k)$

$$\begin{aligned}\Psi_k(r,t) &= \exp\left(i\,k\,r - i\,\varepsilon(k)\,t\right) \\ \varepsilon(k) &= \frac{\hbar k^2}{2m}\end{aligned} \tag{1.1.2}$$

In the case of electrons in a solid, due to the periodic potential of the ions, $\varepsilon(k)$ is no longer the free dispersion, but depends on the microscopic details of the system. The wavefunctions are Bloch waves

$$\Psi_k(r,t) = u_k(r)\exp\left(i\,k\,r - i\,\varepsilon(k)\,t\right), \tag{1.1.3}$$

where $u_k(r)$ has the periodicity of the lattice, and crystal momentum k is only defined modulo a reciprocal lattice vector [53].

What happens when interactions between electrons are introduced? By slowly increasing the interaction strength U according to

$$U(t) = U\exp\left(\eta t\right)$$

such that $U(-\infty) = 0$, and η is positive and infinitesimally small, in the absence of electronic phase transitions, the system adiabatically evolves from the non-interacting Fermi gas state at $t = -\infty$ to the fully interacting state at $t = 0$; that is, a Fermi liquid [75]. This concept of *adiabatic continuity* [6] provides a one-to-one correspondence between the low-energy Fermi liquid states and the original states. Landau-Fermi liquid theory rests precisely on this concept. It predicts that due to the adiabatic evolution of states, many aspects of the Fermi gas carry over to the Fermi liquid, even in the presence of strong Coulomb interactions, which is quite remarkable.

The low-energy excitations of a Fermi liquid are dressed particles or quasiparticles. However, in contrast to the elementary excitations of the non-interacting system, quasiparticles are well-defined only in the vicinity of the Fermi energy [75]. The reason is that a quasiparticle excited to an energy $\varepsilon > E_f$, due to the limited phase space available for scattering, has an inverse lifetime $\tau^{-1} \sim (\varepsilon - E_f)^2$. Hence, the excitations are long-lived only around the Fermi energy. In terms of the fermionic self-energy Σ, this means that the imaginary part, which encodes the lifetime, vanishes like $\mathrm{Im}[\Sigma(\omega)] \sim \omega^2$.

Two of the physical observables most often employed to study Fermi liquid behavior are the specific heat c_V and the static, uniform magnetic susceptibility χ. For a Fermi gas, both quantities are directly related to the density of states at the Fermi energy $A(E_F)$ [75]

$$\begin{aligned} c_V &= \left(\frac{\partial E}{\partial T}\right)_N = \gamma T = \underbrace{\frac{\pi^2}{3} A(E_F)\, k_B^2}_{\gamma} T \qquad (1.1.4) \\ \chi &= \frac{\partial M}{\partial B} = \mu_B^2 A(E_F) \\ \text{where} \quad A(E_F) &= \frac{m k_F}{\pi^2 \hbar^2}. \end{aligned}$$

Hence, the specific heat is linear in temperature, with the Sommerfeld coefficient γ, and the susceptibility is a temperature-independent constant.

In a Fermi liquid, the quasiparticles are subject to a mass renormalization, and acquire an effective mass m_{eff}. The mass renormalization brings about a number of important consequences for physical observables, since [24]

$$\begin{aligned} m_{\text{eff}} &= m\,(1 + F_1^s) \qquad (1.1.5) \\ \Rightarrow A(E_F) &\rightarrow A(E_F)\, \frac{m_{\text{eff}}}{m} \\ c_V &\rightarrow c_V\, \frac{m_{\text{eff}}}{m} \\ \chi &\rightarrow \chi\, \frac{m_{\text{eff}}}{m}\, \frac{1}{1 + F_0^a}. \end{aligned}$$

Hence, the specific heat is still linear in temperature, but reflects the mass renormalization. Meanwhile the spin susceptibility remains a constant. In the above expressions, the Landau parameters $F_l^{s/a}$ arise due to a multipole expansion of the interaction, and describe the renormalization [75]. The superscripts s and a denote contributions symmetric and antisymmetric in spin.

In addition, Fermi liquid theory predicts a quadratic dependence of the electrical resistivity on temperature due to electron-electron scattering, i. e. $\rho \approx \rho_0 + aT^2$, which results from the same phase space argument used to derive the quasiparticle lifetime. A constant contribution from scattering of nonmagnetic impurities is denoted by ρ_0.

The quasiparticle renormalization is equally reflected in the momentum-dependent spectral function $A(k, \omega)$ [24]. For a Fermi gas, $A(k, \omega) = \delta(\omega - \varepsilon_k)$ is a delta function. With interactions, the delta peak transforms into a coherent quasiparticle peak, with a width in accordance with the finite lifetime, and an incoherent background. The weight of the quasiparticle peak is the quasiparticle residue $Z = \dfrac{m}{m_{\text{eff}}} < 1$. In terms of the self-energy, this quantity reads

$$Z = \left(1 - \frac{d\ \mathrm{Re}[\Sigma(\omega)]}{d\omega}\bigg|_{\omega = 0}\right)^{-1} \qquad (1.1.6)$$

Hence, the slope of the real part of the self-energy around $\omega = 0$ reflects the mass renormalization.

Without interaction, the momentum distribution function at zero temperature

$$n(k) = \int_{-\infty}^{0} d\omega \, A(k,\omega) \tag{1.1.7}$$

exhibits a jump of magnitude one at the Fermi momentum $k = k_F$, i. e. at the Fermi surface. This fact is simply a result of the singularity of the Fermi-Dirac distribution at zero temperature, i. e. $\lim_{T\to 0} f(\varepsilon) = \Theta(E_F - \varepsilon)$. In the Fermi liquid, the discontinuity is still present, there is still a Fermi surface, but the size of the jump is reduced to $Z < 1$.

Finally, the Luttinger sum rule, which reflects the fact that the volume enclosed by the Fermi surface measures the particle number, is invariant while adiabatically transitioning from the non-interacting Fermi gas to the interacting Fermi liquid [24]. This results from the one-to-one correspondence between bare particles and quasiparticles, i. e. adiabatic continuity.

The characteristic temperature for the appearance of Fermi liquid behavior is the coherence scale T_{coh}. In a non-interacting Fermi gas, T_{coh} is simply the Fermi temperature $T_F = k_B^{-1} E_F$. In the interacting case T_{coh} is suppressed, since $T_{\text{coh}} \sim Z$. Therefore, Fermi liquid behavior is only observed at sufficiently low temperature $T < T_{\text{coh}}$.

1.1.3 Local Moment Physics and the Kondo Effect

The Kondo effect is at the heart of heavy fermion physics. The term describes the spin-flip scattering of conduction electrons off localized magnetic moments [61]. This process can occur e.g. in a metal with conduction band states derived from s-orbitals or p-orbitals, which hybridize with d-orbitals or f-orbitals from dilute magnetic impurities, like transition metals or lanthanides.

The impurity orbitals act as isolated, local moment. Since charge fluctuations, i. e. hopping of electrons from the impurity into the host band and back are frozen, the only remaining degree of freedom is the electron's spin [24]. A model description for local moment formation and the Kondo effect is provided by the Single Impurity Anderson Model (SIAM) [5]. In second quantized form it reads

$$\hat{\mathcal{H}}_{\text{SIAM}} = \underbrace{\sum_{k,\sigma} \varepsilon_c(k)\, \hat{c}^{\dagger}_{k,\sigma}\hat{c}_{k,\sigma}}_{\text{conduction band}} + \underbrace{\sum_{\sigma} \varepsilon_0\, \hat{f}^{\dagger}_{\sigma}\hat{f}_{\sigma} + U\, \hat{n}_{f,\uparrow}\hat{n}_{f,\downarrow}}_{\text{impurity orbital}} + \underbrace{\sum_{\sigma} V\left(\hat{c}^{\dagger}_{0,\sigma}\hat{f}_{\sigma} + h.c.\right)}_{\text{hybridization}}. \tag{1.1.8}$$

Here $\varepsilon_c(k)$ is the dispersion of the conduction band states $\hat{c}_{k,\sigma}$, while ε_0 is the orbital energy of the impurity orbital state f_σ, where σ is the spin. U is a local Coulomb repulsion, $\hat{n}_{f,\sigma} = \hat{f}^{\dagger}_{\sigma}\hat{f}_{\sigma}$

the density of impurity electrons, and V the hybridization amplitude between the impurity orbital and conduction band state at the location of the impurity $r = 0$.

The energy scale associated with the hybridization is $\Delta = \pi V^2 A(E_F)$ [48]. In the Kondo regime, i. e. for

$$-\varepsilon_0 \gg \Delta \text{ and } \varepsilon_0 + U \gg \Delta, \tag{1.1.9}$$

transitions to the unoccupied and doubly occupied state are blocked. Virtual processes lead to an effective, antiferromagnetic coupling J_K between the impurity spin $\hat{\mathrm{S}}$ and the conduction electron spin $\hat{\mathrm{s}}_0$ at site 0, which is captured in the Kondo model

$$\hat{\mathcal{H}}_{\text{Kondo}} = \sum_{k,\sigma} \varepsilon_c(k)\, \hat{\mathrm{c}}^\dagger_{k,\sigma} \hat{\mathrm{c}}_{k,\sigma} + J_K\, \hat{\mathrm{S}} \circ \hat{\mathrm{s}}_0. \tag{1.1.10}$$

Formally, the Kondo model can be obtained from the SIAM in the Kondo limit Eq. (1.1.9) by a Schrieffer-Wolf transformation [48]. In particular, the Kondo coupling J_K reads

$$J_K = V^2 \left(\frac{1}{\varepsilon_0 + U} + \frac{1}{-\varepsilon_0} \right).$$

The magnetic susceptibility of local moments is given by the Curie-Weiss law

$$\chi(T) \sim \frac{1}{T + \theta}, \tag{1.1.11}$$

where θ is the Weiss temperature, which is a phenomenological parameter describing the interaction between spins. Positive θ corresponds to antiferromagnetic coupling, while for $\theta < 0$ the susceptibility diverges at $T = -\theta$ due to ferromagnetic interactions. A Curie-Weiss magnetic susceptibility is a clear signature of the formation of local moments.

The spin-flip scattering mechanism, encoded in the Kondo model (1.1.10) by the antiferromagnetic exchange J_K, screens the magnetic moments and results in the formation of a composite fermion or Kondo singlet of localized impurity orbital and conduction electrons. As exemplified in the SIAM (1.1.8) and Kondo model (1.1.10), the hybridization or interaction between impurity and conduction electrons is restricted to the site of the local moment. Hence, the Kondo effect is local in space, and arises only due to dynamical fluctuations.

The characteristic temperature for the formation of the Kondo singlet is the single impurity Kondo temperature T_K. As a consequence of the Kondo effect, as a function of decreasing temperature, the electrical resistivity of the host metal exhibits a minimum. The behavior results from the impurity scattering, which gives rise to a logarithmic term $\rho \sim \log(1/T)$. This term counters the T^2 behavior predicted by Fermi liquid theory, which results in the minimum.

In fact, a more involved calculation reveals that the logarithmic divergence of the resistivity is avoided as $T \to 0$ due to the complete screening of the magnetic moments. Since impurities, being magnetic initially, act more and more like potential scatterers, eventually they contribute a constant, i. e. temperature independent term to the resistivity [124].

1.1.4 Heavy Fermion Metals and Kondo Insulators

In certain compounds, the approximation of dilute, isolated impurities giving rise to the Kondo effect, is not justified anymore. As the concentration of localized orbitals increases, one can imagine at every impurity site a composite fermion is formed by the Kondo effect. The scattering at the impurities takes place in an increasingly coherent fashion [24], giving rise to a highly renormalized band of width $\tilde{T}_K$, the lattice Kondo temperature. Indeed, a Fermi liquid state is realized. Hence, one can associate $\tilde{T}_K$ with the coherence temperature T_{coh} of the Fermi liquid.

The heavy fermion state arises due to the interplay between delocalized degrees of freedom and a dense arrangement of localized, strongly interacting degrees of freedom. In heavy fermion compounds, the former are usually conduction electrons, which are formed from extended atomic p- or d-orbitals, while the latter are usually derived from f-orbitals. In most cases, these orbitals originate from rare-earth elements, in particular Ce, which have partially filled 4f shells [101].

In a mean-field picture, as shown in Fig. 1.1.1 the hybridization between the flat f-band and the strongly dispersing conduction band leads to two heavy bands separated by a gap of order T_{coh}.

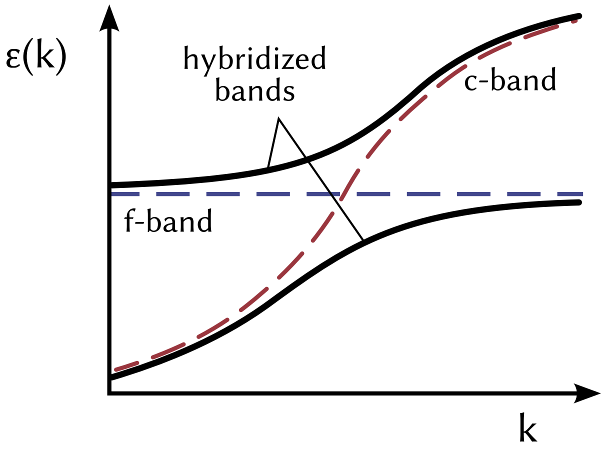

Figure 1.1.1: Schematic mean-field band structure of heavy fermions. The flat f-band and the conduction band (c-band) hybridize, forming two bands separated by a small band gap, which become very flat in the vicinity of the gap. Figure adapted from Ref. 24.

Even though the quasiparticles are strongly renormalized, in the temperature range below the coherence scale T_{coh}, the heavy fermion state still exhibits the hallmark features of a Fermi liquid; that is, a linear in temperature specific heat and a constant magnetic susceptibility.

However, T_{coh} can be very low compared to the Fermi temperature of metals, i. e. conventional Fermi liquids. Therefore, the effective quasiparticle mass $m_{\text{eff}} \sim 1/T_{\text{coh}}$ is of the order of 100-1000 bare electron masses. This enormous mass renormalization becomes apparent from the Sommerfeld coefficient $\gamma \sim m_{\text{eff}}$, which can amount to more than 1000 mJ/(mol K^2) in heavy fermion materials [101], in contrast to single digit values for conventional metals.

In many heavy fermion materials, the chemical potential is located inside the heavy quasiparticle band. Hence, they are metals, but the relevant charge carriers are heavy fermions. Prominent examples include $CeAl_3$, $CeCu_6$, UBe_{13}, and UPt_3 [101].

In contrast, for integer filling, i. e. when the chemical potential is located inside the band gap between the heavy bands, a so-called Kondo insulator or heavy fermion semiconductor is realized. This class of materials includes compounds like SmB_6, YbB_{12}, CeNiSn and $Ce_3Bi_4Pt_3$ [1]. These materials exhibit an intriguing crossover from metallic to insulating, with the crossover temperature scale being the coherence scale T_{coh}. This behavior can be understood from the temperature-dependent formation of the hybridization gap, which separates the heavy bands, and which develops with the onset of heavy fermion coherence.

Besides the Kondo interaction between conduction electrons and localized electrons, other types of interactions can influence the behavior of heavy fermions. Of particular importance is magnetic exchange between f-electrons. A magnetic ion induces Friedel oscillations in the density of conduction electron spins. A second ion can couple to these oscillations [24], establishing an effective exchange interaction between the two ions, the Ruderman-Kittel-Kasuya-Yosida (RKKY) interaction. It can be either ferromagnetic or antiferromagnetic, depending on the microscopic details, but is usually of the latter type. The RKKY energy scale is $T_{\text{RKKY}} \sim J_K^2 A_c(E_F)$, where $A_c(E_F)$ is the density of states of conduction electrons. T_{RKKY} favors a singlet of f-electrons, and therefore competes with the Kondo temperature $T_K \sim \exp\left((-2\, J_K\, A_c(E_F))^{-1}\right)$, which favors a Kondo singlet. Depending on the value of $J_K\, A_c(E_F)$, Kondo lattice coherence ($T_K > T_{\text{RKKY}}$) or antiferromagnetic order ($T_{\text{RKKY}} > T_K$) is realized [28]. Indeed, in some heavy fermion materials, the true ground state is a magnetic state [101], with the Kondo effect broken by antiferromagnetic exchange.

A phase transition at a zero temperature quantum critical point (QCP) separates the heavy fermion phases from the antiferromagnet or spin-density wave. Meanwhile, the Kondo effect is broken down in the magnetic phase. The hybridization between conduction band and f-band vanishes, while simultaneously the effective quasiparticle mass diverges. Hence, the f-electrons localize completely, resulting in a transition from a large volumen of the Fermi surface – including conduction and f-electrons – to small volume, counting only conduction electrons.

In the context of the competition between frustration, either geometrical or due to competing interactions, and Kondo effect, it is debated, whether magnetic transition, i. e. to an antiferromagnet, and localization transition, i. e. Kondo breakdown and Fermi surface transition, coincide due to so-called local quantum criticality. In a different perspective, the two transitions are decoupled, with two distinct QCPs present in the system. Therefore, either an orbital-selective Mott transition to a state without magnetic order, i. e. a quantum spin liquid state, or a coexistence of antiferromagnetism and Kondo effect is possible [25, 96, 97, 109, 127].

The schematic phase diagram provided in Fig. 1.1.2 summarizes the discussion about heavy fermion systems. The two different perspectives of adiabatic continuity (horizontal) and temperature dependent crossover (vertical) both reappear in the second part of the thesis.

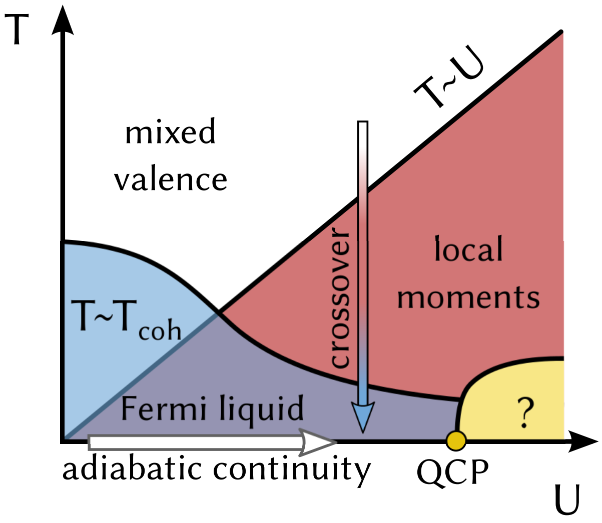

Figure 1.1.2: Phase diagram of heavy fermions, with temperature T and interaction strength U. In the weak-coupling regime, charge fluctuations prevail, while in the strong-coupling local moment regime spin fluctuations are dominant. The heavy Fermi liquid is adiabatically connected to the non-interacting state. In addition, as a function of temperature, a series of crossovers leads to a complicated temperature dependence of physical properties (vertical arrow). For strong interactions, a QCP might appear. Beyond the QCP, different phases are possible, which is denoted by the question mark. Figure adapted from Ref. 24.

1.1.5 Periodic Anderson Model

1.1.5.1 A Model for Heavy Fermions

The Periodic Anderson Model (PAM) is one of the principal models for the investigation of heavy fermion systems. It represents a generalization of the SIAM to a periodic array of impurities, and is able to capture many aspects of Fig. 1.1.2.

In the PAM, two bands of very different character are coupled by a hybridization term: On the one hand there is a conduction band of delocalized, weakly correlated fermions, on the other hand there is a band of almost localized, strongly interacting fermions. In second quantization, the model reads

$$\begin{aligned} \hat{\mathcal{H}}_{\mathrm{PAM}} &= \hat{\mathcal{H}}_c + \hat{\mathcal{H}}_f + \hat{\mathcal{H}}_{cf} + \hat{\mathcal{H}}_I \\ \hat{\mathcal{H}}_c &= \sum_{k,\sigma} \varepsilon_c(k)\, \hat{\mathrm{c}}^\dagger_{k,\sigma}\hat{\mathrm{c}}_{k,\sigma} \\ \hat{\mathcal{H}}_f &= \sum_{k,\sigma} \varepsilon_0\, \hat{\mathrm{f}}^\dagger_{k,\sigma}\hat{\mathrm{f}}_{k,\sigma} \\ \hat{\mathcal{H}}_{cf} &= \sum_{k,\sigma} V(k)\, \hat{\mathrm{c}}^\dagger_{k,\sigma}\hat{\mathrm{f}}_{k,\sigma} + h.c. \\ \hat{\mathcal{H}}_I &= \sum_{i} U\, \hat{\mathrm{n}}_{f,i,\uparrow}\hat{\mathrm{n}}_{f,i,\downarrow} \end{aligned} \tag{1.1.12}$$

The operator $\hat{\mathrm{c}}^\dagger_{k,\sigma}$ creates a fermion of momentum k and spin σ in the conduction band with dispersion $\varepsilon_c(k)$, while $\hat{\mathrm{f}}^\dagger_{k,\sigma}$ creates a fermion in the strongly correlated, flat band with energy ε_0. The c-fermions are uncorrelated, while f-fermions interact locally on each site i via a Hubbard interaction U. The hybridization Hamiltonian $\hat{\mathcal{H}}_{cf}$ describes the mixing between the two fermion species.

The PAM in the formulation of Eq. (1.1.12) is closely related to another prototypical model for strongly correlated systems: The Kondo lattice model (KLM). It is obtained in the Kondo limit, where the f-orbitals reside well below the conduction band, while the local Hubbard repulsion is much larger than the bandwidth (c.f. Eq. (1.1.9))

$$\hat{\mathcal{H}}_{\mathrm{KLM}} = \sum_{k,\sigma} \varepsilon_c(k)\, \hat{\mathrm{c}}^\dagger_{k,\sigma}\hat{\mathrm{c}}_{k,\sigma} + \sum_{i} J\, \hat{\mathrm{S}}_i \circ \hat{\mathrm{s}}_i \tag{1.1.13}$$

Here all the charge fluctuations on the f-sites are frozen out. The model describes a conduction band, where the conduction electron spin $\hat{\mathrm{s}}_i$ at site i interacts locally via a Kondo coupling with an impurity spin $\hat{\mathrm{S}}_i$. The coupling strength is $J > 0$ for antiferromagnetic, or less common $J < 0$ for ferromagnetic exchange.

1.1.5.2 Generalization to Multiple Bands and General Interactions

In many cases, the two-band formulation of the PAM is not sufficient to describe the physics of realistic materials. In this situation a generalization to multiple bands and more complicated, in general non-local interaction terms is necessary. In order to facilitate the discussion in the second part of this work, a more general model is proposed here.

The model is formulated in terms of N_c conduction bands, with the c-fermions acquiring an additional band index m, and N_f localized f-orbitals, with an orbital index α, which are closely related to atomic orbitals. In addition a finite, but usually small overlap of f-orbitals at different sites is allowed for, which results in a finite dispersion of the f-bands. Finally, a very general expression for the interaction is used to include correlations beyond the local Hubbard term. The different parts of the generalized Hamiltonian read

$$\begin{aligned}
\hat{\mathcal{H}}_c &= \sum_{m,k} \hat{\mathrm{c}}^\dagger_{k,m}\, t^{(c)}_m(k)\, \hat{\mathrm{c}}_{k,m} \qquad (1.1.14)\\
\hat{\mathcal{H}}_f &= \sum_{\alpha,\beta} \hat{\mathrm{f}}^\dagger_{k,\alpha}\, t^{(f)}_{\alpha,\beta}(k)\, \hat{\mathrm{f}}_{k,\beta}\\
\hat{\mathcal{H}}_{cf} &= \sum_{k,m,\alpha} \hat{\mathrm{c}}^\dagger_{k,m}\, V_{m,\alpha}(k)\, \hat{\mathrm{f}}_{k,\alpha} + h.c.\\
\hat{\mathcal{H}}_I &= \sum_{\substack{k,p,q\\ \alpha,\beta,\gamma,\delta}} U_{\alpha\beta\gamma\delta}(k,p,q)\, \hat{\mathrm{f}}^\dagger_{\alpha,k+q} \hat{\mathrm{f}}^\dagger_{\beta,p-q} \hat{\mathrm{f}}_{\delta,p} \hat{\mathrm{f}}_{\gamma,k}
\end{aligned}$$

The generalized dispersions $t^{(c)}_m(k)$ and $t^{(f)}_{\alpha,\beta}(k)$ contain both on-site energies for the different orbitals at the same site, as well as the dispersion arising from hopping processes between orbitals at different sites. The hybridization has become a matrix in band and orbital space.

The non-interacting part of the Hamiltonian can be conveniently written in a matrix-vector notation,

$$\hat{\mathcal{H}} = \sum_k \begin{pmatrix} \hat{\mathrm{c}}^\dagger_k & \hat{\mathrm{f}}^\dagger_k \end{pmatrix} \begin{pmatrix} t^{(c)}(k) & V(k) \\ V^\dagger(k) & t^{(f)}(k) \end{pmatrix} \begin{pmatrix} \hat{\mathrm{c}}_k \\ \hat{\mathrm{f}}_k \end{pmatrix} + \hat{\mathcal{H}}_I \qquad (1.1.15)$$

where $\hat{\mathrm{c}}_i = (\hat{\mathrm{c}}_{i,1}, \ldots, \hat{\mathrm{c}}_{i,N_c})$ and $\hat{\mathrm{f}} = (\hat{\mathrm{f}}_1, \ldots, \hat{\mathrm{f}}_{N_f})$. The PAM (1.1.12) is recovered for $N_c = N_f = 2$ for the two spin directions, a dispersionless f-band, a spin-diagonal hybridization of f-fermions and c-fermions, and a momentum independent, i. e. local interaction.

Different interaction terms supplementing the local Hubbard repulsion are conceivable, in particular non-local terms. The most straightforward addition is a density-density repulsion term between different orbitals on the same or neighboring sites, like in the extended Hubbard model. In real-space, it reads

$$\hat{\mathcal{H}}_I = \underbrace{\sum_i U^{(1)}_{\alpha,\beta} \hat{\mathrm{n}}_{f,i,\alpha} \hat{\mathrm{n}}_{f,i,\beta}}_{\text{interorbital repulsion}} + \underbrace{\sum_{\langle i,j\rangle} U^{(2)}_{\alpha,\beta} \hat{\mathrm{n}}_{f,i,\alpha} \hat{\mathrm{n}}_{f,j,\beta}}_{\text{intersite repulsion}}$$

At rather large values of U, the double occupancy of individual orbitals is suppressed. Effective non-local magnetic interactions are dynamically generated [79] via virtual processes, like the direct exchange between neighboring sites, the RKKY interaction discussed above or ring-exchange processes. The corresponding interaction can be described by a Heisenberg term

$$\hat{\mathcal{H}}_I = \sum_{i,j} J_{i,j}\, \hat{\mathrm{S}}_i \hat{\mathrm{S}}_j. \tag{1.1.16}$$

Depending on the number of sites involved, J is either negative, leading to ferromagnetic exchange, or positive, for antiferromagnetic exchange.

1.1.5.3 Phenomenology

The PAM (1.1.12) has been studied extensively in the context of heavy fermions [48]. In exploring the phase diagram, one can take different perspectives. The first is the adiabatic approach. Here, starting from the uncorrelated case at zero temperature, the interactions are gradually increased, with the system evolving accordingly. For $U = 0$, the hybridization of the two bands leads to the formation of two hybridized bands (c.f. Fig. 1.1.1). Gradually switching on the interaction, bare particles evolve into renormalized quasiparticles, and the bands become increasingly flat around the band gap [24]. At the same time, the size of the hybridization gap decreases, reflecting the mass renormalization.

The second perspective explores the temperature dependence of the system from high to low temperatures. In the process, depending on the model parameters, the system exhibits a quite remarkable behavior. For $-\varepsilon_0 \gg \Delta$ and $U + \varepsilon_0 \gg \Delta$, i. e. in the Kondo regime, local moments form at a crossover scale $\sim U$ [24]. The impurity orbitals are occupied by one electron almost all the time. The energy barrier to the unoccupied and doubly occupied states is so large that charge fluctuations are almost completely frozen out. The particles, which reside in the impurity orbitals, are therefore only characterized by their spin. As the temperature is lowered, due to the Kondo effect, the local moments and conduction electrons start to hybridize, forming composite quasiparticles. The quasiparticles become coherent at even lower temperatures $T \sim T_{\mathrm{coh}}$, giving rise to a Fermi liquid state, and a well-defined hybridization gap. Due to the clear separation of energy scales, the different regimes can be easily identified in physical observables like the magnetic susceptibility: The local moment regime is dominated by the Curie-Weiss behavior of f-electrons, while the coherent Fermi liquid exhibits a constant Pauli susceptibility.

Moving away from the Kondo regime to mixed valence by letting either ε_0 or $\varepsilon_0 + U$ approach the hybridization scale, charge fluctuations become increasingly important. Hence, the f-electrons form incomplete local moments at a lower temperature, while the temperature for Fermi liquid coherence is higher. In this situation, which is relevant for heavy fermion materials like SmB_6 [87], disentangling the two energy scales becomes increasingly difficult.

1.2 Topological Insulators

1.2.1 Basic Notions of Topological States

Many heavy fermion compounds contain rare-earth elements, where spin-orbit coupling can play an important role. In this context, the idea of topological Kondo insulators was brought forward, which combines the physics of topological insulators with heavy fermions. To facilitate the discussion on topological Kondo insulators in the second part of the thesis, here the notion of topological states of matter is introduced, and properties of topological insulators and topological invariants for these states are discussed. In the following, the general aspects of the topological insulator (TI) is introduced for the non-interacting case. However, in many cases, generalization to correlated TIs.

In the conventional Ginzburg-Landau theory of phase transitions, different phases are characterized in terms of broken symmetries, with a corresponding vanishing or finite value of the respective order parameter [4]. As an example, an antiferromagnetic phase is distinct from a paramagnetic phase due to the breaking of translational symmetry. The order parameter, which vanishes in the paramagnet, but is finite in the antiferromagnet, is the staggered magnetisation

$$m(q) = \sum_{i,j} \exp\left(i\, q\, (r_i - r_j)\right)(\hat{\mathrm{n}}_{i,\uparrow} - \hat{\mathrm{n}}_{j,\downarrow}) \tag{1.2.1}$$

Here, q is the ordering vector, where $q = (\pi, \pi)$ corresponds to the Néel antiferromagnet on a square lattice.

As it turns out, not all the different phases realized in nature can be differentiated in this scheme. Beyond the Landau theory, this brings about the notion of topological order [43]. In the sense of topology, states are equivalent when they can be continuously transformed into one another. As an example, the conventional band insulator can be transformed into an atomic insulator by appropriately increasing the lattice spacing, such that the lattice sites eventually become isolated atoms.

A topological classification of states depends only on global properties, while local details have no influence. Smooth deformations of the state cannot change the global properties, i. e. the topological character [85].

Time-reversal invariant insulators permit such a topological classification. In two and three spatial dimensions, all such states can be grouped according to a $\mathbb{Z}_2$ classification, with a topological invariant ν [94]. While a trivial band insulator is characterized by $\nu = 0$, the topological insulator (TI) has $\nu = 1$. This state is hence topologically distinct from the band insulator. The TI as an insulator has a bulk band gap. However, a transformation from the TI to the band insulator is only possible via a quantum phase transition, where the band gap closes.

1.2.2 Properties of Topological Insulators

1.2.2.1 Time-reversal Symmetry

The topological insulator is protected by time-reversal symmetry. The time-reversal operation can be written as an antiunitary operator $\hat{\Theta}$,

$$\hat{\Theta} = \exp\left(i\pi\,\hat{S}_y\right)\hat{K}. \tag{1.2.2}$$

$\hat{K}$ is the operator for complex conjugation, and $\hat{S}_y$ is the y-component of the spin. It follows that $\hat{\Theta}^2 = -1$ for spin-1/2 fermions. A Hamiltonian, which is invariant under time-reversal symmetry, has to obey

$$\hat{\Theta}\,\hat{\mathcal{H}}(k)\,\hat{\Theta}^{-1} = \hat{\mathcal{H}}(-k). \tag{1.2.3}$$

Therefore, the eigenstates have to be at least doubly degenerate [43]. In a conventional, time-reversal invariant band insulator, this so-called Kramer's theorem corresponds to the degeneracy of up- and down-spins.

Special points in the Brillouin zone, the time-reversal invariant momenta Γ_i, are mapped onto themselves by the application of $\hat{\Theta}$. On a square lattice, these are the points Γ, M, X and Y. At the Γ_i there have to be two degenerate states, which are time-reversal conjugate partners.

1.2.2.2 Topological Edge States

Since the TI is distinct from the trivial band insulator, at an interface to a trivial insulator or at the surface – the interface to vacuum – the topological character of the state changes. Hence, there has to be a closing of the band gap at the surface, which results in a metallic surface state. Indeed, due to the so-called bulk-boundary correspondence, the topological insulator in n-dimensional space gives rise to robust, gapless surface states in (n-1) dimensions [85]. In this sense, the edge states are "holographic", since they can only exist on the edge of a higher-dimensional topological insulator. They are exponentially localized, and can be described by an effective helical edge theory [85]. The protection of the time-reversal symmetry makes the edge states stable against disorder or weak interaction effects [85].

The quantum spin Hall effect is an example for the unique properties of topological states. It was first realized experimentally in HgCdTe quantum well structures [62]. The edge states of a quantum spin Hall insulator, which is a two-dimensional topological insulator, are helical, i. e. spin and momentum are tightly locked. Therefore, backscattering is suppressed. As a result, transport along the edge channels is ballistic, with each channel contributing a conductance quantum $G_0 = e^2/h$.

Because of time-reversal symmetry, the Hall conductance is zero, since the Hall effect of up and down spins cancel. In contrast, the spin Hall conductance is quantized. This means that the transport properties are directly related to the topological properties of the system. The conductance is hence non-local, and independent on the sample geometry [89]. The notion of local transport, which is the basis of Ohm's law, does not hold in these systems.

1.2.2.3 Models for Topological Insulators

In the presence of spin conservation, the quantum spin Hall state can be understood as two time-reversal conjugate copies of the quantum Hall (QH) state, one for each spin orientation. This construction restores time-reversal symmetry, which is broken in the QH state. It is employed in deriving the Kane-Mele model for graphene with spin-orbit coupling [56, 57], where the QSH effect was proposed. In its simplest form, it reads

$$\hat{\mathcal{H}}_{\mathrm{KM}} = t \sum_{\langle i,j\rangle,\sigma} \hat{c}_i^\dagger \hat{c}_j + i\lambda \sum_{\langle\langle i,j\rangle\rangle} \nu_{ij}\, \hat{c}_i^\dagger\, \sigma_z\, \hat{c}_j. \tag{1.2.4}$$

Here, the $\hat{c}_i$ are two-component spinors at lattice site i. The second term is a next-nearest neighbor hopping term, where $\nu_{ij} = \pm 1$ depending on whether the hopping is clockwise or counterclockwise. This term encodes the spin-orbit coupling.

Another model to describe prototypical topological insulators is the Bernevig-Hughes-Zhang (BHZ) model for HgTe quantum wells [17]. It represents a two-band model with spin-orbit coupling, which can be written as

$$\hat{\mathcal{H}}_{\mathrm{BHZ}} = \sum_k \begin{pmatrix} \hat{c}_{k,1}^\dagger & \hat{c}_{k,2}^\dagger \end{pmatrix} \begin{pmatrix} h(k) & 0 \\ 0 & h^\dagger(-k) \end{pmatrix} \begin{pmatrix} \hat{c}_{k,1} \\ \hat{c}_{k,2} \end{pmatrix} \tag{1.2.5}$$

$$\text{where} \quad h(k) = \Big(m - \cos(k_x) - \cos(k_y)\Big)\, \sigma_z + \lambda \Big(\sin(k_x)\, \sigma_x + \sin(k_y)\, \sigma_y\Big).$$

The Hamiltonian is constructed in a such way, that the lower right 2×2 block is related to the upper left block by application of the time-reversal operator, i. e. they are Kramer's conjugate.

1.2.3 Topological Invariant

1.2.3.1 Topological Invariants for the Quantum Spin Hall State

To characterize topological states, the notion of a global topological invariant is employed, in contrast to the conventional, local order parameters. A topological invariant takes only integer values, and cannot change continuously as a function of parameters. In the case of the QH insulator, the topological invariant is the Chern number or TKNN invariant [43] defined by

$$C_{1,m} = \frac{1}{2\pi} \int_{\mathrm{BZ}} d^2k\, F_m(k) \quad \in \mathbb{Z} \tag{1.2.6}$$

where $F_m(k)$ is the Berry flux associated with the Bloch state in band m with momentum k, and the integral runs over the whole Brillouin zone. Since the Chern number is defined by an integration, local changes to the system cannot change the topological properties. The quantized value of the Hall conductance σ_{xy} is directly related to $C_1 = \sum_m C_{1,m}$, i. e. C_1 counts the number of edge channels.

In contrast, the topological insulator is characterized by the $\mathbb{Z}_2$ topological invariant ν, which is zero for a trivial band insulator, and one for a topological insulator.

In a QSH insulator, the total Chern number is zero due to time-reversal symmetry

$$C_1 = C_{1,\uparrow} + C_{1,\downarrow} = 0$$

However, being essentially two copies of the QH state, one can define the spin Chern number $C_s = 1/2(C_{1,\uparrow} - C_{1,\downarrow})$, which is non-zero. In this case, the $\mathbb{Z}_2$ topological invariant ν is given by $\nu = C_s \mod 2$, since an even number of edge channels yields a trivial insulator, while an odd number is necessary for a topological insulator.

So far, the definition of the topological invariants relied on Bloch states. While Eq. (1.2.6) can be generalized to systems with interactions, the evaluation can be cumbersome or even not possible [49]. However, by defining the topological invariant in terms of the Green's function, one can readily extend the concept to interacting systems [113, 115]. For the two-dimensional case, a topological invariant can be defined via

$$N_2 = \frac{1}{24\pi^2} \int dk_0\, d^2k\, \mathrm{tr}\left[\varepsilon^{\kappa\lambda\rho} G\partial_{k_\kappa} G^{-1}\, G\partial_{k_\lambda} G^{-1}\, G\partial_{k_\rho} G^{-1}\right]. \tag{1.2.7}$$

Here $\varepsilon^{\kappa\lambda\rho}$ is the fully antisymmetric tensor, $k_0 = i\omega$ is the imaginary frequency, and summation over repeated indices $\kappa, \lambda, \rho = 0, 1, 2$ is implied. In fact, one can show that $N_2 = C_1$ [115].

Based on N_2, and similar in spirit to C_s, a topological invariant N_s of the quantum spin Hall state can be defined as

$$N_s = \sum_\sigma \frac{\sigma}{2} N_{2,\sigma}. \tag{1.2.8}$$

However, as N_s is given in terms of the Green's functions, it can be readily generalized to correlated systems. With interactions, it retains its topological character as long as there is an adiabatical connnection to the non-interacting case [20, 41].

The notion of topological states and topological invariants is rigorously defined only at $T = 0$. At finite temperatures, the expression for N_s can take arbitrary real values, and approaches zero as $T \to \infty$. Nevertheless, as discussed in the second part of this thesis, it can be used to quantify the emergence of the topological state as the temperature is lowered.

The above method of calculating topological invariants can be simplified by noting that only the zero-frequency Green's function is necessary for the topological classification [116]. This can be most easily visualized in the form of the so-called topological Hamiltonian [114]. This auxiliary Hamiltonian describes the system in terms of its topological character. The topological Hamiltonian is given by

$$h_{\mathrm{topo}}(k) = -G^{(-1)}(k, i\omega = 0) = h(k) + \Sigma(k, i\omega = 0), \tag{1.2.9}$$

and is hence completely determined by the single-particle part of the Hamiltonian and the self-energy at zero frequency. It is suitable to obtain the correct topological invariant, however it should not be confused with an effective quasiparticle Hamiltonian [114].

In the presence of inversion symmetry [34], it is only necessary to consider the parity eigenvalues δ at the time-reversal invariant momenta Γ_i

$$\begin{aligned} (-1)^{\nu} &= \prod_i \delta_i \qquad (1.2.10) \\ \text{where} \quad \delta_i &= \prod_m \xi_{2m}(\Gamma_i). \end{aligned}$$

m is a band index, and $\xi_{2m}(\Gamma_i)$ is a corresponding parity eigenvalue at Γ_i.

As a remark, in three spatial dimensions, there is not one, but four topological invariants $\nu_\alpha = (\nu_0, \nu_1, \nu_2, \nu_3)$, where $\nu_0 = \prod_{i=1}^{8} \delta_i$ is the strong invariant, while the other three are weak invariants constructed from a subset of the parities δ_i.

1.2.3.2 Space-group Classification of Topological Insulators

With the investigation of topological phases in prototypical models, it became clear that not only time-reversal symmetry, but also lattice symmetries play a role in determining topological properties. In particular, the lattice symmetry gives rise to additional topological phases and indices, which are related to the high-symmetry points.

In Ref. 55, two distinct topological phases of the BHZ model were discussed, the so-called Γ-phase and M-phase. They differ not only in the parities at the Γ and M point, but also in physical properties. Indeed, it was found that a lattice dislocation can act as a π-flux in the M-phase, which is not the case in the Γ-phase.

In Ref. 99 this result was generalized. For every group of equivalent high-symmetry points, there is an associated phase, which can have trivial or non-trivial topological properties. Considering the square lattice, in addition to the trivial band insulator, there are three phases. These are the topological Γ-phase and M-phase, as well as the trivial X-Y-phase.

In fact, it was already recognized in Ref. 34 that with inversion symmetry the individual parity eigenvalues δ_i become gauge independent, and hence topological invariants. Without breaking time-reversal symmetry, a parity δ_i can only change via a band gap closing at the corresponding high-symmetry point Γ_i.

1.2.4 Interacting Topological Insulators

The interplay of topology and correlation effects is a very active field of research [49], even though topological states are to some extent robust against correlation effects. As was discussed in the previous section, the notion of topological states and topological invariants can be carried over to systems with interaction effects. In particular, the prototypical lattice models for topological insulators have been studied in the presence of correlation effects. The Kane-Mele model supplemented by a Hubbard interaction term was found to exhibit a transition from a quantum spin Hall state to an antiferromagnetic state at intermediate couplings, thereby breaking time-reversal symmetry [19, 50, 51]. With the inclusion of long-range Coulomb interactions, the critical interaction strength, where the transition is located, is significantly enhanced [52], but the general phase diagram remains unchanged.

Different possible mechanisms for topological phase transitions driven by interactions have been discussed [41, 110]. While weak interactions can drive a quantum phase transition from a normal to topological band insulator via a mean-field like energy level shift, i. e. a band renormalization, transitions can equally result from strong correlations. Since for an interacting system the topological invariant $\nu = \gamma C_s$ [110], where γ is the frequency-domain winding number and C_s the spin Chern number, in this case, the strong frequency dependence of the self-energy can result in a trivial state, i. e. $\nu = 0$, even though $C_s \neq 0$.

In studies of the correlated BHZ model, such topological phase transitions were equally observed. For a Hubbard interaction, within the DMFT approximation a possible first-order transition from a topological insulator to Mott insulator was found [129]. With the possibility of symmetry-breaking, an antiferromagnetic phase is realized, which might even coexist with the topological phase [130]. The inclusion of the full Hund's rule instead of only density-density interactions shifts the critical interaction strength for the Mott transition to lower values [21].

In related studies, an interaction-driven phase transition from the conventional band insulator to the topological insulator could be realized [21, 111].

1.3 Dynamical Mean-Field Theory

1.3.1 Introduction

The idea of a classical mean-field theory is very appealling. Instead of solving a complicated many-particle problem, which is almost always intractable, one approximates the interaction of a particle with other particles by an effective, average potential [4]. Hence, every particle feels the presence of the other particles in its neighborhood only via this effective field which is obtained from a self-consistency condition by minimizing the free energy.

This simplifies the many-particle problem to a single-particle problem with an effective, self-consistent potential. In addition, at least in classical physics, by scaling the model parameters appropriately, mean-field theory becomes exact in the limit of an infinite number of neighboring sites, because spatial fluctuations can be neglected in this limit.

In quantum physics, not only spatial fluctuations, but also purely quantum mechanical fluctuations in imaginary time come into play. While the spatial fluctuations can be equally neglected in the limit of infinite coordination number, the same is not true for quantum fluctuations. Hence, not even in this limit a static mean-field approximation is correct, since it neglects both kinds of fluctuations.

To find an analog of a mean-field approximation for quantum physics problems, which becomes exact in the limit of infinite coordination number, one has to retain dynamical quantum fluctuations. This leads to the Dynamical Mean-Field Theory (DMFT) [37], which proved to be a very successful method for the investigation of strongly correlated electron systems.

The general concept of the DMFT approximation is introduced in Sec. 1.3.2. A different perspective on the DMFT is provided by the Self-Energy Functional Approach (SFA) presented in Sec. 1.3.3. Here a derivation of the DMFT equations is given. The SFA can be used equally to motivate various extensions to the DMFT. The site-dependent DMFT, a generalization of the translationally invariant DMFT to inhomogeneous systems, is the topic of Sec. 1.3.4. Finally, in Sec. 1.3.5 cluster extensions to the DMFT are introduced, which were developed in order to systematically incorporate non-local correlations neglected in the single-site DMFT.

1.3.2 DMFT Approximation

The idea of the Dynamical Mean-Field Theory is to map a given lattice problem, e.g. the PAM (1.1.12), onto an effective single-site problem. This can be formulated as an action [37]

$$S_{\text{eff}} = -\int_0^\beta d\tau\, d\tau' \sum_{\alpha,\beta} \hat{\mathrm{f}}^\dagger_\alpha(\tau)\, {G^{(0)}}^{-1}_{\alpha\beta}(\tau-\tau')\, \hat{\mathrm{f}}_\beta(\tau') + \int_0^\beta d\tau\, \hat{\mathcal{H}}_{\text{int}}(\tau) \qquad (1.3.1)$$

with an effective, time-dependent Weiss field $G^{(0)}(\tau)$. It encodes the dynamical quantum fluctuations, namely the process of a particle leaving the impurity at time τ', propagating through the bath and finally returning at time τ. α and β are impurity orbital quantum numbers with energies $\varepsilon_{\text{imp}} = (\varepsilon_\alpha)$. The action given in Eq. (1.3.1) can be recast into a Hamiltonian form

$$\hat{\mathcal{H}}_{\text{aux}} = \sum_k \tilde{\varepsilon}(k)\, \hat{\tilde{c}}_k^\dagger \hat{\tilde{c}}_k + \sum_{k,\alpha} \tilde{V}_\alpha(k) \Big(\hat{\tilde{c}}_k^\dagger \hat{\mathrm{f}}_\alpha + \hat{\mathrm{f}}_\alpha^\dagger \hat{\tilde{c}}_k \Big) + \sum_\alpha \varepsilon_\alpha \hat{\mathrm{f}}_\alpha^\dagger \hat{\mathrm{f}}_\alpha + \hat{\mathcal{H}}_{\text{int}} \tag{1.3.2}$$

in terms of auxiliary bath degrees of freedom $\hat{\tilde{c}}$. $\tilde{\varepsilon}(k)$ is the energy of the bath orbital with quantum number k, which can encode e.g. momentum and spin. The auxiliary Hamiltonian takes the form of the single impurity Anderson model (SIAM). To solve the effective action (1.3.1), or equivalently the auxiliary Hamiltonian (1.3.2), the techniques developed for the solution of impurity models can be employed.

In order to arrive at a closed set of equations, the effective action is supplemented by a self-consistency condition, which determines the effective Weiss field in terms of impurity correlation functions. At the same time it provides the connection to the original lattice problem. It demands that the Green's function of the effective impurity problem is equal to the local lattice Green's function

$$\begin{aligned} G_{\text{imp}}(i\omega) &= G_{\text{loc}}(i\omega) \qquad (1.3.3) \\ \text{where} \quad G_{\text{imp},\alpha\beta}(\tau - \tau') &= \langle \hat{\mathrm{T}}\, \hat{\mathrm{f}}_\alpha^\dagger(\tau)\, \hat{\mathrm{f}}_\beta(\tau') \rangle \\ G_{\text{loc}}(i\omega) &= \frac{1}{N} \sum_k G(k, i\omega) \end{aligned}$$

While Eq. (1.3.1) represents a simplification when compared to the original lattice problem, e.g. the PAM given in Eq. (1.1.12), there still remains a fully quantum-mechanical many-body problem to be solved. In particular, quantum fluctuations, i. e. a particle undergoing transitions in imaginary time between different impurity states, are still included.

By comparison with the expression for the impurity Green's function, one can find a more explicit expression for the Weiss field

$$\begin{aligned} G_{\text{imp}}(i\omega) &= \Big(i\omega - \varepsilon_{\text{imp}} - \Delta(i\omega) - \Sigma_{\text{imp}}(i\omega) \Big)^{-1} \qquad (1.3.4) \\ \Rightarrow G^{(0)}(i\omega) &= \Big(i\omega - \varepsilon_{\text{imp}} - \Delta(i\omega) \Big)^{-1} \qquad (1.3.5) \\ \text{where} \quad \Delta(i\omega) &= \sum_k \tilde{V}_k \Big(i\omega - \tilde{\varepsilon}(k) \Big)^{-1} \tilde{V}_k. \end{aligned}$$

To obtain the actual solution to the dynamical mean-field equations, the bare Green's function $G^{(0)}(i\omega)$, or the hybridization functions $\Delta(i\omega)$, i. e. the auxiliary parameters $\tilde{\varepsilon}(k)$ and $\tilde{V}_\alpha(k)$, have to be determined self-consistently. In practice, this is achieved by iteration, as sketched in Fig. 1.3.1.

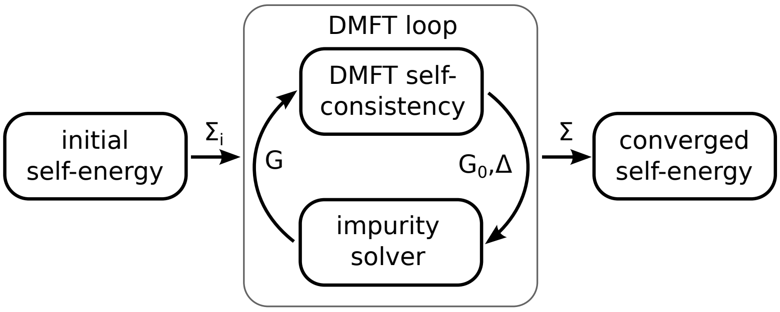

Figure 1.3.1: The DMFT self-consistency is achieved by iteration of impurity solver and self-consistency equation, starting from an initial guess for the self-energy. The converged self-energy is used to calculate lattice correlation functions.

Starting from an initial guess for the self-energy, e.g. $\Sigma = \Sigma_i = 0$, an initial bath function is obtained, which is fed into the impurity solver. The solution to the impurity problem, i. e. the interacting Green's function, subsequently yields a new self-energy via the Dyson equation.

$$\Sigma(i\omega) = G^{(0)^{-1}}(i\omega) - G^{-1}(i\omega) \tag{1.3.6}$$

This loop is iterated until the self-energy is converged. Once a self-consistent solution is found, all correlation functions of the original lattice problem can be obtained from correlation functions of the auxiliary impurity problem. In particular, the lattice self-energy is given by the impurity self-energy

$$\Sigma(k, i\omega) = \Sigma_{\text{imp}}(i\omega). \tag{1.3.7}$$

Thus, it is momentum-independent, and consequently its Fourier transform is purely local

$$\Sigma_{ij}(i\omega) = \delta_{ij}\Sigma(i\omega).$$

The momentum-dependent lattice Green's function is given by

$$G(k, i\omega) = \Big(i\omega - t(k) - \Sigma(i\omega)\Big)^{-1}. \tag{1.3.8}$$

As mentioned above, the Dynamical Mean-Field Theory provides the exact solution to the lattice problem in the limit of infinite coordination number. In this limit the self-energy becomes purely local. Hence, Eq. (1.3.7) is the exact expression for the self-energy. For finite coordination number, i. e. a finite number of spatial dimensions, the use of the DMFT can be regarded as an approximation, which neglects spatial correlations, but fully retains dynamical (quantum) fluctuations.

The Dynamical Mean-Field Theory can be obtained from a truncation of the Luttinger-Ward functional Φ, which can be defined as a series of skeleton diagrams [10, 11]. Taking only local diagrams into account yields the DMFT. Hence, the DMFT approximation is a conserving, i. e. thermodynamically consistent approximation, which respects a number of macroscopic conservation laws [82].

The calculation of the topological invariant by means of the topological Hamiltonian (1.2.9) is significantly simplified within the DMFT. This is a direct consequence of the locality, i. e. momentum-independence, of the self-energy:

$$\begin{aligned} h_{\text{topo}}(k) = -G^{(-1)}(k, i\omega = 0) &= h(k) + \Sigma(i\omega = 0) \\ &= h(k) + \Sigma_0. \end{aligned} \tag{1.3.9}$$

The topological Hamiltonian is simply given by the original, non-interacting Hamiltonian renormalized by the constant energy shift $\Sigma_0 = \Sigma(i\omega = 0)$. As shown in Sec. 2.2.5, this allows for a complete mapping of the phase diagram of the topological Hamiltonian in terms of model parameters, and the renormalization constant Σ_0. Once its value, $\Sigma_0 = \Sigma_0(U)$ is known for a particular value of the interaction strength U, one can immediately obtain the topological properties of the system. In addition, the topological invariant N_s given in Eq. (1.2.8) can be simplified:

$$\begin{aligned} \frac{\partial G_\sigma{}^{-1}(k, i\omega)}{\partial k_i} &= \frac{\partial h_\sigma(k)}{\partial k_i} \\ \Rightarrow N_s &= \operatorname{Im}\Big[\frac{d}{d\omega} K(\omega + iO^+)\Big]_{\omega=0} = \lim_{i\nu \to 0} \frac{\operatorname{Im} K(i\nu)}{\nu} \\ \text{with } K(i\nu) &= -\frac{1}{V\beta} \sum_{k,i\omega,\sigma} \frac{\sigma}{2} \operatorname{tr}\Big[\frac{\partial h_\sigma(k)}{\partial k_y} G_\sigma(k, i\omega + i\nu) \frac{\partial h_\sigma(k)}{\partial k_x} G_\sigma(k, i\omega)\Big]. \end{aligned} \tag{1.3.10}$$

In summary, the DMFT turned out to be a powerful approach to study strongly correlated electron systems. In particular, as dynamical fluctuations are fully retained, it is able to capture the Kondo screening of local moments by delocalized degrees of freedom [48]. The method is very successful in describing the Mott metal-insulator transition. In the correlated metal a quasiparticle peak of weight Z forms, which vanishes at some critical interaction strength [37], where the system turns into an insulator. In addition, the method is widely used in conjunction with band structure method e.g. in LDA+DMFT, where it allows to take correlation effects beyond the mean-field level into account [63].

However, there are areas where the DMFT fails to describe the physics correctly. In general, since the method neglects spatial fluctuations, this applies to phenomena coupled to a momentum-dependence of the self-energy [90], as well as to non-local order parameters for e.g. dimerization or d-wave superconductivity [18]. Concerning long-range order, like antiferromagnetism, DMFT is able to capture the symmetry breaking, but not the non-local fluctuations, which preempt the transition [37]. Since the DMFT is exact in the limit $D \to \infty$, and used as an approximation at finite D, it becomes progressively worse as D becomes lower. In particular, many aspects of one-dimensional systems are beyond the scope of DMFT, like Luttinger liquid formation [90]. Methods developed to improve on some of these shortcomings are discussed in Sec. 1.3.5.

1.3.3 Self-energy Functional Theory Perspective on the DMFT

1.3.3.1 Self-energy Functional Approach

While in the previous section the central ideas and equations of the Dynamical Mean-Field Theory were presented, this section provides a derivation of the DMFT equations. At the same time, a different perspective on the DMFT approximation is given.

To this end, the self-energy functional approach (SFA) s employed. It amounts to formulating a variational principle in terms of the self-energy, such that the physical self-energy is a stationary point of the grand potential. The SFA can be used to derive thermodynamically consistent and systematic approximations to quantum-mechanical many-body problems.

The derivation follows Ref. 81, where the SFA was first proposed, and Ref. 80, which contains additional details and applications of the approach.

The starting point is a Hamiltonian of the form

$$\hat{\mathcal{H}} = \hat{\mathcal{H}}_0(t) + \hat{\mathcal{H}}_1(U), \tag{1.3.11}$$

where $\hat{\mathcal{H}}_0$ is the one-particle hopping part, with the hopping amplitudes parameterized by t, while $\hat{\mathcal{H}}_1$ contains interaction terms, with interaction strength U. The corresponding grand potential $\Omega_{t,U}$ is given as a functional of the Green's function by

$$\Omega_{t,U}[G] = \Phi_U[G] + \operatorname{tr}\ln(-G) - \operatorname{tr}\Big(({G^{(0)}}^{-1} - G^{-1})\,G\Big). \tag{1.3.12}$$

Here, $\Phi_U[G]$ is the Luttinger-Ward functional and tr is the trace over internal indices. The notation makes the dependence on the parameters t and U explicit. The dependence of Ω on the hopping amplitudes t is due to the non-interacting Green's function $G^{(0)}$.

Note that $\Phi_U[G]$ depends explicitly only on U. Hence, it is universal, i. e. the same for models with different values of t. However, a closed expression for Φ cannot be obtained, so that evaluating Eq. (1.3.12) directly is not possible. Instead, an alternate approaches based on writing the Green's function as a functional of the self-energy, i. e. $G = G[\Sigma]$, is pursued. Σ is given by the functional derivative

$$\Sigma = 1/T\,\frac{\delta\Phi_U[G]}{\delta G}. \tag{1.3.13}$$

By a Legendre transform of Φ to the new variable Σ via

$$F_U[\Sigma] = \Phi_U[G[\Sigma]] - \operatorname{tr}(\Sigma\, G[\Sigma]), \tag{1.3.14}$$

the grand potential can be written as a functional of Σ:

$$\Omega_{t,U}[\Sigma] = \operatorname{tr}\ln\Big(-(G^{(0)^{-1}} - \Sigma)^{-1}\Big) + F_U[\Sigma] \tag{1.3.15}$$

$$\text{while } G[\Sigma] = 1/T\,\frac{\delta F_U[\Sigma]}{\delta\Sigma}.$$

From the stationarity condition of the grand potential with respect to the self-energy follows the Dyson equation.

$$\frac{\delta\Omega_{t,U}[\Sigma]}{\delta\Sigma} = 0 \Leftrightarrow G[\Sigma] = (G^{(0)^{-1}} - \Sigma)^{-1}. \tag{1.3.16}$$

This implies that the grand potential is stationary with respect to Σ at the true, physical self-energy.

As a next step, the self-energy is parameterized as $\Sigma = \Sigma(t')$, meaning that the self-energy corresponds to the Hamiltonian with hopping parameters t'. Hence

$$\frac{\partial\Omega_{t,U}[\Sigma(t')]}{\partial t'} = 0 \quad \text{at } t' = t.$$

The functional $F_U[\Sigma]$ prevents the evaluation of $\Omega_{t,U}[\Sigma]$. However, F inherits the universality of Φ. It is the same for a different reference system $\hat{\mathcal{H}}'$

$$\hat{\mathcal{H}}' = \hat{\mathcal{H}}_0(t') + \hat{\mathcal{H}}_1(U). \tag{1.3.17}$$

with the same interaction parameters U, but different hoppings $t' \neq t$.

An explicit comparison of the grand potential $\Omega_{t',U}$ for hopping t' with Eq. (1.3.15) yields

$$\begin{aligned} &\Omega_{t',U}[\Sigma] = \operatorname{tr}\ln\Big(-(G_0'^{-1} - \Sigma)^{-1}\Big) + F_U[\Sigma] \\ &\Rightarrow \Omega_{t,U}[\Sigma] = \Omega_{t',U}[\Sigma] + \operatorname{tr}\ln\Big(-(G^{(0)^{-1}} - \Sigma)^{-1}\Big) - \operatorname{tr}\ln\Big(-G'\Big). \end{aligned} \tag{1.3.18}$$

In the form of Eq. (1.3.18), the grand potential $\Omega_{t,U}$ can be evaluated rigorously for reference system self-energies $\Sigma = \Sigma(t')$.

Demanding stationarity with respect to t' leads to

$$\frac{\partial\Omega_{t,U}[\Sigma(t')]}{\partial t'} = 0 = T\sum_{\omega,i,j}\Big((G^{(0)^{-1}} - \Sigma(t'))^{-1} - G'\Big)_{ij}\,\frac{\partial\Sigma_{ji}(t')}{\partial t'}. \tag{1.3.19}$$

A feasible way to find an approximate solution to the original Hamiltonian therefore proceeds by first defining a suitable reference system with the same interaction parameters as the original model, but different single-particle parameters t'. The simpler structure of the reference system allows to find a solution to the many-body problem, in particular determining the trial self-energy $\Sigma(t')$. By varying the reference system parameters t' to minimize Eq. (1.3.19), an optimal solution is obtained.

1.3.3.2 Motivating the DMFT using the SFA

In the following, the idea of a reference system is illustrated using a concrete example, which serves to elucidate the relation to the DMFT. The original, translationally invariant and homogeneous lattice system is schematically shown in Fig. 1.3.2a, while possible reference systems are shown in Fig. 1.3.2b-c.

Of particular importance for the choice of a suitable reference system is leaving the interaction parameters unchanged from the original lattice problem, to ensure that the functional F is the same for both original and reference system.

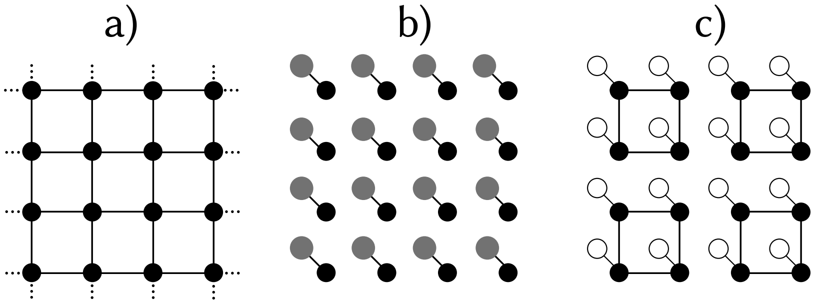

Figure 1.3.2: In the self-energy functional approach, the original, interacting lattice system depicted in a) is approximated by a simpler reference system with variational parameters. In b) a possible choice of a reference system, leading to the DMFT, is shown. The black bold lines represent the hybridization with the bath (solid gray dots). c) is a possible reference system for the VCA, where each site of the plaquette is connected to a single bath site (open dots).

In the case of Fig. 1.3.2b, the reference system is obtained from the original system by switching off the hopping t, and introducing an additional hybridization with a non-interacting bath. The system therefore consists of equivalent, isolated lattice sites coupled to a bath.

In the absence of hopping between correlated sites (Fig. 1.3.2b), the self-energy is local, $\Sigma_{ij} = \delta_{ij}\Sigma$. As a consequence, for the stationary point (1.3.19) it is sufficient to fulfill

$$\left((G^{(0)^{-1}} - \Sigma(t'))^{-1} - G'\right)_{ii} = 0, \tag{1.3.20}$$

which is just the DMFT self-consistency condition (1.3.3). The original lattice system is replaced by a set of identical impurities, where each is coupled to a non-interacting bath. The stationary point of the grand potential is at the same time a solution to the dynamical mean-field equations. The variational parameters are the hybridization amplitudes $\tilde{V}$ and the auxiliary dispersion $\tilde{\varepsilon}$, which are optimized via the hybridization function Δ.

The SFA permits other reference systems, which lead to different approximation schemes. One possible choice is shown in Fig. 1.3.2c. Here, the reference system is obtained by keeping only the hoppings on isolated clusters. In addition, each lattice site is coupled to one additional bath site. In fact, this is a particular realization of the variational cluster approach (VCA) [83]. In this case, the variational parameters are the intracluster hoppings and the bath parameters.

1.3.4 Site-dependent DMFT

The formulation of the DMFT in Eq. (1.3.8) is translation invariant. However, in the case of an inhomogeneous system, or with open boundary conditions, a real-space formulation has to be employed, which enables a spatially inhomogeneous, but still local self-energy [84]:

$$\Sigma_{ij}(i\omega) \approx \delta_{ij}\Sigma_i(i\omega). \tag{1.3.21}$$

Here the index i labels the inequivalent sites within a unit cell of the super lattice, or the layer number in the non-periodic direction. The latter case, with translational invariance broken in one direction, is of interest in Sec. 2.2, and is therefore discussed here.

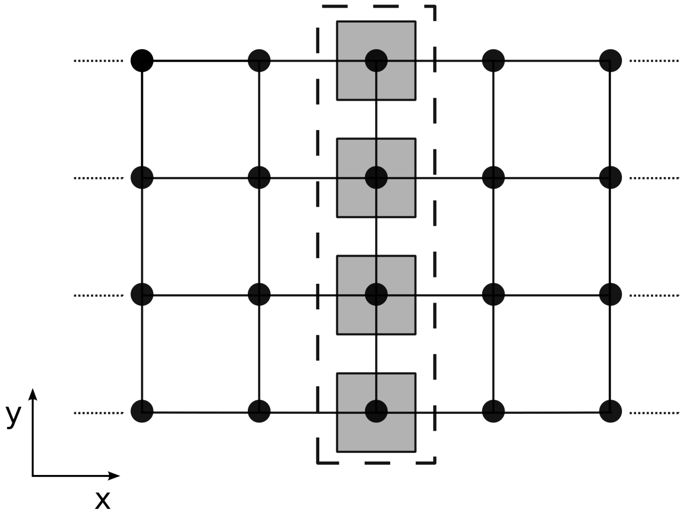

Figure 1.3.3: Lattice with open boundaries in the y-direction. In the x-direction, the lattice is periodic, with the unit cell boundary given by the dashed box. For each of the lattice sites within the unit cell (shaded boxes), the self-energy is assumed to be local, but site-dependent.

In addition to the momentum $k_{\|}$ related to the periodic direction, the Green's function acquires a layer index

$$G_{ij}(k_{\|}, i\omega) = \frac{1}{N_{\|}} \sum_{r} \exp\left(i\, k_{\|}\,(r + r_i - r_j)\right) G_{r+r_i-r_j}(i\omega), \tag{1.3.22}$$

where $N_{\|}$ is the number of sites within one layer. Another perspective on the same problem is given in Fig. 1.3.3. In the direction with open boundaries, all the lattice sites are included in a large unit cell, which is repeated in the periodic direction. In this basis, the Green's function is a matrix of the size of the unit cell, while the periodic direction corresponds to the momentum $k_{\|}$.

In the spirit of the conventional DMFT, non-local correlations, i. e. between different sites within the unit cell and between different unit cells, are neglected. Each of the inequivalent sites is then mapped to a separate impurity problem, with the impurity action given by

$$S_i = \int_0^\beta d\tau\, d\tau' \sum_\sigma \hat{\mathrm{f}}^\dagger_{i,\sigma}(\tau)\, \Delta_i(\tau - \tau')\, \hat{\mathrm{f}}_{i,\sigma}(\tau') + \int_0^\beta d\tau\, \hat{\mathcal{H}}_{\mathrm{imp}}(\tau). \tag{1.3.23}$$

The inequivalence of the sites is mirrored by the inequivalent hybridization functions $\Delta_i(\tau)$. All the impurity problems are coupled only at the single-particle level via the self-consistency condition

$$\begin{aligned} G_i(i\omega) &= \Big(i\omega - t_{\mathrm{imp}} - \Delta_i(i\omega) - \Sigma_i(i\omega)\Big)^{-1} = \Big[G_{\mathrm{loc}}(i\omega)\Big]_{ii} \qquad (1.3.24)\\ \text{where}\quad G_{\mathrm{loc}}(i\omega) &= \frac{1}{N_{\|}} \sum_{k_{\|}} \Big(\omega - H_0(k_{\|}) - \Sigma(i\omega)\Big)^{-1}. \end{aligned}$$

From the viewpoint of the SFA, the site-dependent DMFT is obtained by removing the hoppings between neighboring sites, instead coupling each site to a non-interacting bath. However, in contrast to the homogeneous DMFT, the baths are not equivalent, i. e. the stationary point corresponds to different values for the variational parameters for each site. Hence, the self-energy is local, but site-dependent.

1.3.5 Non-local Extensions to the DMFT

To improve on the shortcomings of the DMFT, the so-called cluster extensions were devised [69]. The goal of these approaches is to go beyond the local self-energy approximation and include non-local correlation effects in a systematic way. The general idea is to consider local degrees of freedom on a cluster of size N_c exactly, while replacing the remaining degrees of freedom by a bath of non-interacting sites. Within this scheme, the DMFT is recovered by a cluster of size $N_c = 1$, while larger clusters systematically incorporate non-local correlations. In the limit of very large cluster size, the solution converges to the exact result.

While there is a unique way to define the single-site DMFT, there are different possibilities to formulate a cluster extension. One of the central requirements is that the self-consistency condition does not produce solutions violating causality [18]. This is fulfilled in the case of the two most widely used flavors of cluster DMFT, namely the Cellular DMFT and the Dynamical Cluster approximation. In the following, both are introduced briefly.

The Cellular DMFT [64] represents a straightforward generalisation of the single-site DMFT to a real-space cluster of N_c site. The self-consistency condition is now a matrix equation, which is formulated in the reduced Brillouin zone of the super-lattice.

$$G_C(i\omega) = \frac{N_c}{N} \sum_{K \in red.BZ} G(K, \omega) \tag{1.3.25}$$

$$\text{where} \quad G(K, i\omega) = \Big(i\omega - t(K) - \Sigma(i\omega)\Big)^{-1}$$

$$\text{and} \quad t_{i,j}(K) = \sum_{k_c} e^{i(K+k_c)(R_i - R_j)}\, t(K + k_c) \tag{1.3.26}$$

R_i are the positions of the sites within the cluster, K is a momentum in the reduced Brillouin zone and k_c is a cluster momentum.

The scheme manifestly breaks translational invariance. As the symmetry is present in the original lattice problem, it has to be recovered by periodizing the self-energy. To this end, different schemes were proposed [18]. Maybe the most straightforward possibility is

$$\Sigma_{\text{latt}}(k, i\omega) = \frac{1}{N_c} \sum_{i,j} \exp\left(i\, k\, (R_i - R_j)\right) \Sigma_{C,i,j}(i\omega) \tag{1.3.27}$$

On the other hand, the breaking of translational symmetry allows to capture symmetry-broken phases with further modifications.

From the perspective of the SFA, the Cellular DMFT is obtained from a reference system, where the system is split into isolated clusters. In order to compensate for the missing intercluster hoppings, to each cluster site a bath is attached. Just like in the DMFT, the stationarity condition is fulfilled by the self-consistent solution to the dynamical mean-field equation (1.3.25).

In contrast to the Cellular DMFT, the Dynamical Cluster Approximation (DCA) is formulated in reciprocal space [47]. While the DMFT self-energy is constant in the whole Brillouin zone, here the extension to a cluster of size N_c means that the self-energy is approximated as a constant on N_c patches of the Brillouin zone, which are located around the coarse-grained momenta $\tilde{K}$ [46]

$$\Sigma(\tilde{K} + k, \omega) \approx \Sigma(\tilde{K}, \omega) \tag{1.3.28}$$

$$G_C(\tilde{K}, \omega) = \bar{G}_{\text{latt}}(\tilde{K}, \omega) = \frac{N_c}{N} \sum_{k \sim \tilde{K}} G_{\text{latt}}(k, \omega).$$

The DMFT is contained in this scheme in the limit, where the whole Brillouin zone is covered by a single patch. Due to the formulation as a periodic cluster, i. e. in reciprocal space, translational invariance is not broken by the DCA. However, to capture phases with broken symmetry, the symmetry-breaking has to be allowed for by a modified formulation of the algorithm. In the SFA framework, there is no reference system which can by used to generate the DCA.

Besides these two methods, other approaches were proposed to go beyond the single-site DMFT. Examples are Extended Dynamical Mean-Field Theory [63, 100], Dual Fermions [90] and the Dynamical Vertex Approximation [106].

Finally it should be noted, that the (cluster) DMFT can be regarded as a complementary approach to direct simulations of the models on finite size lattices [69], which can be conducted by e.g. exact diagonalization of the Hamiltonian matrix or lattice Quantum Monte Carlo methods [7, 91].

1.4 Continuous Time Quantum Monte Carlo

1.4.1 General concept

Continuous Time Quantum Monte Carlo (CTQMC) methods are numerical simulation methods for quantum mechanical models. In particular, CTQMC methods are commonly employed as solvers for the auxiliary impurity problems arising in the DMFT and generalization thereof.

Here some general remarks about the basics of Monte Carlo methods in general and the underlying concept of CTQMC are made. Section 1.4.2 is devoted to the detailed description of a particular CTQMC algorithm, hybridization expansion CTQMC (CT-HYB) method. A detailed discussion of the different flavors of CTQMC and their applications can be found in Ref. 39. Section 1.4.3 introduces the stochastic analytical continuation, which is a method applied to QMC results in order to obtain physical observables, in particular correlation functions, on the real-frequency axis.

The general idea of Monte Carlo methods is the stochastic sampling of quantities of interest from a known or unknown distribution. The CTQMC methods are a particular realization of this general concept. They are based on a quantum mechanical action

$$S = \int_0^\beta d\tau \left(\bar{\Psi}(\tau) \frac{d}{d\tau} \Psi(\tau) + \hat{\mathcal{H}}[\bar{\Psi}(\tau), \Psi(\tau)] \right) \tag{1.4.1}$$

Here $\bar{\Psi}$ is the complex conjugate (conjugate) of the complex-valued boson field (Grassmann-valued fermion field) Ψ.

In the following, the algorithm is formulated quite generally. To facilitate the later presentation of results, the methods are introduced using a fermionic quantum impurity model. Nevertheless, they can be formulated equally for a lattice model.

The derivation starts with the general Hamiltonian (1.1.14). Noting that there is no interaction on the c-fermions, i. e. the Hamiltonian is quadratic in $\hat{c}^\dagger$ and $\hat{c}$, the corresponding degrees of freedom can be integrated out. As a consequence, the hybridization term gives rise to a hybridization function Δ, which contains all the relevant information about the bath degrees of freedom.

$$\Delta(i\omega) = \sum_{i,j} V_i \left(i\omega - t^{(c)} \right)^{-1}_{ij} V_j \tag{1.4.2}$$

In total, the effective retarded action reads

$$\begin{aligned}
S_{\text{eff}} = & \int_0^\beta d\tau\, \hat{\mathrm{f}}^\dagger(\tau) \left(\frac{d}{d\tau} + t^{(f)} \right) \hat{\mathrm{f}}(\tau) && (1.4.3)\\
& + \int_0^\beta d\tau\, d\tau'\, \hat{\mathrm{f}}^\dagger(\tau)\, \Delta(\tau-\tau')\, \hat{\mathrm{f}}(\tau') \\
& + \int_0^\beta d\tau \sum_{\alpha,\beta,\gamma,\delta} U_{\alpha\beta\gamma\delta}\, \hat{\mathrm{f}}^\dagger_\alpha \hat{\mathrm{f}}^\dagger_\beta \hat{\mathrm{f}}_\delta \hat{\mathrm{f}}_\gamma \\
= & \int_0^\beta d\tau\, d\tau' \hat{\mathrm{f}}^\dagger(\tau)\, G^{(0)^{-1}}(\tau-\tau')\, \hat{\mathrm{f}}(\tau') + \int_0^\beta d\tau\, \hat{\mathcal{H}}_{\text{int}}(\tau). && (1.4.4)
\end{aligned}$$

The first expression is the basis for the hybridization expansion CTQMC (CT-HYB) presented in the next section. The second expression can be obtained by noting that the non-interacting impurity Green's function is given by

$$G^{(0)^{-1}}(\tau-\tau') = \Big(\frac{d}{d\tau} + t^{(f)} \Big) \delta(\tau-\tau') + \Delta(\tau-\tau')$$

It is the starting point for the interaction expansion CTQMC (CT-INT) [91] and the related auxiliary field CTQMC (CT-AUX) [39], which sample terms from a systematic expansion of the partition function in powers of the interaction vertex.

1.4.2 Hybridization expansion CTQMC

1.4.2.1 Introduction

While the interaction expansion can be used to solve a variety of models, there are still a large number of situations which are almost intractable with this method. On the one hand, the calculations may become computationally very expensive. This is the case for f-electron systems with almost localized orbitals, where the interaction strength is very large, so that the expansion order becomes very large as well.

On the other hand, the expansion can become very complicated, like in realistic simulations for multi-orbital systems, where the complexity of the Hund's rule exchange makes a separate expansion for each of the multiple interaction parameters necessary.

Under these circumstances, a complementary approach is advantageous: the hybridization expansion CTQMC algorithm (CT-HYB). This method was first proposed by P. Werner et al.

in Refs. 118 and 120, and later generalized by C. Haule in Ref. 44 to clusters, making the method applicable for C-DMFT and DCA calculations.

In contrast to the interaction expansion methods, here the starting point is the atomic limit, i. e. the isolated impurity. All interactions which act locally are fully included. There is no expansion in the interaction necessary, so that one can incorporate all relevant exchange processes, irrespective ot the interaction strength. This makes it very well suited for model calculations with large interaction parameters, as well as for multi-orbital models with a large number of interaction matrix elements.

A performance analysis conducted in Ref. 40 revealed the advantages of this algorithm compared to the CT-INT and Hirsch-Fye QMC methods. In particular, in the case of the SIAM, which is relevant for DMFT calculations of the single-band Hubbard model, the scaling with the Hubbard interaction U is very favorable. In fact, the average expansion order decreases for large values of U. This is in marked contrast to the polynomial scaling of the interaction expansion methods.

The drawback of the CT-HYB method is its scaling with the number of correlated orbitals or cluster sites N_c. As the method is based on an perturbation expansion around the atomic limit, the isolated impurity or cluster has to be solved exactly, i. e. by means of an exact diagonalization. Thus, the CT-HYB inherits the scaling from the exact diagonalization of its atomic limit, which is exponential in N_c. This represents a huge barrier for large-scale multi-orbital and cluster simulations, which ultimately limits the method's application to DMFT calculations and extensions thereof. The scaling with inverse temperature $\beta = 1/T$ is cubic, i. e. equivalent to the interaction expansion methods.

1.4.2.2 General Formulation

To begin, the Hamiltonian given in Eq. (1.1.14) is considered, namely

$$\hat{\mathcal{H}} = \underbrace{\hat{\mathcal{H}}_c}_{\text{bath}} + \underbrace{\hat{\mathcal{H}}_{cf}}_{\text{hybridization}} + \underbrace{\hat{\mathcal{H}}_f + \hat{\mathcal{H}}_I}_{\text{correlated part}} . \tag{1.4.5}$$

In the case of an impurity calculation, the correlated part of the system contains only few degrees of freedom f_α. The corresponding grand-canonical partition function Z is given by

$$Z = \int D[\bar{\mathrm{c}}, \mathrm{c}, \hat{\mathrm{f}}, \mathrm{f}] e^{-S[\bar{\mathrm{c}},\mathrm{c},\bar{\mathrm{f}},\mathrm{f}]} \tag{1.4.6}$$

As argued in the previous section, the uncorrelated bath degrees of freedom c can be integrated out, which yields an effective impurity action for the remaining, correlated degrees of freedom given in Eq. (1.4.3), such that the partition function becomes

$$Z = \int D[\bar{\mathrm{f}}, \mathrm{f}] e^{-S_{\mathrm{eff}}[\bar{\mathrm{f}},\mathrm{f}]} \tag{1.4.7}$$

The effect of the bath degrees of freedom is encoded in the time-dependent hybridization function $\Delta(\tau)$ (c.f. Eq. (1.4.3)), which is the dynamical Weiss field in the case of DMFT.

The task is to calculate impurity correlation function like the single-particle Green's function, and other observables like the double occupancy, in the presence of the bath.

The idea from Refs. 118 and 120 is to do a perturbation expansion of the partition function in powers of the hybridization. The final expression of the partition function reads

$$\begin{aligned} Z =& Z_i \sum_{n=0}^{+\infty} \sum_{\alpha,\beta} \frac{1}{n!} \int_0^\beta d\tau_1\, d\tau_1' \cdots d\tau_k\, d\tau_k' \times \\ & \times \underbrace{\langle \hat{\mathrm{T}}\, \hat{\mathrm{f}}^\dagger_{\alpha_1}(\tau_1)\, \hat{\mathrm{f}}_{\beta_1}(\tau_1') \cdots \hat{\mathrm{f}}^\dagger_{\alpha_n}(\tau_n)\, \hat{\mathrm{f}}_{\beta_n}(\tau_n') \rangle_i}_{A} \times \\ & \times \frac{1}{n!} \underbrace{\det(\Delta_{ij})}_{D} \\ \text{where} \quad \Delta_{ij} =& \Delta_{\alpha_i \beta_j}(\tau_i - \tau_j') \end{aligned} \tag{1.4.8}$$

$\hat{\mathrm{T}}$ is the time-ordering operator. The result tells, that for each order n, there is a sum over all possible configurations of f-operators in orbital space and imaginary time. For each configuration, the contribution to the partition function is given by the expectation value of the time-ordered string of operators taken with respect to the impurity degrees of freedom $A = \langle T \cdots \rangle_i$, multiplied by the determinant of the matrix constructed from all possible hybridization events $D = \det(\Delta_{ij})$. Equation (1.4.8) is the central result for the CT-HYB algorithm.

Thus, starting from the isolated impurity at zeroth order, the algorithm does a perturbation expansion to all orders in the hybridization. As an example, Fig. 1.4.1 schematically shows a second-order contribution to this expansion. Thus, one systematically samples all possible ways that particles can hop from the bath to the impurity and vice versa. Every hybridization line connects a pair of operators, which annihilate and create particles on the impurity orbital, and encodes the time-evolution of the particle's state while it resides in the bath. The determinant represents all possible ways of connecting operators by hybridization lines.

One can write the partition function as a sum over configuration C, where each realization contributes according to its weight

$$Z = \sum_C P[C] A[C] D[C]. \tag{1.4.9}$$

Here, $P[C]$ is a prefactor which depends only on the expansion order n, while $A[C]$ and $D[C]$ are the value of the local trace and the determinant for the configuration C. In the form of Eq. (1.4.9), it becomes evident, that the partition function can be evaluated by a Monte Carlo integration. To be specific, in a random walk along a Markov chain in configuration

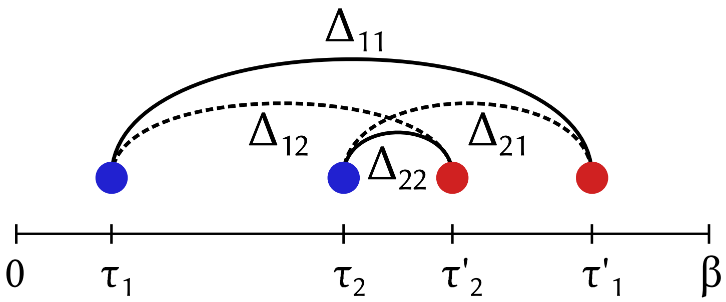

Figure 1.4.1: Second-order contribution to the hybridization expansion. The blue (red) dots represent creation (annihilation) operators at time τ_i (τ_i'). In addition to the diagonal hybridization terms (solid), the determinant takes into account all other possible hybridization events (dashed).

space, a sequence of configurations C of operators is generated. For each configuration, the values of $A[C]$ and $D[C]$ have to be computed. A new configuration is generated starting from the previous one by proposing an update to the string of operators. This is the subject of Sec. 1.4.2.5.

In a very general implementation of the CT-HYB algorithm, a so-called ”matrix code”, the operators are represented by matrices in some basis of the local Hilbert space. A convenient choice is the eigenbasis of the local Hamiltonian. In this basis, the operator matrices become dense, while the time evolution becomes straightforward.

This kind of implementation can treat any type of local interaction. The problem is that the size of local Hilbert space, and thus of the operator matrices, grows exponentially with the number of local degrees of freedom. This makes the simulation of larger systems unfeasible. In Sec. 1.4.2.6 some strategies are presented to get to as large as possible systems. Nevertheless, the exponential scaling ultimately limits the applicability of a general matrix implementation of the CT-HYB method to small systems.

One important case, where additional simplifications are possible is given for a model with only density-density type of interaction and no inter-orbital hopping [39]:

$$\begin{aligned} \hat{\mathcal{H}}_i^{(0)} &= \sum_{\alpha} \varepsilon_\alpha \hat{\mathrm{n}}_\alpha \\ \hat{\mathcal{H}}_i^{(I)} &= \sum_{\alpha\beta} U_{\alpha\beta} \hat{\mathrm{n}}_\alpha \hat{\mathrm{n}}_\beta \\ \text{where} \quad \hat{\mathrm{n}}_\alpha &= \hat{\mathrm{f}}_\alpha^\dagger \hat{\mathrm{f}}_\alpha . \end{aligned} \tag{1.4.10}$$

The simplification results from the fact, that the impurity Hamiltonian commutes with the occupation number of each individual orbital

$$\left[\hat{\mathcal{H}}_i, \hat{\mathrm{n}}_\alpha\right] = 0.$$

Therefore, the time evolution does not mix different orbitals, which makes a representation of the configuration of operators C using so-called "segments" possible. These are intervals on the imaginary time axis, where an orbital is occupied by a fermion. Then it suffices to calculate for the current configuration the length of segments $L_\alpha[C]$ for all orbitals, as well as the overlap between segments of different orbitals $O_{\alpha\beta}[C]$. The calculation of $A[C]$ then proceeds as follows:

$$A[C] = s \exp\Big(-\sum_\alpha \varepsilon_\alpha L_\alpha[C] - \sum_{\alpha\beta} U_{\alpha\beta} O_{\alpha\beta}[C]\Big) \tag{1.4.11}$$

with a sign factor $s = \pm 1$ which results from the time-ordering. The advantage of this formulation becomes immediately visible: This algorithm has only polynomial complexity in the number of local degrees of freedom, in contrast to the exponential scaling of the "matrix code".

As a short remark, another proposal for an efficient evaluation of the trace of operator products was brought forward in Ref. 65. The difference compared to the above algorithm is, that here particle-number basis is chosen, such that the application of creation and annihilation operators is trivial. Meanwhile, the time-evolution is accomplished by a Krylov-subspace method. The authors still observe an exponential increase of computational complexity, but with a reduced slope compared to the "matrix code", which makes this method favorable for more than 3 orbitals.

Besides these optimized methods of evaluating the trace, the CT-HYB method was extended in Ref. 121 to include electron-phonon coupling. Basically, the coupling of the electrons to a bath of non-interacting bosons leads to an effective, frequency dependent interaction $U(\omega)$. This kind of interaction can be incorporated into the algorithm at no computational cost. In general, a screened, frequency-dependent interaction can arise in other context, like in the down-folding of a multi-band model onto an effective single-band model. Here the method is equally applicable [123].

1.4.2.3 Measurement of Observables

The measurement of observables is the actual goal of performing numerical simulations. In general, the Monte Carlo average of the expectation value of an operator $\hat{\mathrm{O}}$, e.g. the occupation of an orbital $\hat{\mathrm{n}}_\alpha$ or an equal-time correlation function, yields an observable value O

$$O = \langle\!\langle \hat{\mathrm{O}} \rangle\!\rangle = \sum_C \frac{\langle \hat{\mathrm{T}}\, \hat{\mathrm{f}}^\dagger_{\alpha_1}(\tau_1)\, \hat{\mathrm{f}}_{\beta_1}(\tau'_1) \cdots \hat{\mathrm{f}}^\dagger_{\alpha_n}(\tau_n)\, \hat{\mathrm{f}}_{\beta_n}(\tau'_n)\, \hat{\mathrm{O}} \rangle_i}{A[C]} \tag{1.4.12}$$

which is exact up to statistical uncertainty. A particular observable, which can provide interesting insights into the state of the system is the reduced impurity density matrix $\rho = \langle\langle \hat{\rho} \rangle\rangle$. By investigating the occupation of individual states $|i\rangle$, given by ρ_{ii}, one can infer the character of the states contributing to the properties of the system.

To measure time-displaced correlation functions, one uses a different approach. This is exemplified by the single-particle Green's function in imaginary time

$$G_{\alpha\beta}(\tau - \tau') = \langle \hat{\mathrm{T}}\, \hat{\mathrm{f}}^{\dagger}_{\alpha}(\tau)\, \hat{\mathrm{f}}_{\beta}(\tau') \rangle. \tag{1.4.13}$$

which is a very important quantity, in particular for DMFT applications, In the standard procedure of measuring the Green's function in the CT-HYB algorithm, the measurement values are direcly read of from the inverse of the hybridization function matrix [39], i. e.

$$G_{\alpha\beta}(\tau - \tau') = \langle\langle \sum_{i,j=1}^{n} \delta_{\alpha,\alpha_i}\, \delta_{\beta,\beta_j}\, \tilde{\delta}(\tau - \tau', \tau_i - \tau_j')\, (\Delta^{-1})_{ij} \rangle\rangle \tag{1.4.14}$$

$$\text{where} \quad \tilde{\delta}(\tau, \tau') = \begin{cases} \delta(\tau - \tau'), & \tau' > 0 \\ -\delta(\tau - \tau' - \beta), & \tau' < 0 \end{cases}$$

For a configuration of order n this yields n^2 correlated measurement values, which can be gathered in fine imaginary time bins, and used to calculate the imaginary frequency Green's function after the simulation. Directly measuring the Green's function in Matsubara frequencies is possible as well, by a simple Fourier transform of the above expression. Both methods yield very accurate results at low frequencies, while the statistical noise becomes quite substantial at higher frequencies. As discussed in Sec. 1.4.2.6, this can lead to problems when computing the self-energy.

Besides the single-particle Green's function, higher-order correlation functions like the two-particle Green's function G_2 can be measured in a very similar way. However, the standard approach described here has some shortcomings, which are discussed in Sec. 1.4.2.6 in the context of improved estimators.

1.4.2.4 Applications

Here a short overview of selected applications of CT-HYB is given, mainly DMFT and cluster DMFT studies, where the method is used to efficiently solve the auxiliary impurity problem.

The CT-HYB solver was employed in DMFT investigations of multiorbital Mott systems, where it allows to include the complicated Hund's rule exchange and to access low temperatures. These studies are relevant for transition metal oxides with partially filled d-orbitals.

In a two-orbital model, the Hund's exchange J greatly influences the critical Hubbard U for the Mott transition [122]. The introduction of a crystal field splitting Δ_{CEF}, which lifts the degeneracy of the orbitals, additionally shifts the critical U. For larger values of Δ_{CEF} an orbitally polarized insulator may be realized in the non-interacting case, while the interactions can stabilize a metallic state. By doping the system away from half-filling, an orbital-selective Mott state is found.

In a three-orbital model studied in Ref. 119, in addition to the Mott phases at integer fillings, a non-Fermi-liquid frozen moment phase was found, with a square-root dependence of the self-energy on frequency.

The inclusion of an orbital splitting Δ_{CEF} in a three-orbital model in Ref. 60 leads to a slight suppression of the metallic phase for small Δ_{CEF}. For larger splitting, a correlated insulating state adiabatically connected to a band insulator is found. For large values of the Hund's exchange J an orbital-selective Mott insulator is found even at commensurate filling.

In Ref. 77 a comparison was conducted between models with only d-orbitals and with d- and additional oxygen p-orbitals, respectively. The inclusion of the p-orbitals strongly influences the filling of the d-orbitals, which changes from $n_d = 1$ to close to 2. Thereby, the influence of the Hund's exchange on the effective crystal field splitting is reversed. In summary, this leads to a marked difference in the low-energy behavior.

In Ref. 76 the Kondo lattice model, a prototypical model for the interplay of delocalized electrons with localized moments (c.f. Eq. (1.1.13)), was investigated using the DMFT approximation. The CT-HYB algorithm was employed for the self-consistent solution of the auxiliary impurity problem. As a function of temperature, the crossover from the local-moment regime with a small Fermi surface to the Fermi-liquid regime with a large Fermi surface was observed. The associated crossover scale T^* was obtained from the renormalization of the chemical potential due to the self-energy.

The pnictides based on iron and arsenic, represent a new class of superconductors, where correlations might play an important role. In Ref. 45, a microscopic model for these materials was derived and investigated using LDA+DMFT. The resulting five-orbital model was simulated numerically using the CT-HYB method. In the normal state, the authors found a crossover from an incoherent, anomalous phase to a coherent Fermi liquid. The crossover scale depends strongly on the value of the Hund's exchange J. Taking the full, rotationally invariant Hund's exchange into account turns out the be crucial for the stability of the Fermi liquid at zero temperature.

Within the emerging field of topological insulators, there is a recent interest in correlated topological insulators [49] (c.f. Sec. 1.2.4). In this context, a series of studies investigated the correlated BHZ model for HgTe quantum wells, using DMFT. The CT-HYB method was employed as impurity solver, which allowed to reach large interaction parameters and low temperatures.

In particular, a first-order transition from the topological band insulator to a Mott state was found, which is hidden inside an antiferromagnetic phase once a symmetry-breaking is allowed for [129]. Even a coexistence region of antiferromagnetic and topological state was observed [130]. However, this coexistence might be an artifact of the approximation.

The inclusion of the full Hund's rule coupling of the two orbitals involved results in a shift of the critical interaction strength to smaller values [21]. In addition, this particular investigation found, that the system can be driven from the topologically trivial state without interactions to a non-trivial state by gradually switching on the interactions.

One particular class of materials attracting increased interest are Kondo insulators, which were conjectured to host a topological state. Recently, a study of the optical conductivity of topological Kondo insulators revealed that the Drude weight associated with the edge states scales precisely with the bulk coherence scale T_{coh} [23]. Meanwhile, the density of states at the edge remains constant as T_{coh} decreases with increasing interaction strength, which is due to the renormalization of edge velocity. Away from half-filling, another investigation found that a topological state is hidden inside a ferromagnetic, metallic state [131].

A detailed discussion of model calculations for topological Kondo insulators conducted by means of DMFT+CT-HYB is presented in Sec. 2.2.

1.4.2.5 Update Rules

The Monte-Carlo algorithm proceeds by creating a sequence of configurations. A new configuration of operators is created from the previous one by means of an update. Thus, the whole sequence represents a Markov chain.

There are several possibilities for defining a valid update procedure. The main criterion for the choice of update moves is that the ergodicity has to be fulfilled. This means that it must be possible to get from one particular configuration to any other one by a finite number of allowed updates.

In addition, the configurations have to be sampled from the equilibrium distribution P, such that each configuration C is visited by the Monte Carlo process with the probability

$$p = P[C] = \frac{W[C]}{Z}. \tag{1.4.15}$$

Thus, every configuration has to be realized with a probability proportional to its contribution to the partition function. This is accomplished by enforcing the detailed balance condition on the transition probability $\xi(C \to C')$ between configurations C and C'

$$\begin{aligned} P[C']\,\xi(C \to C') &= P[C]\,\xi(C' \to C) \\ \Leftrightarrow \frac{\xi(C \to C')}{\xi(C' \to C)} &= \frac{P[C]}{P[C']} \end{aligned} \tag{1.4.16}$$

A Metropolis sampling is employed, which splits the transition probability into two parts: First, a proposal probability $T(C', C)$ and second, an acceptance probability $S(C', C)$

$$\xi(C \to C') = T(C', C)\, S(C', C). \tag{1.4.17}$$

This allows to choose a simple form for $T(C', C)$ and solve for $S(C', C)$ by enforcing the detailed balance condition:

$$\frac{S(C', C)}{S(C, C')} = \frac{P[C']\, T(C, C')}{P[C]\, T(C', C)}, \tag{1.4.18}$$

which yields

$$\begin{aligned} S(C', C) &= F\left(\frac{P[C']\, T(C, C')}{P[C]\, T(C', C)}\right) \\ &\overset{(1.4.15)}{=} F\left(\frac{W[C']\, T(C, C'}{W[C]\, T(C', C)}\right) \end{aligned} \tag{1.4.19}$$

$$\text{where} \quad \frac{F(x)}{F(1/x)} = x. \tag{1.4.20}$$

For the Metropolis sampling, the function F is chosen as

$$F(x) = \min(1, x). \tag{1.4.21}$$

In order to keep the notation simple, in the following description of possible update moves, the arguments of transition and acceptance probabilities are written in such a way, that they reflect only the most important aspect of the configurations that changes during the update.

The first possible update of the current configuration C of expansion order n is to add a pair of creation and annihilation operators at randomly chosen imaginary time positions. The result is a new configuration C' with expansion order $n + 1$. The opposite is achieved by removing a random pair of operators. The proposal probability for adding operators is obtained in the following way:

1. Pick randomly one of the N possible orbitals (including spin) α for the creation operator, and another one β for the annihilation operator.
2. Choose two random times on the time axis, τ and τ', between 0 and β.
3. Place the operator pair randomly at one of the $n + 1$ possible positions in the string of operators.

Gathering the different contributions to the proposal probability yields the result

$$T(n \to n+1) = \frac{1}{N^2 \beta^2 (n+1)^2}. \tag{1.4.22}$$

For the remove update, from picking randomly one of the n creation operators and one of the annihilation operators, one obtains the result

$$T(n \to n-1) = \frac{1}{n^2}. \tag{1.4.23}$$

Finally, the acceptance probabilities are given by

$$\begin{aligned}
S(n \to n+1) &= \min\left(1, \frac{W(n+1)}{W(n)} \frac{T(n+1 \to n)}{T(n \to n+1)}\right) \\
&= \min\left(1, \frac{n!n!}{A(n)\,D(n)} \frac{A(n+1)\,D(n+1)}{(n+1)!(n+1)!} \frac{N^2\beta^2\,(n+1)^2}{(n+1)^2}\right) \\
&= \min\left(1, \frac{N^2\beta^2}{(n+1)^2} \frac{A(n+1)\,D(n+1)}{A(n)\,D(n)}\right). \qquad (1.4.24) \\
\text{and} \quad S(n \to n-1) &= \min\left(1, \frac{n^2}{N^2\beta^2} \frac{A(n-1)\,D(n-1)}{A(n)\,D(n)}\right). \qquad (1.4.25)
\end{aligned}$$

Another possible update of the configuration of operators is to shift one operator chosen randomly on the time axis from its current position, denoted by τ_{old}, to a new position τ_{new}. This move is self-balancing, i. e. the update is reversed by an additional shift, but of opposite direction. Therefore, the acceptance probability is simply given by

$$S(\tau_{\text{old}} \to \tau_{\text{new}}) = \min\left(1, \frac{A(\tau_{\text{new}})D(\tau_{\text{new}})}{A(\tau_{\text{old}})D(\tau_{\text{old}})}\right). \qquad (1.4.26)$$

In the case of a symmetry-broken phase, the pair of add and remove updates is not sufficient to ensure ergodicity. Instead, higher-order updates involving more than two operators have to be employed [95]. As an example, consider the flipping of the spin of a pair of operators. This emulates the removal of a pair of operators and the subsequent addition of a pair of operators with opposite spin at the same positions in time. The acceptance probability for this kind of move is given by

$$S(\sigma \to -\sigma) = \min\left(1, \frac{n_\sigma}{n_{-\sigma}+1} \frac{A(-\sigma)D(-\sigma-)}{A(\sigma)D(\sigma)}\right). \qquad (1.4.27)$$

Here, n_σ is the number of operator pairs with spin orientation σ.

1.4.2.6 Tricks and Optimizations

The bottleneck of the CT-HYB algorithm is usually the evaluation of the trace of local operators. At expansion order n, this corresponds to a product of $2n$ matrices. Each matrix is the size of the local Hilbert space D_H, which scales unfavorably with the number of local degrees of freedom N

$$D_H = \text{dim(local Hamiltonian)}^N.$$

One way of reducing the computational complexity of the matrix multiplications was introduced in Ref. 44. By exploiting symmetries of the Hamiltonian, it is possible to split the Hamiltonian and operator matrices into blocks. The most obvious simplification result by exploiting conservation of the total particle number $\hat{\text{N}}$. Creation and annihilation operators connect blocks with different particle number in a well-defined way, e.g. the creation operators $\hat{c}^\dagger$ connect the block with N particles to the block with $N+1$ particles. An additional conserved quantity is the z-component of the total spin $\hat{S}_z$. As an example, $\hat{c}^\dagger_\uparrow$ connects the blocks (N, S_z) and $(N+1, S_z+1/2)$.

A more thorough analysis for interactions obeying $SU(2)$-symmetry done in Ref. 78 reveals another set of conserved quantities, which can be used in models without a direct hopping between correlated sites or orbitals. In this case, the projector onto states with just a single fermion

$$\hat{PS}_a = (\hat{n}_{a,\uparrow} - \hat{n}_{a,\downarrow})^2, \quad a = 1\ldots M \tag{1.4.28}$$

commutes with the local Hamiltonian. The sequence of $PS = (PS_1, \ldots, PS_M)$ is a good quantum number, and can be exploited in the same way as N and S_z to reduce the size of the matrix blocks. The possible reduction of the matrix block size by exploiting different sets of symmetries is shown in Table 1.1.

number of orbitals or sites M	considered symmetries			
	$\emptyset$	N	N, S_z	N, S_z, PS
$M = 2$	$16 = 4^2$	6	4	2
$M = 3$	$64 = 4^3$	20	9	3
$M = 4$	$256 = 4^4$	70	36	6
$M = 5$	$1024 = 4^4$	252	100	10
asymptotic scaling ($M \to \infty$)	4^M	$\frac{4^M}{\sqrt{M}}$	$\frac{4^M}{M}$	$\frac{2^M}{\sqrt{M}}$

Table 1.1: Size of the largest matrix block for different number of sites or orbitals, when exploiting different sets of symmetries.

In some models it is reasonable to assume that the sites are occupied by at most one fermion at a time. This can be the case in Ce-based compounds, which has a $4f^1$ configuration, or in models for He-3 layer systems as discussed in Sec. 2.1, where the fermions are in fact atoms with a hard-core repulsion. Such a situation can be realized in a model Hamiltonian by taking the limit of an infinitely large Hubbard repulsion U. Thus, the energy penalty for putting two particles on the same sites becomes so large, that the states with double occupancy are never populated. As a consequence, one can project out these states, arriving at a formulation of the Hamiltonian in a restricted Hilbert space. In the case of the Hubbard model or PAM this decreases the size of the local Hamiltonian from 4 states to only 3 states, which can amount to a quite substantial reduction in the case of clusters with multiple sites.

Another possibility of reducing the time spent calculating the local trace can be realized by recycling results from previous updates. The easiest way is to split the chain of matrix products

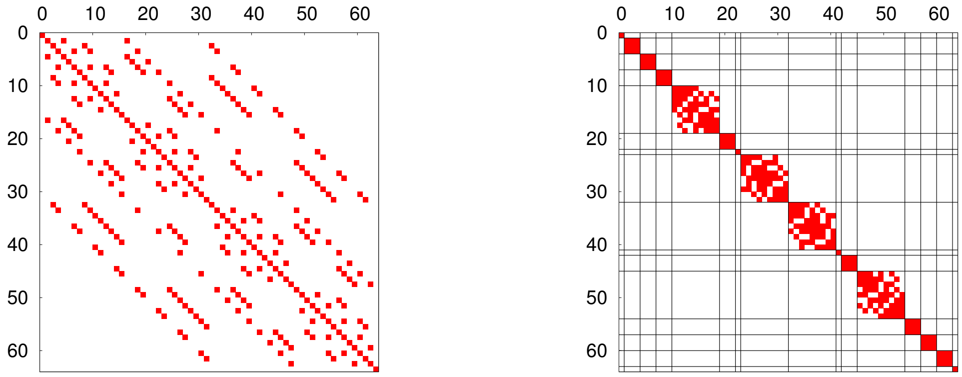

(a) Symmetries not taken into account. Obviously there is some structure, which can be exploited to reduce the computational complexity.

(b) States grouped by particle number N and z-component of the total spin S_z. The largest blocks are of size 9×9.

Figure 1.4.2: Structure of the Hamiltonian of a 3-site cluster, with $D_H = 64$.

into $\sqrt{k}$ individual segments [39]. Since only a limited number of segments is affected by an update, the remaining can be left untouched, reducing the number of matrix multiplication from $O(k)$ to $O\left(\sqrt{k}\right)$. More advanced techniques have been employed as well, involving self-balancing binary trees [39] or skip lists [102].

Besides the evaluation of the trace of operators $A[C]$, the other part, which contributes to the weight of a certain configuration C is the determinant $D[C]$ of the hybridization function matrix

$$\Delta = \begin{pmatrix} \Delta_{\alpha_1\beta_1}(\tau_1 - \tau_1') & \cdots & \Delta_{\alpha_1\beta_n}(\tau_1 - \tau_n') \\ \vdots & & \vdots \\ \Delta_{\alpha_n\beta_1}(\tau_n - \tau_1') & \cdots & \Delta_{\alpha_n\beta_n}(\tau_n - \tau_n') \end{pmatrix} \tag{1.4.29}$$

In principle, the evaluation of the determinant of the matrix scales like the cube of the expansion order n. However, by inspection one notices, that the updates described above usually change the matrix only at a very limited number of positions. The rank of the update is $k \ll n$. Most of the rows and columns remain unchanged. This can be exploited to reduce the computational complexity of evaluating the determinant to be quadratic in n by employing fast updates [39].

The self-energy is a very important quantity, in particular in DMFT applications. However, inverting the Dyson equation and calculating the self-energy from the CT-HYB results for the Green's function, i. e.

$$\Sigma(i\omega) = \left(G^{(0)}(i\omega)\right)^{-1} - \left(G(i\omega)\right)^{-1}, \tag{1.4.30}$$

has the disadvantage of introduces strong statistical noise at large frequencies. The reason is, that the interacting and non-interacting Green's function are the same asymptotically, which amplifies the statistical error for large frequencies. This can be overcome by an improved estimator for the self-energy developed in Ref. 42. It is based on the equations-of-motion approach

$$\begin{aligned}\Big(i\omega - \varepsilon_0\Big) G_{\alpha\alpha}(i\omega) &= 1 + \sum_{\beta} \Gamma_{\beta\alpha}(i\omega) \\ \Leftrightarrow G(i\omega) &= G^{(0)}(i\omega) + G^{(0)}(i\omega)\Gamma(i\omega)\end{aligned} \tag{1.4.31}$$

where Γ is a higher-order correlation function.

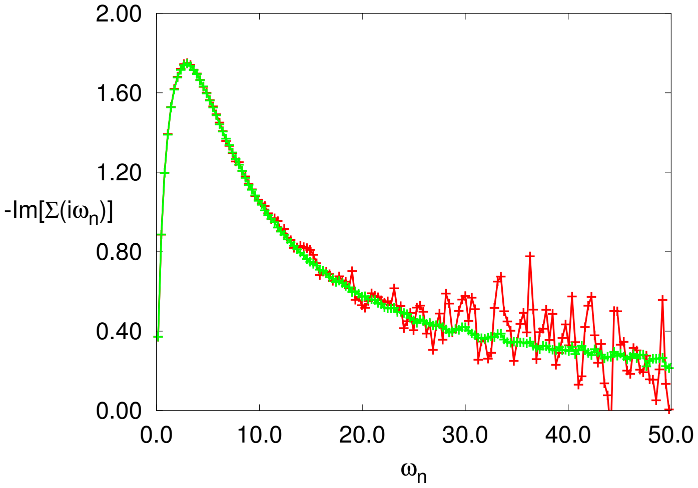

Figure 1.4.3: Self-energy obtained by the conventional method based on Eq. (1.4.30) (red), and by the improved estimator based on Eq. (1.4.32) (green). For $\omega_n > 10$ the first starts to exhibit substantial statistical error, while the improved estimator yields much better results.

The Dyson equation connects this expression to the self-energy, i. e.

$$\begin{aligned}G(i\omega) &= G^{(0)}(i\omega) + G^{(0)}(i\omega)\Sigma(i\omega)G(i\omega) \\ \Rightarrow \Sigma(i\omega) &= \Gamma(i\omega)\Big(G(i\omega)\Big)^{-1}\end{aligned} \tag{1.4.32}$$

Equations (1.4.30) and (1.4.32) are formally equivalent. However, because in the latter approach the self-energy is given by the ratio of two noisy quantities, it is more stable against numerical uncertainty. The significant increase in data quality by employing the improved estimator is shown in Fig. 1.4.3. Another advantage of this method of calculating the self-energy is that it yields the correct non-interacting $U = 0$ limit, namely $\Sigma = 0$. To reap these benefits, one has to measure the correlation function Γ in addition to the Green's function G. This is only feasible for models with density-density interactions:

$$\begin{aligned} \hat{\mathcal{H}}_i^{(I}) &= \sum_{\alpha,\beta} U_{\alpha\beta} \hat{\mathrm{n}}_\alpha \hat{\mathrm{n}}_\beta \\ \Rightarrow \Gamma_{\alpha\beta}(\tau - \tau') &= U_{\alpha\beta} \, \langle \hat{\mathrm{T}} \, \hat{\mathrm{n}}_\alpha(\tau) \, \hat{\mathrm{f}}^\dagger_\beta(\tau) \, \hat{\mathrm{f}}_\beta(\tau') \rangle. \end{aligned} \tag{1.4.33}$$

In this case, Γ can be obtained quite easily from the Green's function matrix.

$$\Gamma_{\alpha\beta}(\tau - \tau') = U_{\alpha\beta} \, \langle\!\langle \sum_{i,j} \delta_{\alpha,\alpha_i} \, \delta_{\beta,\beta_j} \, \tilde{\delta}(\tau - \tau', \tau_i - \tau'_j) \, \hat{\mathrm{n}}_\alpha(\tau_i) \, (\Delta^{-1})_{ij} \rangle\!\rangle$$

Note that another improved method of measuring the Green's function was proposed, which yields better results than the standard approach, in particular at small expansion orders and at high frequencies [8].

1.4.3 Analytical Continuation

The quantum Monte Carlo method yields all quantities on the imaginary time or imaginary frequency axis. In contrast, experimentals and other numerical methods yield results on the real axis. In order to derive real-frequency results from quantum Monte Carlo, one has to resort to some kind of analytical continuation.

The connection between the imaginary time Green's function $G(\tau)$ or imaginary frequency Green's function $G(i\omega_m)$ and the spectral density $A(\omega)$ or real frequency Green's function $G(\omega + i0^+)$ is given by

$$\begin{aligned} G(\tau) &= \int d\omega \, A(\omega) \, \underbrace{\frac{\exp(-\tau(\omega - \mu))}{1 + \exp(-\beta(\omega - \mu))}}_{K(\tau,\omega)} \\ G(i\omega_m) &= \int d\omega \, A(\omega) \, \underbrace{\frac{1}{i\omega_m - \omega}}_{K(i\omega_m,\omega)} \\ \text{where} \quad A(\omega) &= -\pi^{-1} \, \mathrm{Im} \left[G(\omega + i0^+) \right]. \end{aligned} \tag{1.4.34}$$

Equation (1.4.34) represent an integral transform of the spectral function $A(\omega)$ with a kernel $K(\tau, \omega)$ and $K(i\omega_m, \tau)$, respectively.

This relations have to be inverted, i. e. deconvoluted, in order to obtain $A(\omega)$ from $G(\tau)$. This is an ill-posed problem [98], since many different spectral functions $A(\omega)$ exist, which fit the data equally well. Hence, direct inversion of the kernel K by least-squares fitting is unstable [12], i. e. the result is extremely sensitive to small errors in the initial data $G(\tau)$.

One method successfully employed for the analytical continuation of QMC results like the Green's function is the Maximum Entropy method (MaxEnt) [98]. It infers the most probable spectral function from the data using Bayesian methods. In the process, MaxEnt is able to take prior information on the properties of the spectral function into account, in particular positivity and moments M_n

$$\begin{aligned} A(\omega) &\geq 0, \\ M_n &= \int d\omega\, \omega^n A(\omega), \\ \text{e.g.}\quad M_0 &= 1. \end{aligned}$$

In addition, it provides an error estimation based on the statistical uncertainties of the input data $G(\tau)$ given by the standard deviation $\sigma(\tau)$ or covariance $\mathrm{cov}(\tau, \tau')$.

The central equation of the MaxEnt method is Bayes' theorem

$$\underbrace{P\,[A(\omega)|G(\tau)]}_{\text{posterior prob.}} \sim \underbrace{P\,[G(\tau)|A(\omega)]}_{\text{likelihood}}\ \underbrace{P\,[A(\omega)]}_{\text{prior prob.}} \tag{1.4.35}$$

which relates the probability of obtaining $A(\omega)$ conditional on the $G(\tau)$ data to the probability of observing $G(\tau)$ given $A(\omega)$ and the total probability of getting $(A\omega)$. MaxEnt works by maximizing the posterior probability, and in this sense yields the "best" or most probable spectral function $A(\omega)$ given the data $G(\tau)$. The likelihood and prior probability take the form

$$\begin{aligned} P\,[G(\tau)|A(\omega)] &\sim \exp(-\chi^2[A]/2) \\ P\,[A(\omega)] &\sim \exp(-\alpha^{-1} S\,[A]). \end{aligned} \tag{1.4.36}$$

Here $\chi^2[A]$ is the goodness-of-fit function [12],

$$\chi^2[A] = \int d\tau\, \sigma(\tau)^{-2} \left[\int d\omega\, K(\tau, \omega) A(\omega) - G(\tau) \right]^2$$

which estimates how good the data $G(\tau)$ can be reproducing by the spectral function $A(\omega)$. $S\,[A]$ is the information entropy

$$S\,[A] = \int d\omega\, A(\omega)\, \ln\left(\frac{A(\omega)}{D(\omega)}\right)$$

of the spectral function relative to the so-called "default model" $D(\omega)$, which is usually a completely flat spectral function $D(\omega) = 1/W$, where W is the bandwidth. While the χ^2 term favors a perfect fit to the data, the entropy term regularizes the spectral function by suppressing arbitrary structure, such that only features relevant for the reconstruction of $G(\tau)$ are kept. The parameter α plays the role of an artificial temperature, and controls the relative influence of the two terms.

In practice, MaxEnt is able to reproduce finer details close to the chemical potential, while at higher frequencies only much broader features are obtained [98]. In addition, the method has the tendency to yield overly smooth solutions [12]. In Ref. 93, the stochastic analytical continuation was proposed to overcome this shortcoming: By a stochastic averaging over a certain set of different spectral functions, each fitting the data equally well, a better final result can be obtained, and finer features can be resolved.

In Ref. 12 this approach was extended, by employing an analogy of the analytical continuation to a classical, interacting field theory. From this point of view, the MaxEnt method can be understood as the saddle point approximation to the field theory. By Monte Carlo sampling of all possible field configuration, parametrized by delta function random walkers, an improved estimate for the spectral function can be obtained. In addition, by running multiple simulations for different values of the parameter α in parallel, and constructing a final spectral function as a weighted average of the individual results, the method is able to resolve sharp peaks and gap edges much better than the conventional MaxEnt method. A formulation of the above approach in terms of Bayesian logic, getting rid of any free parameters and ad hoc assumptions, was published in Ref. 36.

An additional improvement, in particular in applications of DMFT, can be achieve by analytical continuation of the self-energy instead of the Green's function. As the self-energy is momentum-independent, instead of having to continue the results for each momentum-point to the real axis, only a single run is necessary. In addition, in calculating the spectral function, all effects of the bare band structure can be included analytically. The procedure detailed in the following was introduced in Ref. 112 and extended in Refs. 35 and 38.

Expanding the bare and full Green's function and the self-energy at high frequencies yields the expressions

$$G^{(0)}(i\omega) = \sum_n \frac{M_n^{(0)}}{(i\omega)^n} = \frac{1}{i\omega} + M_2^{(0)} \frac{1}{(i\omega)^{-2}} + O\left(\omega^{-3}\right) \tag{1.4.37}$$

$$G(i\omega) = \sum_n \frac{M_n}{(i\omega)^n} = \frac{1}{i\omega} + M_2 \frac{1}{(i\omega)^{-2}} + O\left(\omega^{-3}\right) \tag{1.4.38}$$

$$\Sigma(i\omega) = \sum_{n=0}^{\infty} \Sigma_n \frac{1}{(i\omega)^n} = \Sigma_0 + \Sigma_1 \frac{1}{i\omega} + O\left(\omega^{-2}\right)$$

$$\text{where} \quad M_n^{(0)} = \int d\omega\, \omega^n A^{(0)}(\omega). \tag{1.4.39}$$

$M_n^{(0)}$ are the moments of the interacting (non-interacting) spectral function, and the coefficients Σ_n can be obtained order by order from the Dyson equation (1.4.30) [38]. In particular, for the Hubbard model [112], but equally for the generalized PAM employed in Sec. 2.2, in the paramagnetic phase the first two coefficients read

$$\begin{aligned}\Sigma_0 &= \frac{U}{2}\langle n\rangle,\\ \Sigma_1 &= \frac{U^2}{4}\langle n\rangle(2-\langle n\rangle).\end{aligned}$$

The expression $\langle n\rangle$ is the total occupation of correlated sites.

Therefore, the idea is to subtract the Hartree term Σ_0 and to rescale the remaining expression by Σ_1 to obtain a quantity Σ' which fully resembles a Green's function:

$$\Sigma'(i\omega) = \frac{\Sigma(i\omega)-\Sigma_0}{\Sigma_1} \sim \frac{1}{i\omega} \tag{1.4.40}$$

The quantity Σ' can be fed into the analytical continuation just like a Green's function, since it can be represented by a spectral function $A_S(\omega)$ in the very same way:

$$\Sigma'(i\omega) = \int d\omega'\, A_S(\omega')\frac{1}{i\omega-\omega'}.$$

Having obtained $A_S(\omega)$ from the analytical continuation, one readily calculates $\Sigma'(\omega+i0^+)$, and inverting Eq. (1.4.40) finally yields $\Sigma(\omega+i0^+)$. Via the Dyson equation (1.4.30) one can calculate the momentum-resolved Green's function on the real frequencies axis.

2 Application to Heavy Fermion Systems

2.1 Bilayers of He-3

2.1.1 Introduction

A prominent example for a Fermi liquid is bulk He-3. At very low temperatures, it forms a liquid of coherent quasiparticles [75], which are strongly renormalized due to correlation effects. In addition, since there is no crystal lattice, there is no coupling to lattice excitations, and since He-3 atoms are neutral, the long-range Coulomb interaction is absent [24]. This is in stark contrast to electronic Fermi liquids in metals.

In Sec. 2.1.2, an overview is given on experimental investigations of different He-3 systems. Section 2.1.3 summarizes previous model studies of the He-3 bilayer system. Next, Sec. 2.1.4 introduces the approach employed here and presents some details of the methods to investigate the model. What follows is the presentation of the numerical results. While Sec. 2.1.5 deals with the heavy fermion phase, in Sec. 2.1.6 results are presented which exhibit clear signatures of a first-order phase transition taking place in this system. Note that part of these results were published in the paper J. Werner and F. F. Assaad, Phys. Rev. B **90**, 205122 (2014).

2.1.2 Experimental Results

This section is devoted to the presentation of some experimental results for layered systems of He-3, with particular emphasis on bilayers. Since He-3 atoms consist of two protons and one neutron, they have a residual nuclear spin of 1/2; that is, they are fermions. This is in contrast to He-4, which is bosonic.

At the same time, He-3 atoms are neutral. Hence, the long-range Coulomb interaction does not play a role here. This makes systems of He-3 a very interesting playground to study fermions, and in particular Fermi liquid behavior.

While bulk He-3 is a strongly renormalized Fermi liquid which has been investigated extensively [75], the possibility of preparing thin layers of He-3 on top of a variety of substrates opens up the way to study different realizations of the Fermi liquid state in two dimensions. The relevant parameters in these experiments are the choice of the substrate and the amount of He-3 applied. While the substrate provides a surface potential and, depending on the setup, couples to the He-3 layers to different extent, the density of He-3 atoms tunes the relative strength of kinetic energy and interactions.

The experimental results discussed here were obtained in the group of John Saunders at the Royal Holloway University of London, and were published by M. Neumann et al. in Refs. 72 and 73.

The setup employed in the experimental investigation involves a substrate of graphite, on top of which two completely filled layers of superfluid He-4 were grown. On top of that, different amounts of He-3 were applied. The resulting layer structure is depicted in Fig. 2.1.1. The graphite and completely filled He-4 bilayer provide a periodic potential for the He-3. Otherwise there is a negligible coupling between the top-most He-4 layer and the He-3 layers [72].

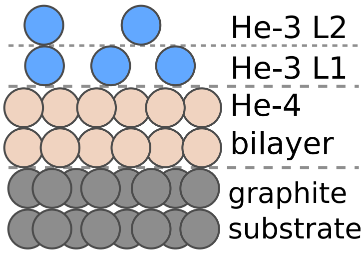

Figure 2.1.1: Schematic layer stacking of layers of He-4 and He-3 on a graphite substrate. Figure adapted from Ref. 73.

The experimental control parameters were the density of He-3 atoms $n_3 = 4.0 \ldots 12.0\,\mathrm{nm}^{-2}$ and the temperature T, which was varied in the range from 100 mK down to less than 1 mK. As a function of these two parameters, the phase diagram of the He-3 system was mapped out. The different phases were identified and characterized by measurements of the heat capacity $c(T)$ and measurements of the total magnetization $M(T)$.

2.1.2.1 Heavy Fermion Phase

The phase diagram, which summarizes the experimental findings, is shown in Fig. 2.1.2. At a density of $n_3 = n_{\mathrm{L2}} \approx 6.3\,\mathrm{nm}^{-2}$, where the first layer is completely filled, the atoms start to populate the second layer. Further increasing the density changes the number of particles in the second layer, while the first-layer density stays constant. The hybridization of the two layers leads to a crossover from an incoherent phase at high temperatures, where the layers are decoupled, to a coherent Fermi-liquid state at low temperatures. The Fermi liquid is made of quasiparticles of composite character, which originate in the spin-flip scattering of the second-layer fermions off the first-layer fermions; that is, the Kondo effect. This mechanism screens the first-layer local moments, which dissolve in the bath of second-layer, delocalized states.

The energy and temperature scale around which the crossover takes place is the coherence temperature T_{coh}. With increasing filling, T_{coh} is found to be suppressed. As a consequence, the effective mass of the quasiparticles $m_{\mathrm{eff}} \sim 1/T_{\mathrm{coh}}$ increases, leading to a heavy-fermion state. The heat capacity develops a maximum at a temperature T_0, and is linear at temperatures $T \ll T_0$. The linear coefficient of the heat capacity $\gamma \sim m_{\mathrm{eff}}$ increases with filling, thus signaling the heavy-fermion character of the phase. Meanwhile, the behavior of the small-field

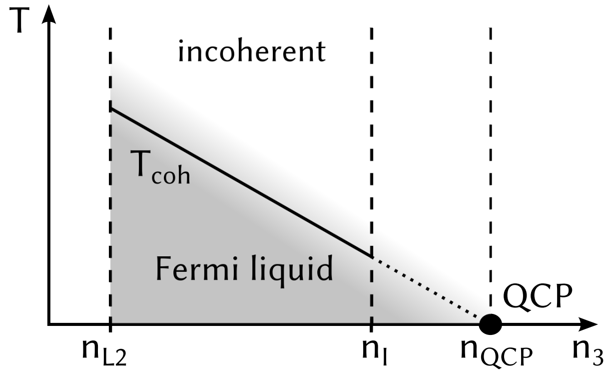

Figure 2.1.2: Phase diagram of the He-3 bilayer. The second layer is established at a filling $n_3 = n_{L2}$. With increasing filling, the Fermi liquid coherence scale is suppressed, and by extrapolation vanishes at a quantum critical point located at $n_3 = n_{QCP}$. In the range $n_I < n_3 < n_{QCP}$, an anomalous intervening phase is observed. Figure adapted from Ref. 73.

magnetization changes from a Curie-law behavior at high temperatures, which is characteristic of local moments, to a Pauli behavior below T_{coh}, which is consistent with a Fermi liquid.

2.1.2.2 Quantum Criticality and Intervening Phase

With rising filling, the coherence scale T_{coh} becomes smaller. This results in a shift of the maximum of the heat capacity T_0 to lower temperatures, and an increase of the linear coefficient γ. By extrapolation, both T_0 and the inverse effective mass vanish at a density $n_3 = n_{QCP} = 9.9/nm^2$. The critical exponents with respect to $\delta = 1 - n/n_{QCP}$ are $m_{\text{eff}} \sim \delta^{-1}$ and $T_0 \sim \delta^{\alpha}$ with $\alpha = 1.7 \pm 0.1$.

Therefore, at n_{QCP} the Kondo screening of the first-layer moments breaks down, and the quasiparticle fraction $Z \sim 1/m_{\text{eff}}$ vanishes at a quantum critical point. At the QCP, an orbital-selective Mott transition, which affects the first layer, takes place. The localization transition and the breakdown of the Kondo effect leave behind a system of two decoupled layers: The first layer hosts localized moments, which interact via magnetic exchange, while the second layer is an itinerant overlayer, i. e. a two-dimensional Fermi liquid.

At a lower filling $n_I \approx 9.2/nm^2 < n_{QCP}$, the heat capacity develops a second maximum at higher temperatures. At the same time, there is a strong increase of the magnetization at the lowest temperatures. It is even larger than one would expect from unscreened, isolated local moments. In the experimental work, this range of fillings was termed *intervening phase*.

2.1.2.3 Discussion

As the experiments presented above clearly demonstrate, layered systems of He-3 can give rise to unique Fermi liquid states, including heavy fermions. In the particular case relevant here, the first-layer fermions represent the almost localized, strongly interacting degrees of freedom, while the fermions in the second layer are delocalized and weakly interacting. In solid state heavy fermion compounds, the interplay between these two types of fermions gives rise to the heavy fermion behavior. The results of the above experiments can be equally interpreted as heavy fermion physics. Indeed, the Sommerfeld coefficient of the specific heat grows with increasing filling, which signifies an enhancement of the mass renormalization of quasiparticles due to strong correlations.

By extrapolation of the experimental results, the vanishing of the inverse effective mass and related quantities was proposed to take place at a quantum critical point. However, the Kondo breakdown QCP could not be studied directly in the experiments.

An additional, very interesting ingredient which comes into play in He-3 is the magnetic exchange interaction. In the interpretation of the experimental results, it becomes dominant beyond the QCP, making the first layer a two-dimensional magnet of coupled magnetic moments. However, as the large magnetization in the intervening phase suggests, the magnetic exchange already comes into play prior to the QCP.

2.1.3 Theoretical Works on He-3 Bilayers

Following the experiments on He-3 bilayers, a series of theoretical investigations of suitable microscopic models were conducted. In Refs. 15, 16 and 86, the bilayer was modeled by a Periodic Anderson Model. In addition, an interlayer repulsion was included in the model besides the Hubbard interaction. The hard-core character of the atoms was taken into account in a slave boson treatment of the infinite U limit.

The first-layer fermions were found to be close to a Mott transition, with strong correlation effects. As a function of filling, a sudden drop to zero of the slave boson amplitude was observed. This quantity encodes the renormalization of the hybridization. It was argued, that the vanishing of the effective hybridization marks the physical QCP, where the Kondo effect breaks down. This QCP preempts the experimentally found quantum critical point.

In Refs. 13 and 14, a different model for bilayers of He-3 was investigated by means of Cellular DMFT. The Hubbard interaction U was chosen sufficiently large to suppress the double occupancy and to resemble the hard-core repulsion. The study of different cluster sizes revealed a significant difference between clusters with an odd or even number of sites. For odd cluster sizes, there is always a crossover from the high-temperature phase with a small Fermi surface volume to the low-temperature, heavy fermion phase with a large Fermi surface volume. As a function of filling, the crossover scale T_{coh} and corresponding quasiparticle residue decrease smoothly.

In contrast, the even cluster sizes exhibit a discontinuous, orbital-selective Mott transition of the first layer at a critical value of the chemical potential μ_c. Across the transition, there is a jump in the Fermi surface volume, which signals that the first-layer fermions drop out of the Fermi surface count. In a filling controlled situation, which is the case in the experiments, this density-driven first-order transition translates to a phase separation.

In this approach, magnetic exchange interactions are dynamically generated, which couple the local moments antiferromagnetically. Hence, the different behavior for even cluster sizes results from the competition of the different possibilities to screen the local moments. While the Kondo effect results in the formation of composite quasiparticles, it breaks down at μ_c. Instead, intralayer singlets generated from first-layer fermions become more favorable, and supersede the interlayer Kondo singlets. However, the antiferromagnetic coupling seems to be an artifact of the method used. As argued below, in He-3 bilayers the three-particle ring exchange is dominant, which generates an effective ferromagnetic coupling.

2.1.4 Ring Exchange Periodic Anderson Model

The starting point for the model of He-3 bilayers is the generalized Periodic Anderson Model (PAM) (1.1.14), which was introduced in Sec. 1.1.5 as a prototypical model for heavy fermions. The operators $\hat{\mathrm{f}}_{k,\sigma}$ are identified with first-layer fermions, while $\hat{\mathrm{c}}_{k,\sigma}$ represent particles in the second layer.

Following Refs. 13 and 14, the model is considered on a triangular lattice. The layers are stacked in such a way, that the atoms are closed-packed, resembling the stacking of billiard balls. Within each layer, a hopping between neighboring sites with a layer dependent hopping amplitude $t_{c,f}$ is introduced. The hybridization of amplitude V is interpreted as an interlayer hopping. Due to the geometrical arrangement of lattice sites, the fermions of one layer can hybridize with three nearest sites on the opposite layer. The spatial arrangement of He-3 atoms and the hopping processes included in the model are depicted in Fig. 2.1.3.

The corresponding hopping part of the model Hamiltonian can be written in momentum space in the form of Eq. (1.1.15), which is reproduced here for convenience,

$$\hat{\mathcal{H}}_0 = \sum_k \begin{pmatrix} \hat{\mathrm{c}}_k^\dagger & \hat{\mathrm{f}}_k^\dagger \end{pmatrix} \begin{pmatrix} t^{(c)}(k) & V(k) \\ V^\dagger(k) & t^{(f)}(k) \end{pmatrix} \begin{pmatrix} \hat{\mathrm{c}}_k \\ \hat{\mathrm{f}}_k \end{pmatrix}. \tag{2.1.1}$$

Note that $\hat{\mathcal{H}}_0$ is diagonal in spin, so that the hopping and hybridization matrices are diagonal matrices as well.

Each fermion species has a dispersion which results from the intra-layer hopping. In addition, there is a momentum-dependent hybridization, which mixes different layers. They are

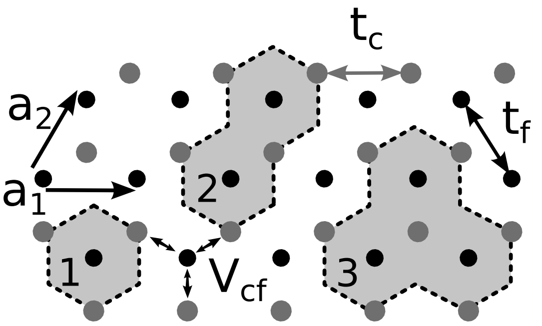

Figure 2.1.3: Spatial arrangement of He-3 atoms in the bilayer. The a_i are the lattice unit vectors. Second-layer sites (gray) are on top of and shifted with respect to sites in the first layer (black). The double arrows indicate hopping processes within layers with amplitude $t_{c,f}$ and hybridization processes with amplitude V_{cf}. The shaded regions represent the cluster geometries employed, containing one (1), two (2) and three (3) correlated first-layer sites.

given by

$$\begin{aligned} \varepsilon_c(k) &= -2t_c\,\gamma(k) \qquad (2.1.2)\\ \varepsilon_f(k) &= \varepsilon_0 - 2t_f\,\gamma(k)\\ V(k) &= V_{cf}\,\sqrt{3+2\gamma(k)}\\ \text{where}\quad \gamma(k) &= \cos(k\cdot a_x)+\cos(k\cdot a_y)+\cos(k\cdot a_x - k\cdot a_y). \end{aligned}$$

Here, the a_i are the vectors, which span the unit cell in real space, while ε_0 is the difference in binding energy between the two layers. The hopping parameter $t_c = t = 1$ is taken as the reference energy. Finally, the resulting eigenenergies of the hopping Hamiltonian are

$$E^{\pm}_{k,\sigma} = \frac{1}{2}\left(\varepsilon_c(k)+\varepsilon_f(k) \pm \sqrt{(\varepsilon_c(k)-\varepsilon_f(k))^2 + 4|V(k)|^2}\right). \qquad (2.1.3)$$

In Fig. 2.1.4, the first Brillouin zone of the reciprocal lattice with the high-symmetry points Γ, K and M is shown, as well as the bare dispersion $\varepsilon_c(k)$.

Concerning the interaction part of the Hamiltonian, two aspects have to be taken into account, which are described in detail in Ref. 88.

The first is the hard-core repulsion, which prevents the interpenetration of electron shells. A Lennard-Jones potential with a hard-core diameter of $d_{\mathrm{He}} = 2.14\mathring{A}$ and a weakly attractive tail phenomenologically describes the interaction of two atoms of He-3 [88]. The hard-core constraint of the atoms upon close approach can be captured in a lattice model quite nicely by introducting a very large local repulsion, i. e. a Hubbard term with a very large U parameter. In

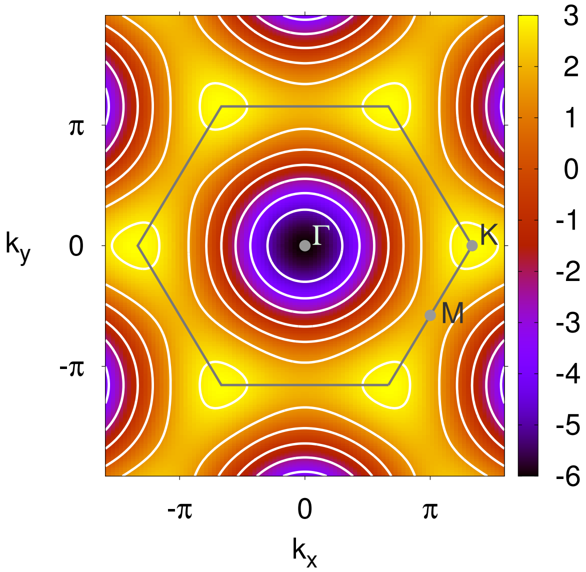

Figure 2.1.4: First Brillouin zone of the reciprocal space of a triangular lattice, with indicated high-symmetry points Γ, K and M. The bare dispersion $\varepsilon_c(k)$ is shown with color code.

fact, it is reasonable to take the limit $U \to \infty$. Thus, double occupation of lattice sites is strictly forbidden. This allows to project out the corresponding states, which results in a reduction of the local Hilbert space size from four to three states, as mentioned in Sec. 1.4.2.6.

The second interaction mechanism in He-3 is magnetic ring exchange of multiple particles. In fact, there is a whole hierarchy of n-particle ring exchange processes, which can be visualized as permutations of atoms, see Fig. 2.1.5.

Starting from a tightly packed lattice, no exchange at all is possible, essentially because the surrounding atoms not involved have to be pushed out of their equilibrium positions. However, the Lennard-Jones potential barrier prevents particles from coming too close to each other.

By slowly increasing the separation between particles, the potential barrier is lowered. Of the exchange processes discussed here, the four-particle exchange is the first, which becomes possible. Increasing the lattice spacing further, also three-particle exchange takes place, while two particle exchange is frustrated up to an even larger lattice spacing. Therefore, geometry favors higher-order processes. On the other hand, higher-order exchange becomes increasingly unfavorable due to the length of the path between equilibrium positions.

As a result, exchange processes involving three- and four-particle are favored the most, depending on the geometry. In particular, in a triangular geometry, and in layered systems of only a few layers, three-particle exchange is dominant [88].

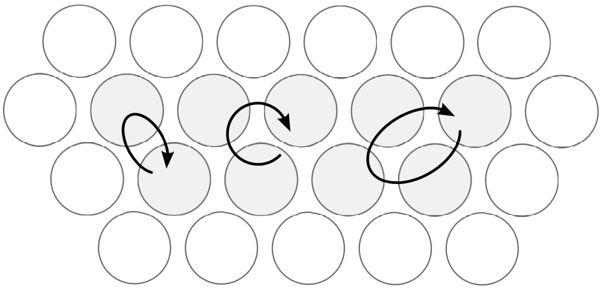

Figure 2.1.5: Ring exchange processes on a triangular lattice, involving two, three and four particles (filled circles), depicted as permutations of spheres. The more particles are directly involved in the exchange, the smaller is the influence on surrounding particles (white circles). Figure adapted from Ref. 88.

In general, exchange processes can be described in terms of spin permutations P_α. A suitable pseudo-Hamiltonian reads [88]

$$\hat{\hat{\mathcal{H}}} = -\sum_{\alpha} J_\alpha (-1)^{P_\alpha} P_\alpha \quad J_\alpha > 0. \tag{2.1.4}$$

It follows that exchange of an even number of particles, which is an odd permutation, is antiferromagnetic. In contrast, exchange processes involving an odd number of particles are even permutations, and are therefore ferromagnetic [105].

More explicitly, the two and three-particle exchange processes, written in terms of spin operators S, read

$$\begin{aligned} P_{ij} &= \frac{1}{2}(1 + S_i S_j) \qquad (2.1.5)\\ P_{ijk} &= P_{ij} P_{ik} = \frac{1}{4}\Big(1 + S_i S_j + S_j S_k + S_k S_i + i S_i (S_j \times S_k)\Big)\\ \Rightarrow \hat{\mathcal{H}}_{exch} &= -J \sum_{\langle i,j \rangle} S_i S_j\\ \text{where} \quad J &= \frac{1}{2}(6J_3 - J_2). \end{aligned}$$

Note that the imaginary part of P_{ijk} cancels in the summation over all possible permutations. Depending on the particular values of the exchange constants J_2 and J_3, the effective nearest-neighbor exchange is antiferromagnetic or ferromagnetic. As stated above, the three-particle ring exchange is dominant in the present case, so that the effective exchange constant $J > 0$.

The hard-core constraint and the ring exchange can be included in the model via an interaction Hamiltonian of the form

$$\hat{\mathcal{H}}_I = \lim_{U \to \infty} \frac{U}{2} \sum_{\alpha,i} \hat{\mathrm{n}}_{\alpha,i} \left(\hat{\mathrm{n}}_{\alpha,i} - 1\right) - J \sum_{\langle \{\alpha,i\},\{\beta,j\} \rangle} S_{\alpha,i} \cdot S_{\beta,j}. \tag{2.1.6}$$

α and β denote the layer, while i and j are lattice site indices. The notation $\langle\{\alpha, i\}, \{\beta, j\}\rangle$ denotes distinct pairs of neighboring sites within a single layer ($\alpha = \beta$) and on different layers ($\alpha \neq \beta$).

In order to facilitate the numerical investigation of the above model, it is assumed that all correlations involving fermions in the second layer can be neglected. This is justified as long as the filling of the second layer is much smaller than one; that is, half-filling. In this case, correlations in the second layer can result at most in a small renormalization of the band energies. Thus, what remains is a correlated first layer subject to the local repulsion U and nearest-neighbor magnetic exchange J, which is coupled to an uncorrelated second layer.

The non-local magnetic exchange can be included in the single-site DMFT only at the static mean-field level. As discussed in Sec. 1.3, this approach is able to describe a possible phase transition, but fails to capture the relevant fluctuations. It is therefore not appropriate in the present case. However, using a cluster extension of the DMFT allows to incorporate the ring exchange directly. In the following, the Cellular DMFT with N_c cluster sites is used for the investigation of the above model. Given the interaction part of the Hamiltonian with both hard-core constraint and magnetic ring exchange, the CT-HYB algorithm introduced in Sec. 1.4.2 is the cluster solver of choice.

Because the effective spin-spin interaction resulting from the ring exchange is included explicitly in the model, already the smallest non-trivial cluster with $N_c = 2$ captures an important part of the ring exchange physics, despite that fact, that it does not contain a single ring. Simulating larger clusters allows to systematically include larger parts of the non-local correlations. Hence, by comparing the results for different cluster geometries, it is possible to assess the error introduced by the truncation of the interactions.

In order to draw robust conclusions about the thermodynamic limit, a careful extrapolation of results for different cluster sizes to $N_c \to \infty$ is necessary [69]. However, with the proposed model making the use of the CT-HYB cluster solver necessary, the number of cluster sites N_c is severely limited. As it turned out during the simulation runs, even simulations for small clusters in the parameter regime of interest require extensive simulation time. This is due to another obstacle, the negative sign problem [108]. In particular, it prohibits the simulation from accessing very low temperatures for $N_c \geq 3$, as shown in Fig. 2.1.6. Therefore, only the cluster geometries shown in Fig. 2.1.3 could be investigated. As a consequence, the simulations are restricted to the cluster sizes $N_c = 1 - 3$, where $N_c = 1$ corresponds to the single-site DMFT. As indicated above, for the three-site cluster, the inverse temperature $\beta t \leq 50$, while for $N_c = 1$ and 2 inverse temperatures up to $\beta t = 60$ are simulated, and even higher values, i. e. lower temperatures, are in principle accessible.

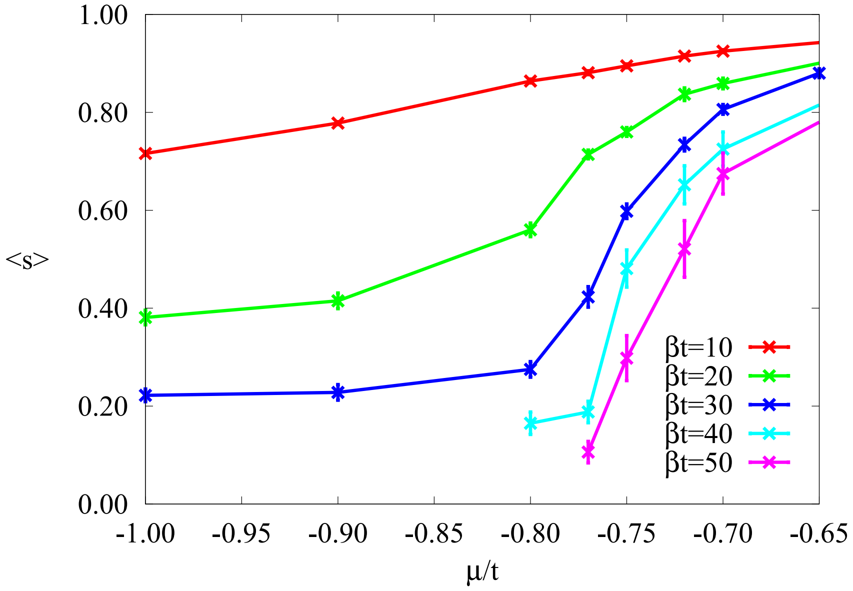

Figure 2.1.6: Average sign $\langle s \rangle$ for the cluster with $N_c = 3$ for different inverse temperatures β, as a function of chemical potential μ.

2.1.5 Numerical Results: Heavy Fermions

In the following, the model is investigated by systematically raising the chemical potential μ. With increasing μ, its conjugate variable, the filling, increases as well. To find signatures of a Fermi liquid, which develops at low temperatures, the first quantity studied here is the self-energy.

For a Fermi liquid, the imaginary part of the Matsubara self-energy vanishes linearly at the Fermi energy: $\mathrm{Im}[\Sigma](i\omega) \sim i\omega$. This is a consequence of the infinite lifetime of quasiparticles at the Fermi energy. In Fig. 2.1.7 the imaginary part of the local self-energy

$$\Sigma(i\omega) = \frac{1}{N}\sum_k \Sigma(k, i\omega) \tag{2.1.7}$$

is shown, for $N_c = 1 - 3$. Starting with the lowest values of μ/t, a linear regime appears at small frequencies. At larger values of μ, the linear behavior develops only at smaller frequencies. However, the last two data sets for each cluster size exhibit significant differences when compared to the other data. Except for the data at $N_c = 1$ and $\mu/t = 0.05$, they do not seem to obey the linear relationship at all. Instead they seem to extrapolate to a finite value as $i\omega \to 0$.

Before discussing these data points in more detail, first, another quantity is investigated, which can be equally used to identify a Fermi liquid state: The static magnetic susceptibility χ.

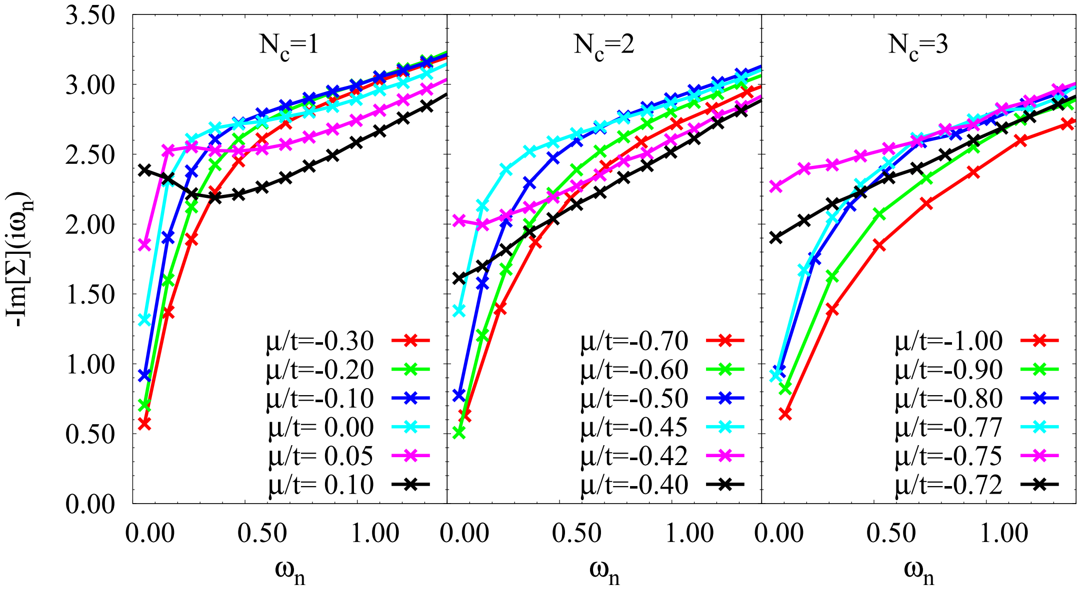

Figure 2.1.7: Imaginary part of the local self-energy at small Matsubara frequencies, for different cluster sizes N_c and chemical potential μ. The results shown for each parameter set correspond to the lowest temperatures attainable.

While the low temperature Fermi liquid state has a Pauli susceptibility, i. e. $\chi \sim$ const., at high temperatures the unscreened local moments exhibit a Curie-Weiss susceptibility according to Eq. (1.1.11). The results for the static magnetic susceptibility of the f-spins are shown in Fig. 2.1.8. Here, the cluster susceptibility is taken as an approximation to the corresponding lattice quantity, which becomes exact for large clusters:

$$\chi_f \approx \chi_f^{(C)} = \frac{1}{N_c} \sum_{i,j}^{N_c} \left\langle S_{f,i} S_{f,j} \right\rangle, \tag{2.1.8}$$

$$\text{where} \quad \langle S_{f,i} S_{f,j} \rangle = \int d\tau \left\langle S_{f,i}(\tau) S_{f,j}(0) \right\rangle$$

At high temperatures all data exhibit a linear dependence on temperature. This corresponds to a Curie-Weiss susceptibility, which is the expected behavior, given that at temperatures above the coherence scale the two layers are decoupled. Hence, the f-spins considered here represent localized moments, at least to a certain extent. Comparing the data with the idealized case of isolated spin-1/2 moments, in the single-site case the susceptibility is lowered by the residual charge fluctuations. These are due to inter- and intralayer hopping, which is not completely suppressed. For $N_c = 2$ and 3, at lower filling the susceptibility is also suppressed. However, with increasing particle number the susceptibility becomes enhanced compared to

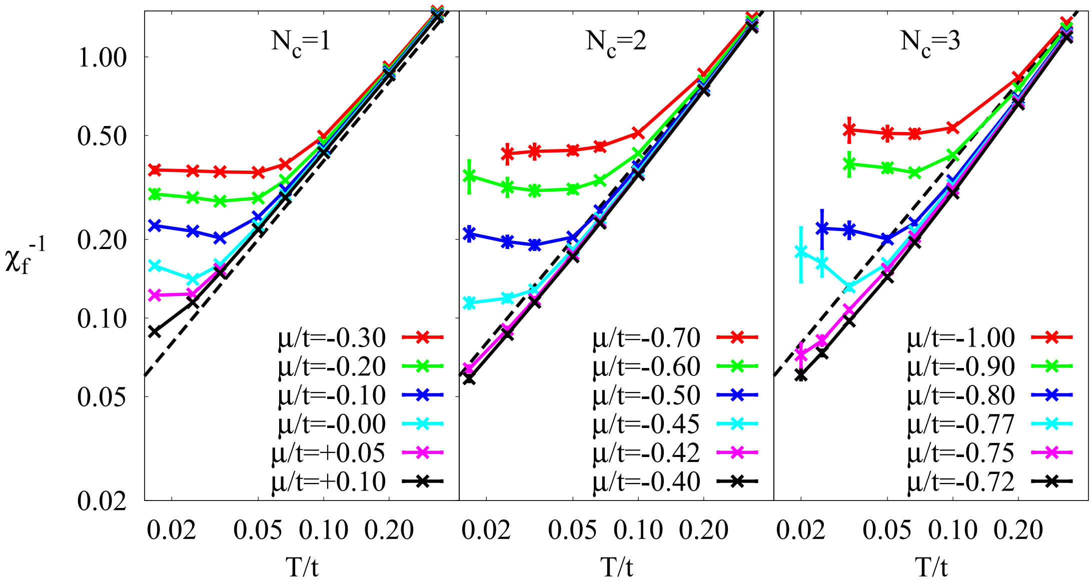

Figure 2.1.8: Static cluster f-spin susceptibility, for different cluster sizes N_c and chemical potential μ, as a function of temperature. The dashed line is the susceptibility of isolated spin-1/2 local moments; that is, a Curie law ($\Theta = 0$).

the isolated spin case. This is a consequence of the ring exchange between f-spins, which is becoming increasingly important at larger filling, while at the same time the residual screening due to hopping is more and more suppressed. In total, this gives rise to a positive ordering temperature or Weiss temperature θ.

At low temperatures most of the data start to deviate substantially from the linear behavior. This marks the crossover to the Fermi liquid as the temperature crosses the coherence scale T_{coh}. At $T \ll T_{\text{coh}}$ this leads to a constant susceptibility. With increasing filling, T_{coh} is shifted to lower temperatures, and the zero-temperature value of χ_f increases accordingly.

However, for $N_c = 2$ and 3, for the two last data sets, which correspond to the highest values of μ, the crossover is clearly absent. Instead, the data still follow the Curie-Weiss law with a positive Weiss temperature. Compared to the case of isolated moments, the susceptibility is enhanced due to the ring exchange.

To better quantify the evolution of the Fermi liquid coherence scale, the focus is again put on the self-energy. The linear coefficient at small frequencies is connected to the quasiparticle residue Z (c.f. Eq. (1.1.6)), which is approximated by the first Matsubara frequency value

$$Z \approx Z_M = \left(1 - \left. \frac{\text{Im}[\Sigma(i\omega_n)]}{\omega_n} \right|_{\omega_n = \omega_0 = \pi T} \right)^{-1}, \tag{2.1.9}$$

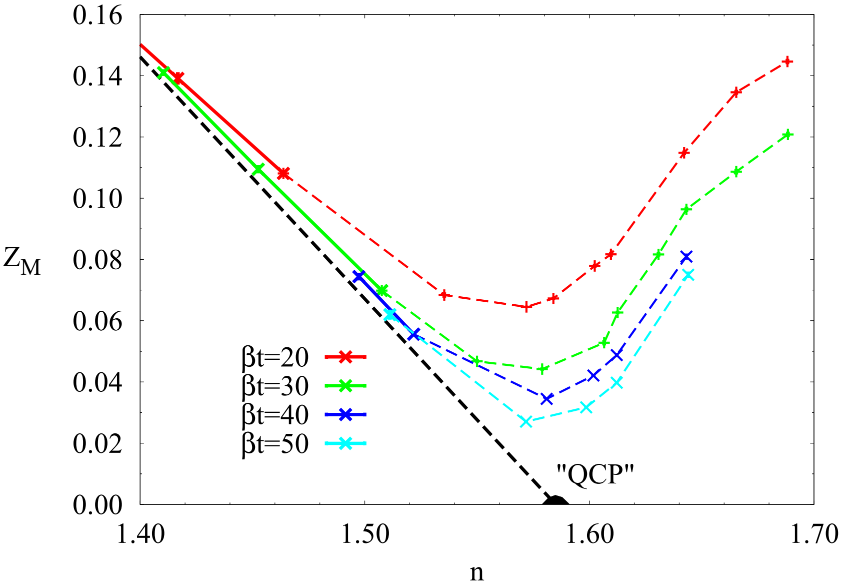

Figure 2.1.9: Approximate quasiparticle residue Z_M for different inverse temperatures, as a function of total filling. The dashed lines indicate results, where the imaginary part of the self-energy is not yet linear in frequency because of the high temperature or where Z_M is not well defined because the self-energy is not linear at all. The black, dashed line is a guide to the eye. It suggests the existence of a quantum critical point at $n \approx 1.58$.

As the temperature decreases, this quantity approaches the true quasiparticle residue, i. e. $Z_M(T \to 0) \to Z$, which is in turn related to the coherence scale and effective mass via

$$Z \sim T_{\text{coh}} \sim m_{\text{eff}}^{-1}. \tag{2.1.10}$$

In Fig. 2.1.9 the approximate quasiparticle residue Z_M is plotted for the cluster of size $N_c = 3$. For smaller filling up to $n \approx 1.5$, the values of Z_M for the inverse temperature investigated have already converged to the zero-temperature value Z. This is mirrored by the imaginary part of the self-energy being almost perfectly linear. Hence, the Fermi liquid is well established. However, with increasing filling the deviation at higher temperature from the converged result becomes more apparent, which results from the decreasing coherence temperature. This becomes equally manifest in the smaller Z values. At larger filling, as was visible already in the self-energy, the quasiparticles are not well-defined. As the self-energy is not linear, Z_M is meaningless. The corresponding values are nevertheless included in Fig. 2.1.9 for completeness, but differentiated by the use of dashed lines.

An extrapolation of the trend yields a vanishing Z and T_{coh} at a quantum critical point at $n \approx 1.58$. Simultaneously, the quasiparticle effective mass has to diverge, i. e. the Kondo effect breaks down. While the scenario of a Kondo breakdown QCP seems plausible, and is in good agreement with the conclusions from the experiments, there are other observables which have to be taken into account. This is the topic of the next section, while for the moment, the heavy fermion state is discussed a little further.

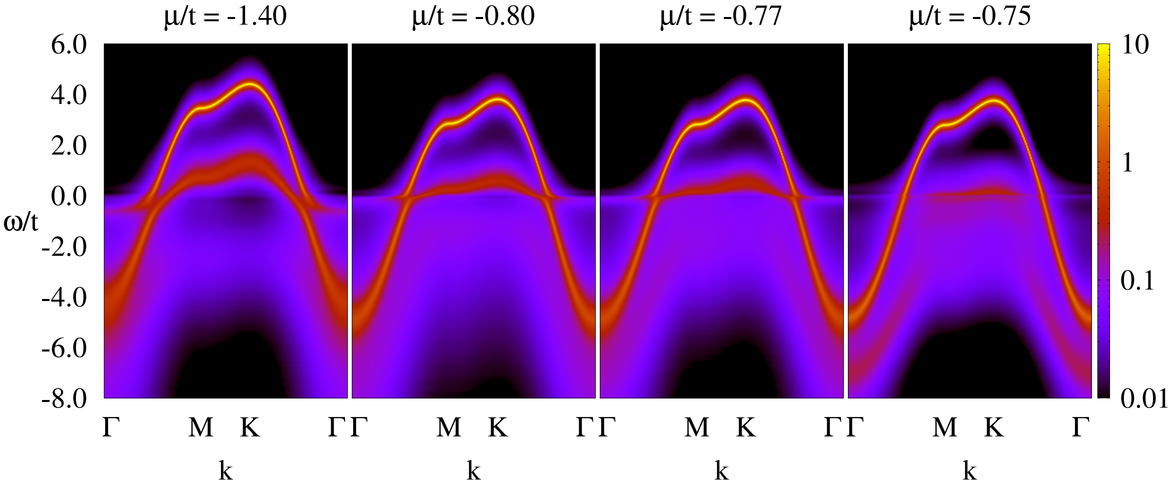

Figure 2.1.10: Momentum-resolved spectral function $A(k, \omega)$, for $N_c = 3$ and different values of the chemical potential μ. The inverse temperature is $\beta t = 40$, except for $\mu/t = -1.40$, where $\beta t = 20$.

The coherent heavy fermion state can be visualized quite nicely in the momentum-resolved spectral function $A(k, \omega)$. This quantity is obtained by analytical continuation of the lattice Green's function from the Matsubara frequencies to real frequencies. As Fig. 2.1.10 shows, the heavy quasiparticle states are located close to the chemical potential around $\omega = 0$, except for the last panel of Fig. 2.1.10. For $\mu/t = -1.40 \ll \mu_c$, the bandwidth of the quasiparticle band is quite large. This is also true for the coherence scale, since both quantities are closely connected. The bandwidth decreases considerably as the chemical potential is raised from $\mu/t = -1.40$ to $\mu/t = -0.77$, which is a consequence of the decrease of the coherence scale. There is also a small direct hybridization gap at the chemical potential, which prevents the crossing of the narrow heavy band and the wide second-layer band.

Since the quasiparticle residue is small ($Z \ll 1$), only little spectral weight is contained in the heavy fermion band. There is a broad, incoherent feature far below the chemical potential, where most of the spectral weight is concentrated.

In the last panel, where $\mu > \mu_c$, the heavy fermion feature is almost gone, as well as the hybridization gap at $\omega = 0$. In addition, the incoherent part of the spectrum has gained in intensity, i. e. spectral weight is shifted from the vicinity of the chemical potential to energies far below $\omega = 0$. In the case of a complete breakdown of the Kondo effect, the quasiparticle residue Z would go to zero, and the heavy quasiparticle band would have disappeared completely. However, as Fig. 2.1.10 shows, around the chemical potential some spectral weight is left, which suggests that some residual hybridization remains. As argued in the next section, this is merely an artifact of the approximation. For $N_c \to \infty$, the Kondo effect breaks down completely and the layers perfectly decouple.

2.1.6 Numerical Results: Phase Transition

In the preceding section, beyond a certain threshold value μ_c of the chemical potential, a rather abrupt change was observed in several physical properties. In the self-energy, the linear dependence on frequency was absent. Simultaneously, the f-moments remained unscreened, which became manifest in the spin susceptibility. In this section, this issue is investigated using additional observables.

First, in Fig. 2.1.11 the first-layer occupation $n_f = \langle \hat{n}_f \rangle$ is plotted. While the result is smooth for $N_c = 1$ at all temperatures, at lower temperatures the cluster results exhibit a strong increase of f-occupation in a narrow range of parameter values. Comparing $N_c = 2$ with $N_c = 3$, the increase in occupation becomes even steeper. This allows to define μ_c as

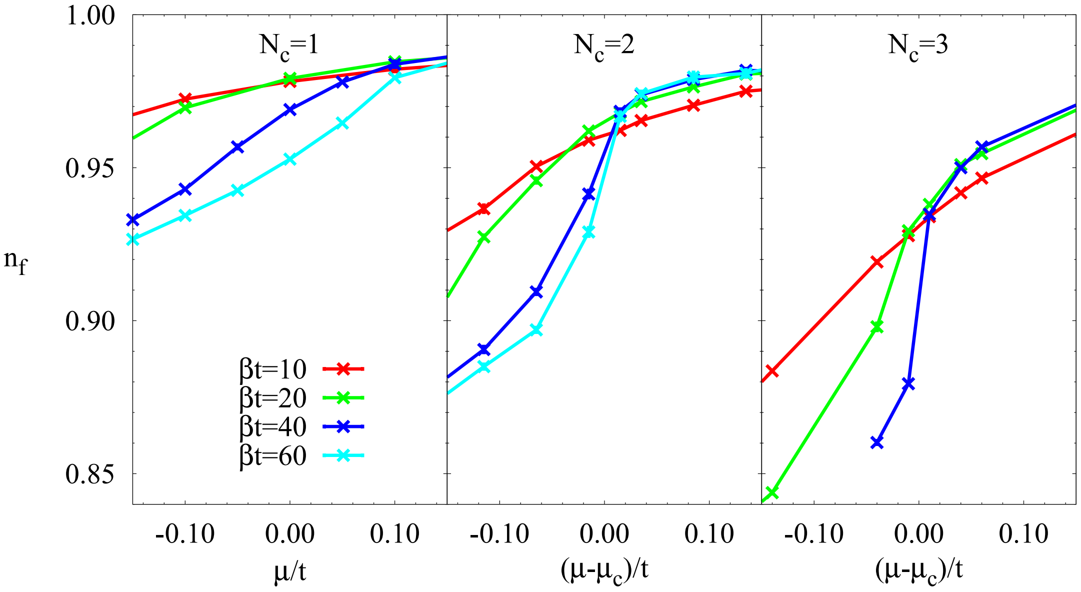

Figure 2.1.11: Occupation of the first-layer (f) sites, for the different cluster sizes N_c and inverse temperatures β, as a function of chemical potential μ. For $N_c = 2$ and 3 the chemical potential is shifted by a cluster size dependent constant μ_c, as explained in the main text.

the point of the steepest ascent at low temperatures. The corresponding values are given in Table 2.1.

cluster size N_c	$N_c = 1$	$N_c = 2$	$N_c = 3$
μ_c/t	-	-0.44(1)	-0.76(2)

Table 2.1: Point of steepest ascent of n_f with respect to μ, with the uncertainty in the last digit given in brackets.

Along these lines, in Fig. 2.1.12 the total occupation is shown. Here, the different clusters are compared at fixed temperatures. With increasing cluster size, the occupation is enhanced. In addition, going from high temperatures to low temperatures, a very strong increase can be observed for $N_c = 2$ and even more so for $N_c = 3$. By comparison with the black lines depicting $1 + n_c$, it becomes clear that this results from the strong increase of n_f at $\mu \approx \mu_c$. The second-layer occupation increases smoothly across this point. For $\mu > \mu_c$, the first layer is almost completely filled ($n_f \rightarrow 1$), so that $n \rightarrow 1 + n_c$.

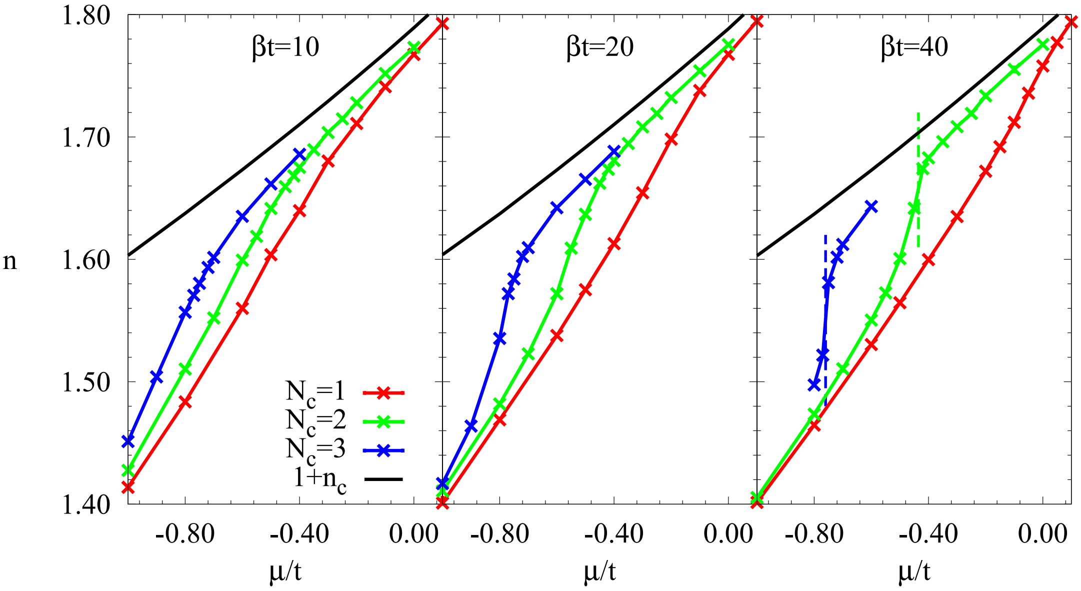

Figure 2.1.12: Total particle number $n = n_f + n_c$ for different inverse temperatures β and cluster sizes N_c, as a function of chemical potential μ. For comparison, $1 + n_c$ is plotted with black lines. The dashed lines in the right panel indicate the position of μ_c for $N_c = 2$ (green) and $N_c = 3$ (blue).

As both Figs. 2.1.11 and 2.1.12 show, the increase in n_f is steep. However, for all cluster sizes investigated here, it remains continuous. However, from comparing $N_c = 2$ and $N_c = 3$, it seems plausible that as $N_c \to \infty$, at μ_c a discontinuity develops.

In Fig. 2.1.13 the effective f-level position relative to the chemical potential μ,

$$\Delta\varepsilon_f = \varepsilon_0 + \mathrm{Re}[\Sigma(i\omega \to 0)] - \mu, \tag{2.1.11}$$

is plotted. It contains information about the effective renormalization of the bare f-level position ε_0 at low energies due to interaction effects, which is encoded in the zero-frequency real part of the self-energy. While for $N_c = 1$, there is a smooth decrease with increasing filling, for the larger clusters a strong drop of the effective f-level develops in a very narrow range of μ-values around μ_c. Thus, the strong increase of filling around μ_c can be understood by a sudden drop of the f-level to a value far below the chemical potential. Again the drop is more pronounced at lower temperatures and for the larger cluster size.

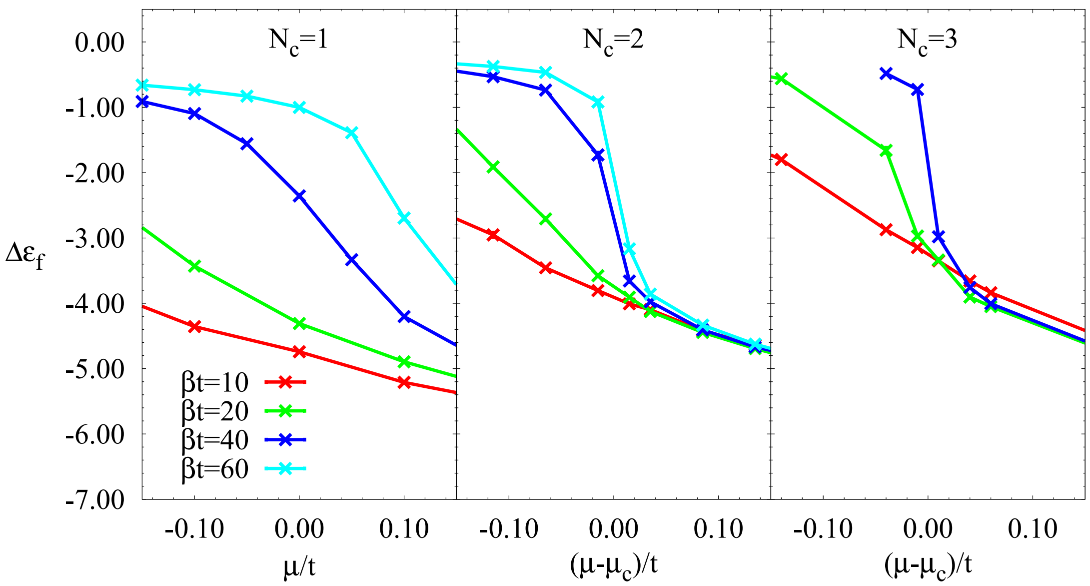

Figure 2.1.13: Effective f-level position $\Delta\varepsilon_f$ as defined in Eq. (2.1.11), for different inverse temperatures β and cluster sizes N_c, as a function of chemical potential μ.

As discussed in Sec. 1.4.2.3, the CT-HYB method allows to measure the contribution of individual cluster states to the cluster density matrix. The occupation of states grouped by sectors of particle number and z-component of the total spin is shown Fig. 2.1.14. Across μ_c, the contribution of different sectors changes significantly. In particular, comparing $\mu = -0.77t < \mu_c$ and $\mu = -0.75t > \mu_c$, the states with particle number $N = 3$ gain weight, while states with $N = 0-2$ contribute less. Thus, the number of particles in the cluster increases, which mirrors the jump in occupation observed above. For $N = 3$, the sector with a large z-component of the total spin gain the most. However, since no symmetry-breaking is allowed, states with large x-component or y-component equally contribute a larger proportion to the density matrix, so that the $S_z = \pm 1/2$ sectors contribute more as well.

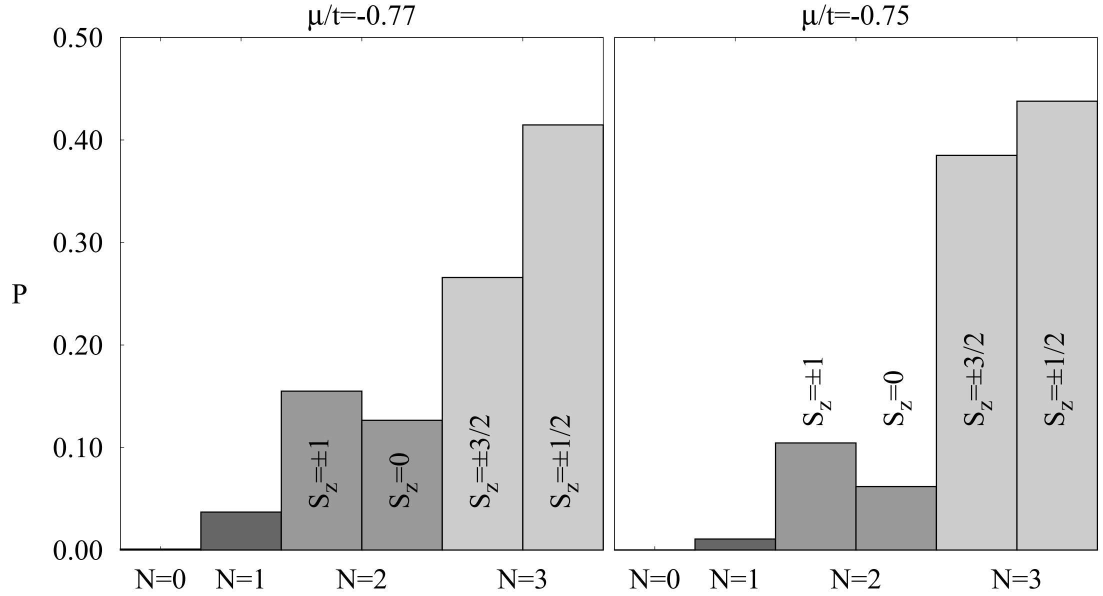

Figure 2.1.14: Occupation of different sectors of states for $N_c = 3$ at $\beta t = 40$. States with larger particle number and parallel alignment of spins gain weight across μ_c.

To learn more about the character of the putative phase transition, in the following the spin correlations in the effective cluster between neighboring first-layer sites are investigated. This observable is given by the equal-time correlation

$$\langle S_f S_f \rangle = \frac{1}{N_p} \sum_{<i,j>} \langle S_{f,i}(0)\, S_{f,j}(0) \rangle. \tag{2.1.12}$$

The sum runs over the N_p distinct pairs of neighboring sites $< i, j >$ in the cluster: $N_p = 1$ for two sites, and $N_p = 3$ for three sites. Due to the fact that $SU(2)$ symmetry is preserved, it follows that

$$\langle S_f S_f \rangle = 3 \langle S_f^z S_f^z \rangle.$$

Hence, it is sufficient to measure the correlation in the z-component. In Fig. 2.1.15 the spin correlation is plotted for the two- and three-site clusters. For $\mu < \mu_c$, with lower temperatures the spin correlation drops to a rather small value. This is a consequence of the almost complete screening of the local moments due to the Kondo effect. Crossing μ_c, the behavior changes:

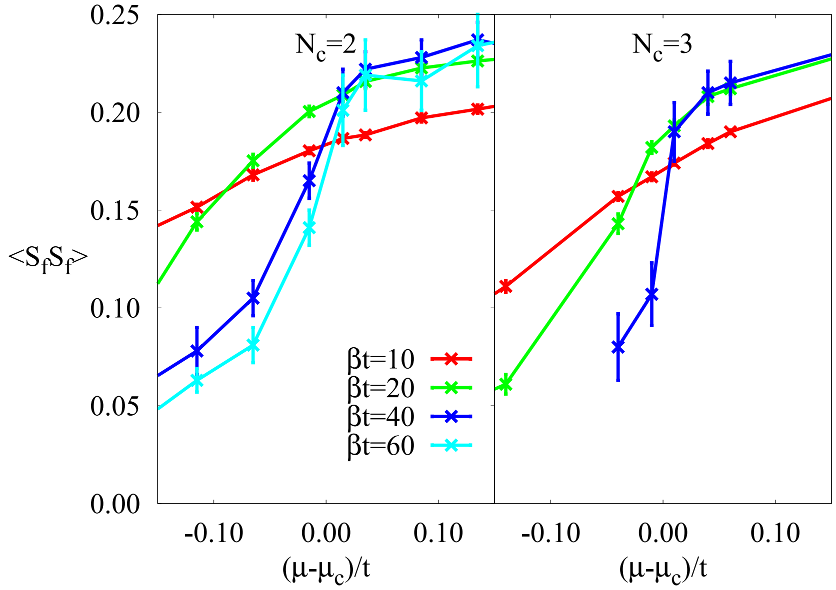

Figure 2.1.15: Spin correlation between neighboring f-sites on the cluster, for different cluster sizes N_c and inverse temperatures β, as a function of chemical potential μ. For perfectly aligned spins $\langle S_f S_f \rangle = 1/4$.

Now the spin correlation takes a large value down to the lowest temperature, which corresponds to a substantial positive, i. e. ferromagnetic correlation between neighboring spins. This strong enhancement of spin correlation happens across a very narrow μ-range around μ_c. It becomes more pronounced for lower temperatures and the larger cluster. Since a symmetry breaking is not allowed for in the simulations, a paramagnetic state is found at all fillings. However, after crossing $\mu > \mu_c$, strong ferromagnetic fluctuations appear, which could lead to a breaking of the symmetry.

This allows to conclude that a crossover from a heavy fermion state at small filling to a ferromagnetic state at large filling is observed, which takes place in a very narrow μ-range. This observation is consistent for both cluster sizes investigated. The ascent observed in the data for the f-occupation number and the spin correlation becomes even steeper for the larger cluster.

This suggests that extrapolating of the trends observed to the thermodynamic limit $N_c \rightarrow \infty$, the transition becomes discontinuous. Thus, the heavy fermion phase and a truly ferromagnetic state are separated by a discontinuous transition at a critical chemical potential μ_c.

2.1.7 Discussion

The numerical simulations of the PAM (1.1.12), adapted to the He-3 bilayers in Eq. (2.1.1) and Eq. (2.1.6), reveal a number of interesting observations. The main results are summarized in the phase diagram of Fig. 2.1.16.

First, the onset of the coherent Fermi liquid can be observed. It becomes manifest in a linear dependence of the self-energy on frequency. This is accompanied by a screening of the first-layer moments due to the Kondo effect, which becomes apparent in the spin susceptibility.

An analysis of the evolution of the quasiparticle residue Z with increasing filling reveals, that the coherence scale T_{coh} becomes increasingly suppressed. Hence, the effective mass $m_{\mathrm{eff}} \sim T_{\mathrm{coh}}^{-1}$ increases, and gives rise to a heavy Fermi liquid. This is in good agreement with the experimentally observed development of the heavy fermion state with increasing filling.

An extrapolation of the quasiparticle residue $Z \sim T_{\mathrm{coh}}$ leads to a putative Kondo breakdown QCP at a filling $n_{QCP} \approx 1.58$.

However, for values of the chemical potential larger than a threshold μ_c, the self-energy as well as the spin susceptibility deviate from the Fermi liquid behavior. In particular, the linear part of the self-energy is absent down to the lowest temperatures attainable. Meanwhile, the spin susceptibility follows a Curie-Weiss law. However, a phase transition is implausible for finite size clusters. Instead, the local moments at the cluster sites, which are coupled due to the ferromagnetic exchange J, eventually become screened. However, the coherence temperature is strongly suppressed for larger clusters, so that it cannot be accessed with the numerical method used here.

In conjunction with the disappearance of the Fermi liquid signatures, a rather steep increase in the filling of the first-layer (n_f) is observed for the cluster simulations around $\mu = \mu_c$. This behavior is absent in the single-site DMFT case. The increase becomes more pronounced at lower temperatures and for the larger cluster. This hints at a discontinuity in the occupation of the first-layer sites as $N_c \to \infty$, i. e. a first-order transition. The spin-spin correlation in the first-layer exhibits a similiar behavior; that is, a strong enhancement of short-ranged ferromagnetic spin fluctuations in a very narrow range of μ-values.

All the above points are consistent for the cluster sizes investigated. Hence, they hint at a first-order phase transition in the limit $N_c \to \infty$. The temperature scale for the screening of the local moments on the N_c cluster sites is increasingly suppressed, and vanishes in the thermodynamic limit. Hence, screening is not possible, and the Kondo effect breaks down in a discontinuous manner. In the process, the Fermi liquid state of composite quasiparticles is replaced by a ferromagnetic state of the first-layer localized moments, with the second layer as a fluid overlayer. The effective hybridization between the layers is completely suppressed, so that first and second layer are decoupled. On a finite size cluster, the transition is always a continuous crossover, leaving a small residual hybridization between the two layers.

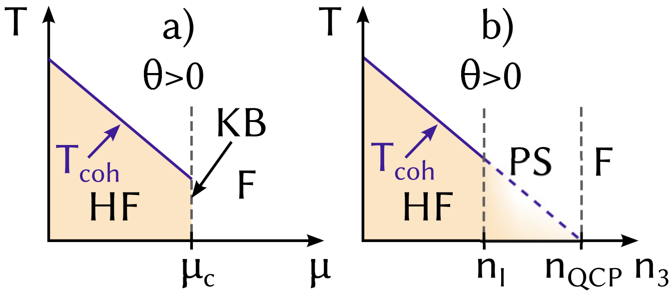

Figure 2.1.16: Phase diagram of the model for the He-3 bilayer. In the incoherent phase, there is a positive (ferromagnetic) Weiss temperature θ. Below the coherence temperature T_{coh}, the heavy fermion state (HF) forms. a) At a critical chemical potential μ_c, a first-order Kondo breakdown transition (KB) to a ferromagnetic state (F) takes place in the first layer. b) In terms of filling, the transition is mirrored by a phase separation (PS) for $n > n_I$. Extrapolation of the coherence scale yields a putative QCP at n_{QCP}.

The first-order transition is a consequence of the competition between Fermi liquid coherence, characterized by T_{coh}, and the ferromagnetic exchange with an effective coupling strength $J^* = J + J_{\mathrm{AF}}$. $J_{\mathrm{AF}} < 0$ is the antiferromagnetic coupling due to direct and indirect virtual exchange processes. As T_{coh} is suppressed with increasing filling, eventually the energy gain due to the ferromagnetic alignment of spins becomes comparable to or larger than the gain from forming composite quasiparticles. When this is the case, the ferromagnetic alignment of f-spins becomes favorable, and the Kondo effect breaks down.

By comparison with the experimental findings, the numerical results allow for the following conclusion. The intervening phase, which preempts the experimental QCP, can be understood as resulting from the first-order transition between two competing ground states: the Fermi liquid state at lower density and ferromagnetic state at higher density. In the simulations, the tuning parameter is the chemical potential, which couples to the density, while in the experiments the density is tuned directly. Translating the simulation results of a first-order transition at a critical chemical potential μ_c to a description in terms of the density (c.f. Fig. 2.1.16), it is concluded that the intervening phase is in fact the result of a phase separation. In this range of densities, the two phases coexist. The proportion each phase occupies depends on the filling. This interpretation is consistent with a continuous onset of a finite sample magnetization at the lowest temperatures, which is found for densities $n_3 \geq n_I$.

In summary, the model for bilayers of He-3 investigated here is able to capture important aspects of the experimental results. While at smaller filling the heavy fermion phase is recovered, at larger filling the consistent results for different cluster sizes strongly hint at a first-order transition in the thermodynamic limit. This allows to interpret the observed intervening phase at larger filling in terms of a phase separation.

2.2 Topological Kondo Insulators

2.2.1 Introduction

In heavy fermion systems, the relevant degrees of freedom are strongly correlated, almost localized fermions, e.g. f-electrons, and weakly correlated, delocalized fermions, e.g. conduction electrons. The two fermion species hybridize, giving rise to a coherent Fermi liquid state of composite quasiparticles. With increasing interaction strength, the quasiparticle effective mass is enhanced, while the width of the quasiparticle band decreases. Hence, the characteristic energy scale of Fermi liquid coherence, the coherence temperature T_{coh}, is small. On the other hand, in many heavy fermion materials, the almost localized electrons originate from f-orbitals of rare-earth elements like Ce, where spin-orbit coupling is strong. Hence, for sufficiently large correlation effects, the width of the quasiparticle band can become smaller than the characteristic energy scale of spin-orbit coupling. In this case, spin-orbit coupling has a significant influence on the properties of the Fermi liquid state.

In particular, as was proposed by M. Dzero et al. in Refs. 30 and 31, in the case of Kondo insulators, the spin-orbit coupling can give rise to a topologically non-trivial band structure; that is, a topological Kondo insulator. Just like the conventional Kondo insulator, this state has to be adiabatically connected to a non-interacting band insulator. However, here the non-interacting state is a topological insulator. The authors hint at the possibility, that such a state might indeed be realized in Kondo insulating materials like SmB_6, YbB_{12} and $\mathrm{Ce}_3\mathrm{Bi}_4\mathrm{Pt}_3$.

The prospect of a topological Kondo insulator sounds promising, as it combines the complicated temperature dependence of heavy fermions with the intriguing properties of topological states of matter. As discussed in Sec. 2.2.2, the proposal sparked a number of experimental investigations on candidate materials for a topological Kondo insulator. In particular, expectations are high, that this new perspective can solve some of the open questions in the field of heavy fermion physics. The aim of Sec. 2.2.3 is to review some theoretical results for topological Kondo insulators. In Sec. 2.2.4, a simple model for topological Kondo insulators is devised, which takes spin-orbit coupling and interaction effects into account. After that the model is investigated with the help of DMFT+CTQMC, and sections 2.2.5 and 2.2.6 present different aspects of the numerical results. Finally, Sec. 2.2.7 summarizes the findings on topological Kondo insulators.

Part of the results presented here appeared in the publications J. Werner and F. F. Assaad, Phys. Rev. B **88**, 035113 (2013) and J. Werner and F. F. Assaad, Phys. Rev. B **89**, 245119 (2014).

2.2.2 Experimental Results

In this section the most important experimental results for topological Kondo insulators are summarized. The focus is on SmB_6, which is the most promising candidate material for the realization of such a state [29].

SmB_6 has been investigated extensively in the past [87]. Of particular importance is the fact, that SmB_6 is a mixed valence material. Hence, the material changes valence while the temperature is lowered into the Kondo insulating regime.

One of the unsolved mysteries is the temperature dependence of the resistivity, which does not fit the picture of a insulator. In particular, while exhibiting an exponential dependence in an intermediate temperature range, the resistivity saturates at the lowest temperatures [3].

In the following, only recent results concerned in one way or another with the topological character of the material are presented briefly. One of the challenges present in different investigations is to differentiate between experimental signatures originating from the surface and bulk effects [70, 74, 128].

The method of choice to reveal possible surface state is Angle Resolved Photoemission Spectroscopy (ARPES), which provides direct access to the occupied part of the momentum-resolved spectral density. The sensitivity to the surface can be tuned by the photon energy.

Following the proposal of topological Kondo insulators, the renewed interest in SmB_6 lead to a series of ARPES investigations [26]. Reaching the energy resolution necessary in order to detect surface states at low enough temperature proved to be a major barrier [32, 126]. Dispersive in-gap states were found [71], which appeared only at temperatures significantly lower than the characteristic temperature for the formation of the hybridization gap [126]. The surface states were robust against thermal recycling [74], favoring the interpretation of a topological origin. At the same time, a significant redistribution of spectral weight was observed during the gap formation, where conduction band states shift out of the gap. This signifies the importance of charge fluctuations in this mixed-valence compound [70].

Relating ARPES results with transport can provide additional, valuable insights. The temperature at which the conduction band crosses the Fermi level and the hybridization gap forms was found to coincide with a sign change of the Hall coefficient. In addition, the bulk conductivity and ARPES intensity at the Fermi level were found to vanish in a very similar fashion [27]. Besides these bulk properties, a mapping of the Fermi surface revealed an odd number of pockets around the high-symmetry points $\bar{X}$ and $\bar{\Gamma}$ of the surface Brillouin zone [54, 74].

A property of SmB_6, which complicates interpreting ARPES results, is that different surface terminations are possible. Hence, depending on the termination, trivial metallic surface states might arise, from B-2p dangling bonds [133].

Other experimental probes which were employed to study SmB_6 include Point Contact Spectroscopy (PCS) [128] and Scanning Tunneling Spectroscopy (STS) [92, 132], which can access local electron states, the latter with very high spatial resolution. In these works, the formation of the bulk gap and associated hybridizated bands is observed around the lattice coherence temperature. In addition, in Ref. 132 it was found that different surface morphologies to different spectral features. However a robust residual spectral weight at the Fermi level was found down to the lowest temperatures irrespective of the surface [92].

Quantum oscillation experiments relying on the de Haas-van Alphen effect, which is absent for an insulator, can provide valuable insights into the Fermi surface topology. In Ref. 67, two Fermi surface features were found. Both exhibit a small effective mass $m_{\text{eff}} \sim 0.1m$, consistent with a Dirac dispersion of the relevant states, and the chemical potential being located close to the crossing point. Plotting the highest occupied Landau level as a function of magnetic field and extrapolating to infinite field strength yields an intercept $\gamma = -1/2$, characteristic of a topological state.

Another hallmark of topological insulators is anomalous transport properties, which result from topological surface states. In particular, a local resistivity or conductivity as described by Ohm's law is not a valid notion in topological insulators. Experiments devised to distinguish bulk from surface conductance by using a special sample geometry found a crossover from three-dimensional to two-dimensional conductance at $T \approx 4$K [125]. Different scenarios of conventional, non-topological origin of the surface conductance were discussed, but found too fragile to explain the robustness of the effect. In particular, doping SmB_6 with non-magnetic Y and Yb impurity atoms cannot destroy the surface effect, as found by investigating the resistance ratio for different sample thicknesses [59]. However, doping with magnetic Gd impurities, hence destroying time-reversal symmetry, leads to a bulk-like result.

Hall effect measurements found a similar result, namely that at high temperature, the Hall resistance differs between different sample geometries, but converges to the same value at low temperatures [58]. Measurements at very low temperatures found a saturation of the resistance below $T = 4K$, leading to a plateau down to the lowest temperature $T = 20$mK. In addition, in a magnetic field oriented perpendicular to the surface, a dip in the magnetoresistance around zero field was observed, which is absent for in-plane orientation. This hints at weak antilocalization due to the locking of spin and momentum found in topological surface states [104]. In another work, a surface-roughness dependence of the conductivity was observed, which was interpreted in terms of a coexistence of trivial and non-trivial surface states [22].

2.2.3 Theoretical Results

In the presence of spin-orbit coupling, f-electron states are characterized by the total angular momentum J and the z-component m_J. In contrast, the conduction electron states, where the spin-orbit interaction is small, are characterized by spin σ. In order to determine the hybridization amplitude between f-electrons and conduction electrons, the f-orbital Wannier states have to be decomposed in terms of the plane-wave Bloch states. The different symmetries of the f-electron and conduction electron states lead to a non-diagonal structure of the hybridization amplitude in the hybridization part of the Hamiltonian [30]

$$\begin{aligned}\hat{\mathcal{H}}_{\text{hyb}} &= \sum_{i,j,\sigma,\alpha} V_{ij,\sigma\alpha}\hat{\text{c}}^{\dagger}_{i,\sigma}\hat{\text{f}}_{j,\alpha} + h.c. \\ V_{ij,\sigma\alpha} &= V\sum_{k}\Phi_{\sigma\alpha}(k)\exp\left(i\left(R_i - R_j\right)k\right),\end{aligned}$$

$\Phi_{\sigma\alpha}(k)$ is the momentum-dependent form factor, which is given by the overlap between the f-electron and conduction electron states, and is a general $(2J + 1) \times 2$ matrix.

The degenerate $(2J + 1)$-multiplet of the f-states is split in the presence of a crystal electric field (CEF), with the splitting depending on the particular crystal symmetry. For half-integer values of J, the presence of time-reversal symmetry guarantees, that the ground-state is at least a Kramer's doublet.

The angular momentum states for f-electron Kondo insulators are $J = 5/2$, which are the most relevant, and $J = 7/2$. In a cubic environment, the CEF splits the sixfold degenerate $J = 5/2$ multiplet into a doublet of Γ_7 symmetry and a Γ_8 quartet [9]. For a tetragonal lattice symmetry, the quartet is split, resulting in three doublets.

In Ref. 107 a detailed derivation of the form factor is given. The basic steps of the derivation and the result are reproduced here for later use. The hybridization amplitude $V_{ij,\sigma\alpha}$ is basically the overlap between a conduction electron state $|i\sigma\rangle$ at site i with spin orientation σ and an f-electron state $|j\alpha\rangle$ at site j in the state α of the multiplet of total angular momentum $J = 5/2$ split by the CEF.

$$V_{ij,\sigma\alpha} = \langle i\sigma | j\alpha\rangle \tag{2.2.1}$$

By successively decomposing the states in suitable basis states as described below, one obtains the expression

$$\langle i\sigma | j\alpha\rangle = \sum_{\eta,\sigma}\left(\langle i\sigma | j\eta\sigma\rangle \times \sum_{m_L=-3}^{3}\left(\langle j\eta\sigma | jm_L\sigma\rangle \times \sum_{m_J=-5/2}^{5/2}\langle jm_L\sigma | jm_J\rangle \times \langle jm_J | j\alpha\rangle\right)\right). \tag{2.2.2}$$

Here, since the system has cubic symmetry, $|j\eta\sigma\rangle$ is the basis of orbital angular momentum $L = 3$ cubic harmonics at site j, $|jm_L\sigma\rangle$ are $L = 3$ spherical harmonics, and $|jm_J\rangle$ are total angular momentum $J = 5/2$ states. The matrix elements $\langle i\sigma | j\eta\sigma\rangle$ are overlap integrals between s-orbitals and f-orbitals centered at different sites, which have been estimated in Ref. 103. The coefficients $\langle j\eta\sigma | jm_L\sigma\rangle$ decompose the spherical harmonics in terms of cubic harmonics, and $\langle jm_L\sigma | jm_J\rangle$ are Clebsch-Gordan coefficients. Finally, $\langle jm_J | j\alpha\rangle$ can be read of from the CEF multiplet in a cubic environment [9],

$$|\Gamma_{7,\pm}\rangle = \sqrt{1/6}\,|\pm 5/2\rangle - \sqrt{5/6}\,|\pm 3/2\rangle \tag{2.2.3}$$
$$|\Gamma_8\rangle = \begin{cases} |\Gamma_{8(1),\pm}\rangle = \sqrt{5/6}\,|\pm 5/2\rangle + \sqrt{1/6}\,|\pm 3/2\rangle \\ |\Gamma_{8(2),\pm}\rangle = |\pm 1/2\rangle \end{cases} .$$

Collecting all the coefficients, performing the internal summations in Eq. (2.2.2) and a Fourier transform, the form factor can be written using the vector of Pauli matrices $\sigma = (\sigma_x, \sigma_y, \sigma_z)$

$$\Phi(k) = d(k) \circ \sigma \tag{2.2.4}$$
$$\begin{aligned} \text{where} \quad d_{\Gamma 7}(k) &= 0 \\ d_{\Gamma 8(1)}(k) &= \big(2\sin(k_x), 2\sin(k_y), 0\big) \\ d_{\Gamma 8(2)}(k) &= \sqrt{1/3}\,\big(-2\sin(k_x), 2\sin(k_y), 4\sin(k_z)\big) . \end{aligned}$$

All additional prefactors are included in the definition of the hybridization amplitude V.

The simplest possible case of a topological Kondo insulator is obtained by taking only one of the Γ_8 doublets into account. This amounts to a single Kramer's doublet coupled to a single conduction band. This case was discussed in Ref. [30] on a cubic lattice on the level of an effective, mean-field Hamiltonian. The key parameter, which determines the state of the system, is the bare f-orbital energy ε_0. As Fig. 2.2.1 shows, depending on the position of ε_0, either a topological insulator (strong or weak) or a trivial insulator is realized, with metallic states at the transition points. In addition, for a system with open boundaries, the presence of a metallic surface state was shown by the direct calculation of the energy spectrum.

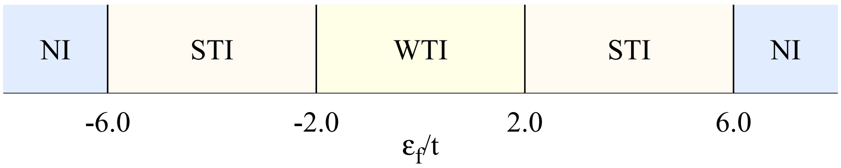

Figure 2.2.1: Different phases of a simple model for topological Kondo insulator in three dimensions. Depending on the position of the f-band ε_0 relative to the conduction band, a trivial insulator (NI), a strong topological insulator (STI) or a weak topological insulator may be realized. The black vertical lines denote the phase transition points, where the band gap closes. Adapted from Ref. 31.

In Ref. 107, a phase diagram for the same model was obtained within the slave-boson mean-field approach. For a fixed value of the f-orbital energy ε_0, with increasing hybridization strength V, a sequence of phase transitions between Mott insulator, strong and weak topological Kondo insulator and conventional Kondo insulator was found. In addition, interaction-driven quantum phase transitions between different topologically trivial and non-trivial phases were discussed [66].

While the approach of a single Kramer's doublet is appealing due to its simplicity, a treatment geared towards realistic topological Kondo insulating materials has to take into account the cubic symmetry usually found in these compounds. The full Γ_8 quartet of lowest lying f-states has to be included, which hybridizes with an e_g quartet of d-states. As discussed in Ref. 2 for three spatial dimensions within a slave-boson mean-field approximation, in this case, three Dirac cones at X/Y and M are possible. Being an odd number, this is a prerequisite for a non-trivial band topology. Compared to Fig. 2.2.1, the weak topological insulator is eliminated. Instead, the range of parameters leading to a strong TI is enlarged.

In Ref. 68 the candidate material SmB_6 was investigated within the LDA+Gutzwiller approach, which combines a first-principle band structure calculation with an approximate treatment of correlation effects. By calculating the parities in Eq. (1.2.10), the material was shown to be a topological insulator. Compared to the LDA results, the inclusion of correlations within the Gutzwiller variational ansatz shifts the $J = 7/2$ states up in energy, such that only $J = 5/2$ and 5d bands prevail around the Fermi level.

A similar study using LDA+Gutzwiller and LDA+DMFT of YbB_6 and YbB_12 found that the former is a topological insulator comparable to SmB_6, while the latter is a realization of a topological crystalline insulator [33] with a mirror Chern number of 2 [117].

However, the realistic modeling using a sophisticated many-body method like DMFT brings about a number of serious complications, in particular due to the Hund's rule exchange and the increased size of the local Hilbert space. Therefore, in the next section a simple model is introduced, which neglects material-specific aspects, but captures the fundamental and universal properties of topological insulators.

2.2.4 A Model for Topological Kondo Insulators

In the following, a simple model for topological Kondo insulators is devised. It is based on a single Kramer's doublet of f-states and a single conduction band. As a starting point, again the Periodic Anderson Model in two spatial dimensions is considered, now on a square lattice. Taking spin-orbit coupling into account, one can derive the following one-particle parameters of the Hamiltonian of Eq. (1.1.12)

$$\begin{aligned} \varepsilon_c(k) &= -2t_c\left(\cos(k_x) + \cos(k_y)\right) \\ \varepsilon_f(k) &= \varepsilon_0 - 2t_f\left(\cos(k_x) + \cos(k_y)\right) \\ V(k) &= V_{cf}\,\Phi(k) \end{aligned} \tag{2.2.5}$$

The form factor $\Phi(k)$ is constructed according to Eq. (2.2.4), where the f-state is assumed to have $\Gamma_{8(1)}$ symmetry. Therefore, the vector $d(k)$ takes the form

$$d(k) = \Big(d_x(k), d_y(k), d_z(k)\Big) = \Big(2\ \sin(k_x), 2\ \sin(k_y), 0\Big). \tag{2.2.6}$$

Inserting the parameters from Eq. (2.2.5) in the general expression of Eq. (1.1.15), the one-particle part of the Hamiltonian reads

$$\hat{\mathcal{H}}^{(0)}_{\text{TKI}} = \sum_k \begin{pmatrix} \hat{c}^\dagger_k & \hat{f}^\dagger_k \end{pmatrix} \begin{pmatrix} -2t_c(c_x + c_y) & 0 & 0 & 2V_{cf}(s_x - is_y) \\ 0 & -2t_c(c_x + c_y) & 2V_{cf}(s_x + is_y) & 0 \\ 0 & 2V_{cf}(s_x - is_y) & \varepsilon_0 - 2t_f(c_x + c_y) & 0 \\ 2V_{cf}(s_x + is_y) & 0 & 0 & \varepsilon_0 - 2t_f(c_x + c_y) \end{pmatrix} \begin{pmatrix} \hat{c}_k \\ \hat{f}_k \end{pmatrix}. \tag{2.2.7}$$

Here, the shorthand notation $c_i = \cos(k_i)$, $s_i = \sin(k_i)$ is used. As one can easily see, the Hamiltonian splits into two independent blocks, which are in fact Kramer's conjugate.

The model for the topological Kondo insulator as defined in Eq. (2.2.5) can be related to another prototypical model for topological insulators, the BHZ model, which was introduced in Sec. 1.2. By appropriately choosing model parameters, such that

$$t_f = -t_c,\ V_{cf}/t = \lambda, \text{ and } \varepsilon_0/t = -4m \tag{2.2.8}$$

the model of Eq. (2.2.5) can be transformed into Eq. (1.2.5). Even though the motivation of the BHZ model is different from the present situation, some of the results for this model certainly carry over, in particular in the weak coupling regime. However, in this work the main focus is on the strongly correlated regime.

For the current model, a Hubbard interaction on the f-orbitals is considered,

$$\begin{aligned} \hat{\mathcal{H}}_I =& U \sum_i \hat{n}_{f,\uparrow,i}\, \hat{n}_{f,\downarrow,i} \qquad (2.2.9) \\ \Rightarrow \hat{\mathcal{H}}_{\text{TKI}} =& \hat{\mathcal{H}}^{(0)}_{\text{TKI}} + \hat{\mathcal{H}}_I. \end{aligned}$$

To investigate the topological properties of the model, the topological invariant $\mathbb{Z}_2$ is calculated from the parity eigenvalues at the high-symmetry points Γ_i using Eq. (1.2.10). As the form factor Φ vanishes at the Γ_i, following Ref. 30, the one-particle part of the Hamiltonian can be written as

$$h(\Gamma_i) = \frac{E_i}{2} + \frac{\delta_i}{2} P \tag{2.2.10}$$

$$\text{where} \quad P = \text{diag}(+1,\ +1,\ -1,\ -1). \tag{2.2.11}$$

Hence, one obtains the following expression for the $\mathbb{Z}_2$ topological invariant ν

$$(-1)^\nu = \underbrace{\text{sign}(4t_f - 4t_c - \varepsilon_0)}_{\delta_\Gamma}\ \underbrace{\text{sign}(4t_c - 4t_f - \varepsilon_0)}_{\delta_M}\ \underbrace{\text{sign}(-\varepsilon_0)}_{\delta_X}\ \underbrace{\text{sign}(-\varepsilon_0)}_{\delta_Y}. \tag{2.2.12}$$

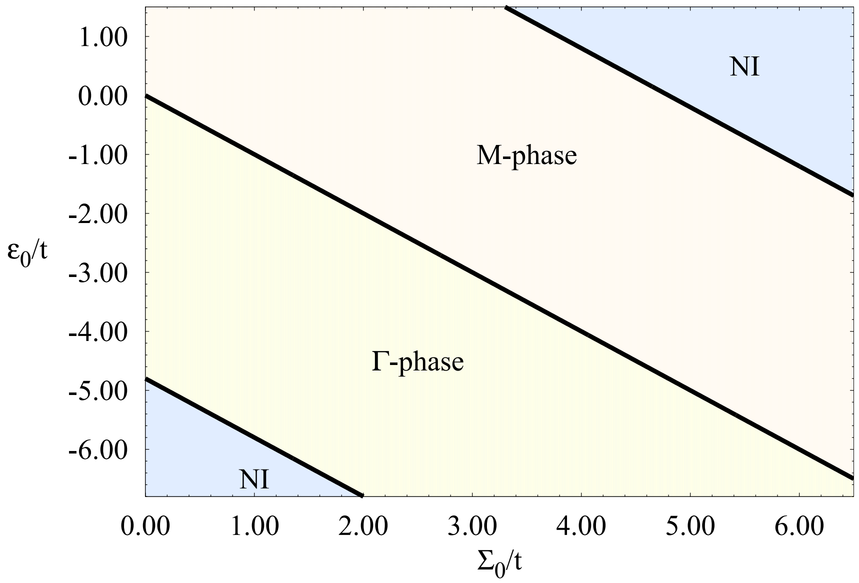

Figure 2.2.2: Phase diagram of the topological Hamiltonian in two dimensions, as a function of the bare f-level position ε_0 and the renormalization constant Σ_0, which results from the interaction. Depending on the choice of parameters, a trivial normal insulator (NI) as well as the non-trivial Γ-phase and M-phase may be realized. At $\Sigma_0 = 0$ it contains the non-interacting case as well. At the black transition lines the argument of at least one sign function in Eq. (2.2.13) is zero.

The different topological and non-topological phases arising in the model, which are contained in the above expression, are discussed in the next section in the context of a DMFT investigation of the full, interacting model for topological Kondo insulators.

In the DMFT, the topological Hamiltonian is simplified according to Eq. (1.3.9). Hence, the only difference arising due to correlations in Eq. (2.2.12) is that one has to replace $\varepsilon_0 \to \varepsilon_0 + \Sigma_0$, so that

$$(-1)^{\nu} = \operatorname{sign}(4t_f - 4t_c - \varepsilon_0 - \Sigma_0)\ \operatorname{sign}(4t_c - 4t_f - \varepsilon_0 - \Sigma_0)\ \operatorname{sign}(-\varepsilon_0 - \Sigma_0)^2. \tag{2.2.13}$$

During this work, the c-hopping amplitude t_c is chosen as the energy unit, i. e. $t_c = t = 1$, while the f-hopping amplitude and hybridization are chosen as $t_f = -0.2t$ and $V_{cf} = 0.4t$. The bare f-orbital energy ε_0 is varied.

For this situation, using the result from Eq. (2.2.13), one is able to calculate the topological ground state phase diagram of the current model in terms of the f-level position ε_0 and the renormalization constant Σ_0. It is shown in Fig. 2.2.2.

As already expected from the discussion in Sec. 1.2.3.2 about the space-group classification of topological states, three distinct phases are realized: A conventional band insulator with parities $(+1,+1,+1,+1)$, as well as two topological phases, the Γ-phase with $(-1,+1,+1,+1)$ and the M-phase with $(-1,+1,-1,-1) \equiv (+1,-1,+1,+1)$. In principle, an additional phase, the X-Y-phase is possible, which is a so-called topological crystalline insulator [33]. The corresponding parities are $(+1,+1,-1,-1)$, which yields a topological invariant $\nu = 0$. However, it can only be realized by including hopping processes between next-nearest neighbors [99].

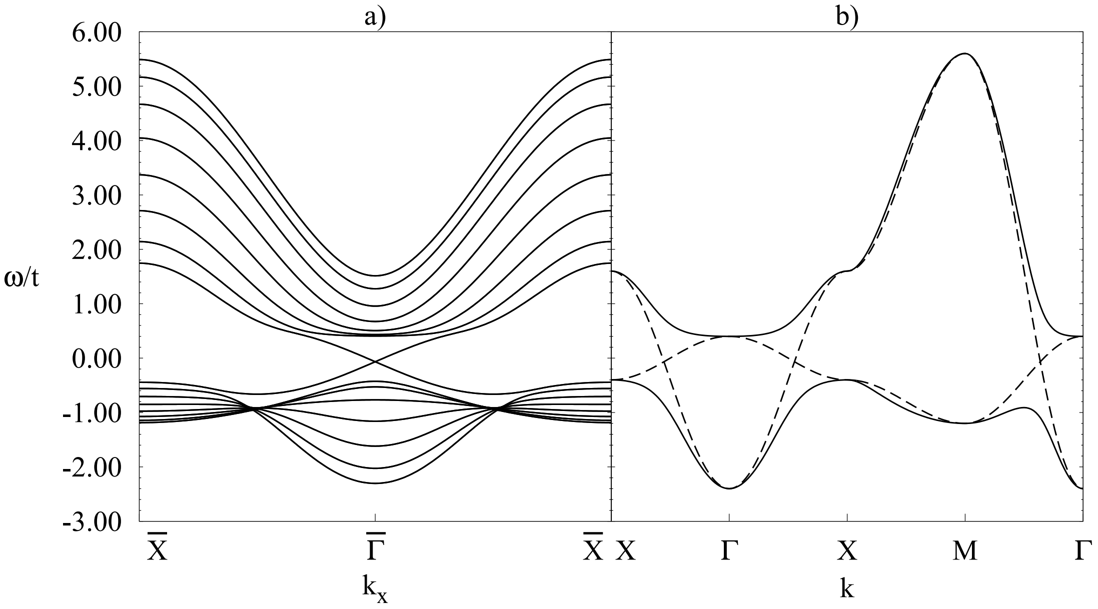

Figure 2.2.3: Energy spectrum a) for open boundaries, with $N_y = 16$, and b) for periodic boundaries, as a function of momentum in the surface and bulk Brillouin zone. The dashed lines correspond to the case with no hybridization ($V_{cf} = 0$).

In Fig. 2.2.3 the energy spectrum of the non-interacting Hamiltonian (2.2.5) is shown for $\varepsilon_0/t = -2.0$. This point in parameter space is located in the Γ-phase, since calculating the parity eigenvalues δ_i yields

$$\begin{aligned}(\delta_\Gamma, \delta_M, \delta_X, \delta_Y) &= (-1,+1,+1,+1)\\ \Rightarrow \nu &= +1\end{aligned}$$

The topological character of the state becomes apparent in the left panel with open boundary conditions, where topological surface states crossing at $\bar{\Gamma}$ can be seen. Comparing in the right panel the cases with hybridization (solid lines) and without hybridization (dashed lines) reveals the band inversion between Γ with parity -1 and X/Y and M, which have parity $+1$, as well as the vanishing of the form factor $\Phi(k)$ at all of these high-symmetry points. Hence, the system has a non-trivial band topology, and by placing the chemical potential inside the bulk band gap, i. e. the insulating case, a topological insulator is realized.

2.2.5 Topological Phase Transitions

In the previous discussion it became clear that the character of the phase, topological or not, depends on the model's bare parameters as well as on the renormalization due to correlations. The second point brings about the possibility of driving the system through phase transitions by changing the interaction strength.

Here, results of DMFT studies of the model introduced above are presented. The auxiliary impurity problem of the DMFT is solved by means of the CT-HYB method, which allows to study the model from U = 0 up to very high interaction strength, and at sufficiently low temperatures to gain insight into the ground state.

To proceed, different non-interacting starting points are chosen, namely i) $\varepsilon_0/t = -2.0$ (Γ-phase) as well as ii) $\varepsilon_0/t = 1.0$ (M-phase) and iii) $\varepsilon_0/t = -6.0$ (NI). In each case, the chemical potential μ is located inside the bulk band gap, such that the system is half-filled, with one filled band below μ and another empty band above μ, and is hence an insulator.

First, the evolution of the bulk band gap Δ_g is studied. While U is adiabatically increased, the chemical potential μ is adapted in order to stay in the middle of the band gap. The band gap size is determined by $\Delta_g = \Delta_{lu} - \Delta_{ho}$, where Δ_{lu} (Δ_{ho}) is the energy difference from the lowest unoccupied (highest occupied) state to the chemical potential. The energy differences can be obtained from the decay of the local imaginary time Green's function by fitting appropriate exponentials in the range $\tau < \beta/2$ and $\tau > \beta/2$:

$$G_{\text{loc}}(\tau) \sim \begin{cases} e^{-\Delta_{ho}\,\tau}, & \tau < \beta/2 \\ e^{-\Delta_{lu}\,(\beta-\tau)}, & \tau > \beta/2 \end{cases} \tag{2.2.14}$$

$$\text{where} \quad G_{\text{loc}}(\tau) = \frac{1}{N}\sum_k G(k,\tau).$$

This is exemplified in Fig. 2.2.4a. In order to get a robust estimate for the band gap, the temperature has to be $T \ll \Delta_g$. For $T \geq \Delta_g$, the exponential decay cannot be resolved due to thermal broadening.

The result for the band gap size of case i) is shown in Fig. 2.2.4b. As mentioned in the beginning, the non-interacting starting point is located in the Γ-phase. With increasing of the interaction strength U, the gap size starts to decrease. Approaching $U/t = 4.0$, the gap size becomes so small that eventually the temperature necessary to reliably determine Δ_g cannot be reached. However, as can be seen in Fig. 2.2.4a, at $U/t = 4.0$ there is clearly no exponential dependence on τ around $\beta/2$, even at the very high inverse temperature $\beta/t = 300$. Instead, the

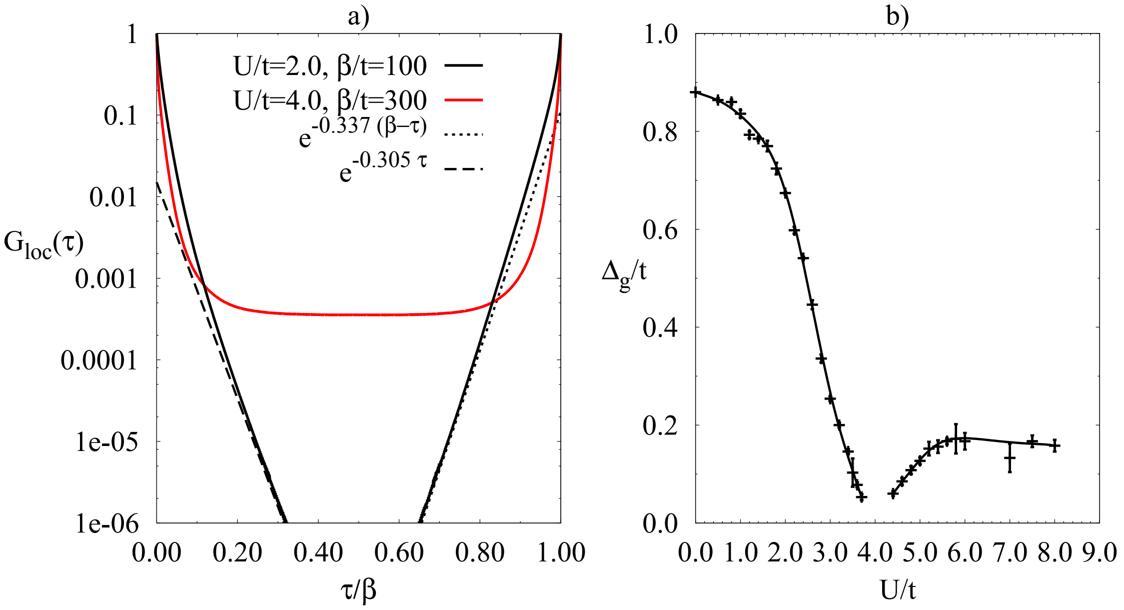

Figure 2.2.4: a) local Green's function for case i) ($\varepsilon_0/t = -2.0$) at different U and β. For $U/t = 2.0$ the decay of the Green's function around $\tau = \beta/2$ is fitted by exponentials shown with dashed and dotted lines. For $U/t = 4.0$, there is a plateau around $\tau = \beta/2$, which indicates the presence of spectral weight at the Fermi level; that is, a closing of the band gap. b) Size of the bulk band gap as a function of interaction strength U/t. The solid line is a guide to the eye.

plateau around $\beta/2$ is a clear signature of finite spectral weight located right at the chemical potential. Further increasing U, the gap size starts to increase again. From these observations it becomes clear that in fact the band gap closes at $U/t \approx 4.0$.

In order to better understand what happens at $U/t = 4.0$, one has to turn to the phase diagram of Fig. 2.2.2. For this, the renormalization constant Σ_0 has to be obtained from extrapolation of the self-energy to zero frequency. This quantity is shown in Fig. 2.2.5a. While the imaginary part vanishes linearly, the real part extrapolates to a constant as $\omega_n \to 0$. In Fig. 2.2.5b the results for Σ_0 and the effective mass, i. e. the slope of the imaginary part, are plotted. By looking specifically for the point $U/t = 4.0$, one sees that here the value of Σ_0 is precisely at the transition line between the Γ-phase and M-phase, which is located at $\Sigma_0/t = 2.0$. In conclusion, a quantum phase transition induced by the interactions is found, where the system is driven from the non-interacting starting point of the Γ-phase via a band gap closing into the M-phase.

In the following, it is shown that the system is indeed in the M-phase for interactions $U/t > 4.0$. To this end, the adiabatical connection to the non-interacting M-phase has to

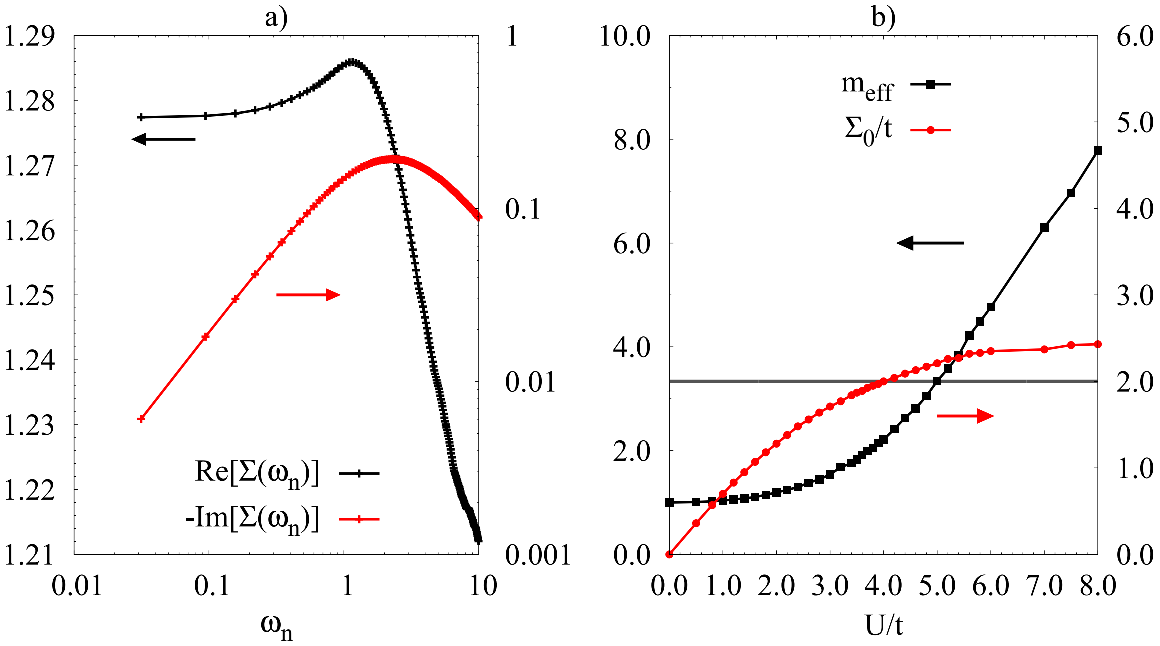

Figure 2.2.5: a) Real and imaginary part of the local self-energy for case i) ($\varepsilon_0/t = -2.0$) at $U/t = 2.0$ and $\beta t = 100$. b) Effective mass and renormalization constant Σ_0 for case i). The solid lines are guides to the eye. The gray horizontal line at $\Sigma_0/t = +2.0$ indicates the transition line predicted from Eq. (2.2.13).

be established. To do so, the case ii) is considered. To adiabatically connect it to the case i) at $U/t > 4.0$, U has to be increased slowly. At the same time the bare f-level has to be shifted from the initial value $\varepsilon_0/t = 1.0$ to $\varepsilon_0/t = -2.0$, while keeping track of the band gap size. That this approach does indeed work out can be seen in Fig. 2.2.6. Along the path starting at $\varepsilon_0/t = +1.0$, the band gap never closes. Meanwhile, the closing of the gap at $(\varepsilon_0/t = -2.0, \Sigma_0/t = +2.0)$ is the transition point discussed above. Both paths meet at around $(-2.0, +2.3)$. Thus, the adiabatical connection from case i) at $U/t > 4.0$, which corresponds to $\Sigma_0/t > 2.0$, to the non-interacting M-phase is established. Hence, this proves that by tuning the interaction, the system can be driven through a phase transition between distinct topological phases, namely from the Γ-phase to the M-phase.

2.2.6 Topological Heavy Fermion Phase

2.2.6.1 Bulk Topological Kondo insulator

In this section, the focus is put on case iii) ($\varepsilon_0/t = -6.0$), which has not yet been discussed. Here, the non-interacting starting point is located in the trivial phase (NI). By increasing the

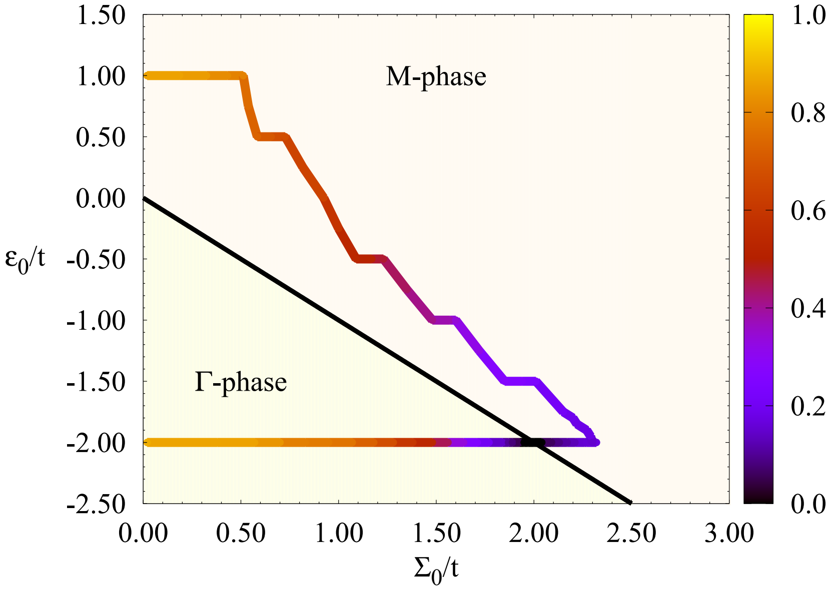

Figure 2.2.6: Part of the phase diagram of Fig. 2.2.2, superimposed with the size of the band gap color-coded along the paths in parameter space which correspond to the cases i) and iii).

interaction strength U, a band gap closing at $U/t \approx 1.2$ is found, as Fig. 2.2.7a shows. At the same time, the renormalization constant Σ_0 crosses the transition line from the NI-phase to the Γ-phase, which can be seen in Fig. 2.2.7b. By the reasoning already applied above, it is concluded that in case iii) it is possible to drive a transition from the NI-phase to Γ-phase by changing the interaction. While it is not proven here, there is no doubt that an adiabatical connection to the non-interacting Γ-phase is possible.

Beyond the transition, the band gap starts to grow up to $U/t \approx 3.0$, where it again decreases in size. For $U/t > 8.0$ it becomes very small. At the same time, the renormalization constant Σ_0, while approaching the value of the transition to the M-phase, seems to saturate at a somewhat smaller value. In contrast, the effective mass starts to grow quickly, and for $U/t = 8.0$ takes on very large values. In fact, it seems to diverge on approaching $U/t = 9.0$. This could in principle be understood in the framework of a Mott transition. However, within the DMFT approximation, it is more reasonable to assume that the effective mass does not diverge, hence the coherence temperature does not vanish: It just takes a very small values. Thus, the ground state is still a Fermi liquid. A more thoroughly founded answer about the nature of the state for $U/t \geq 9.0$ can only be found by using methods that go beyond the DMFT.

Therefore, no definitive statements is made here on the nature of phase transition. However, in order to shed some light on this issue, the range of parameters in the vicinity of the apparent

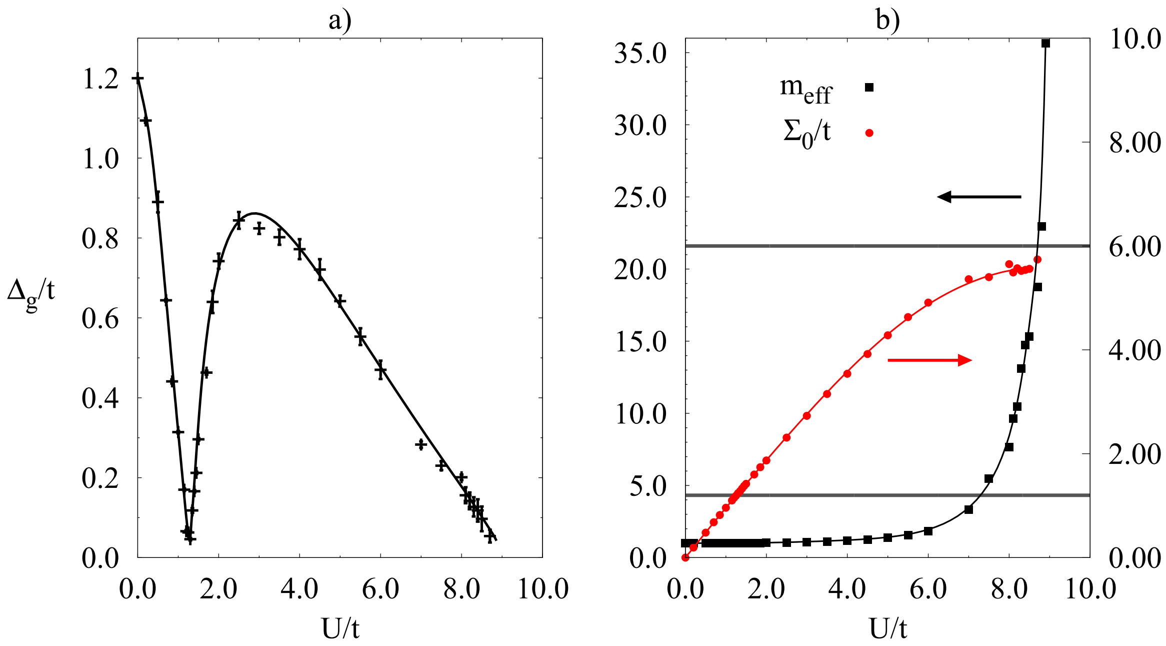

Figure 2.2.7: Evolution as a function of interaction strength U for case iii) ($\varepsilon_0/t = -6.0$) of a) bulk gap size and, b) effective mass and renormalization constant. The solid lines are guides to the eye. The gray lines at $\Sigma_0/t = 1.2$ and $\Sigma_0/t = 6.0$ mark the transitions from NI-phase to Γ-phase and from Γ-phase to M-phase, respectively.

divergence is studied in more detail below. Here, the effective mass is large, but clearly finite.

The phase diagram of Fig. 2.2.8 summarizes the results for the bulk of the topological Kondo insulators. It shows the different phases predicted by the topological Hamiltonian, and the numerically found band gap size. Most of the predicted phase transitions can indeed be identified in our simulation results, indicated by the band gap closing coinciding with the transition lines between distinct phases. The shaded region indicates the possible Mott phase.

To find out more about the region close to the apparent phase transition, the possibility of local moment formation in the f-orbitals at high temperatures is investigated, which is a prerequisite for the coherent heavy fermion state at low temperatures.

To this end, the quantity

$$\Theta = 1 - \frac{\langle \hat{n}_{f,\uparrow}\hat{n}_{f,\downarrow}\rangle}{\langle \hat{n}_{f,\uparrow}\rangle\langle \hat{n}_{f,\downarrow}\rangle} \tag{2.2.15}$$

is studied. Here, $\langle \hat{n}_{f,\sigma}\rangle$ is the occupation of the f-orbital with spin σ, and $\langle \hat{n}_{f,\uparrow}\hat{n}_{f,\downarrow}\rangle$ is the double occupancy. In the non-interacting limit $\Theta = 0$, while a perfect local moment yields $\Theta = 1$, because the double occupancy is completely suppressed. In Fig. 2.2.9a, the quantity Θ is plotted as function of U. It grows slowly, such that at the transition from the normal

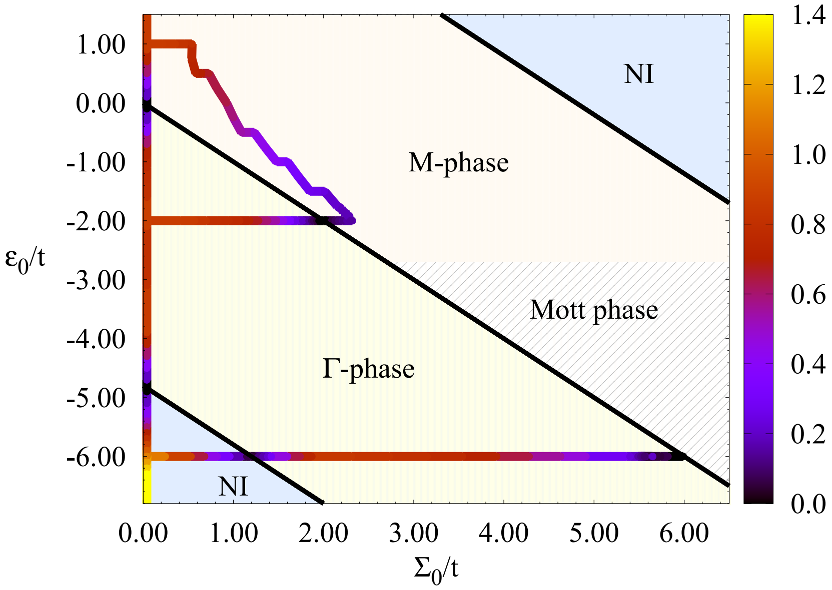

Figure 2.2.8: Complete phase diagram of the model for the topological Kondo insulators. The numerically found band gap size is included in the same fashion as in Fig. 2.2.6, for the cases i) to iii).

insulator to the Γ-phase at $U/t \approx 1.2$, there are almost no correlation effects visible. Hence, this transition can be understood equally in a mean-field decoupling of the interaction Hamiltonian $\hat{\mathcal{H}}_I$ [111]. With increasing U and decreasing filling of the f-orbitals, correlation effects become more pronounced. In particular, as the f-orbital occupancy $n_f = n_{f,\uparrow} + n_{f,\downarrow}$ approaches half-filling, Θ is getting closer to 1.

In Fig. 2.2.9b, the evolution of Θ is tracked as the temperature changes. Starting at very high temperatures, where correlations play hardly any role, Θ increases, and reaches a maximal value before decreasing at lower temperature and finally saturating as $T \to 0$. From this behavior, one can define a temperature scale T_L as

$$\Theta(T_L) = 1/2, \qquad (2.2.16)$$

which tracks the onset of local moment formation. In this way, it is possible to define T_L for parameters $U/t \geq 7.0$.

Hence, the ingredients for a heavy fermion state are complete: The f-orbital local moments formed below T_L hybridize with delocalized conduction electrons, thereby creating composite quasiparticles as the temperature becomes lower than the coherence scale $T_{\text{coh}} \ll T_L$.

As was already visible in Fig. 2.2.7b, in the vicinity of the putative Mott transition, the effective quasiparticle mass can take quite large values. This results from a large renormaliza-

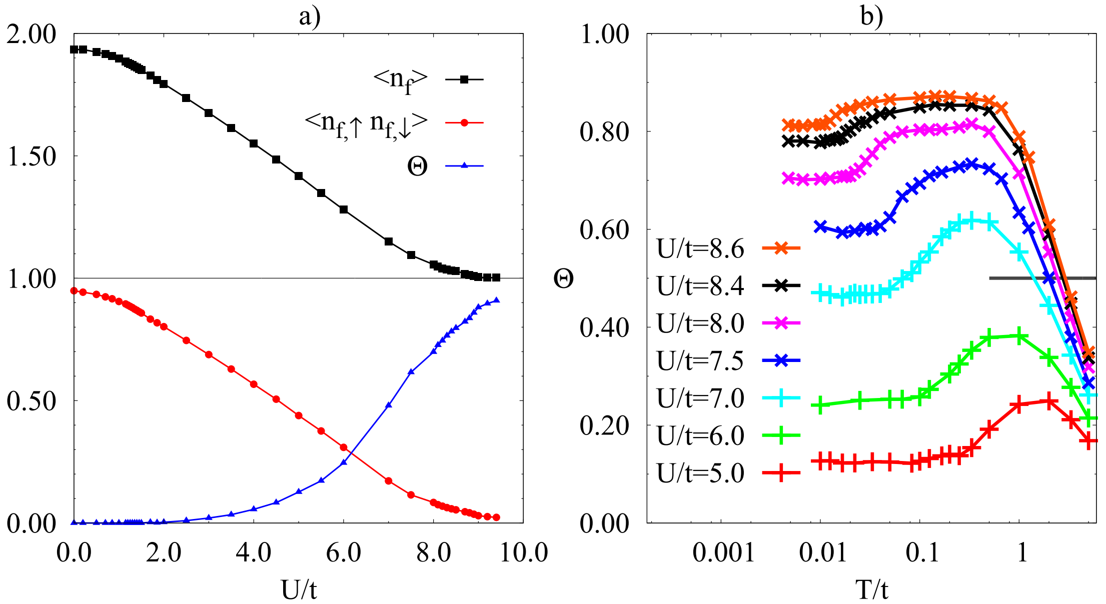

Figure 2.2.9: a) f-orbital occupancy, double occupancy and Θ defined in Eq. (2.2.15) for the case iii) ($\varepsilon_0/t = -6.0$), as a function of interaction strength U, at the lowest temperatures. b) Evolution of Θ with temperature for a range of values of U. The solid gray line indicates the threshold value for defining T_L in Eq. (2.2.16).

tion of the bands due to correlations, which becomes visible quite convincingly in the spectral function. This quantity is shown in Fig. 2.2.10. The left panel corresponds to the weakly correlated system close to the transition from NI-phase to Γ-phase: The bulk band gap is almost closed at Γ, where the band inversion takes place. The other panels correspond to the Γ-phase. For moderate correlations ($U/t = 5.0$), the bands are becoming increasingly flat around the band gap. However, the upper Hubbard band is located close to the chemical potential, so that charge fluctuations still play a significant role. In the strongly correlated case ($U/t = 8.4$), the renormalization leads to very flat heavy fermion bands. Hence, the band gap is very small, in particular around X/Y. There the band gap has to close and reopen in order to perform the transition to the M-phase. As was discussed in the previous section, it is not clear whether this phase transition takes place at all. At least, since T_{coh} is rather small in the heavy fermion regime, one cannot rule out the possibility that it is superseded by a magnetic scale J.

In the heavy fermion regime, the lower and upper Hubbard band are already well formed, containing a significant portion of spectral weight, with only little spectral weight $\sim Z$ left in the quasiparticle bands. However, even with the large renormalization of the bulk bands and band gap, and the small quasiparticle fraction Z, the state is still adiabatically connected to the non-interacting state. What is exciting here is that this non-interacting state is not a

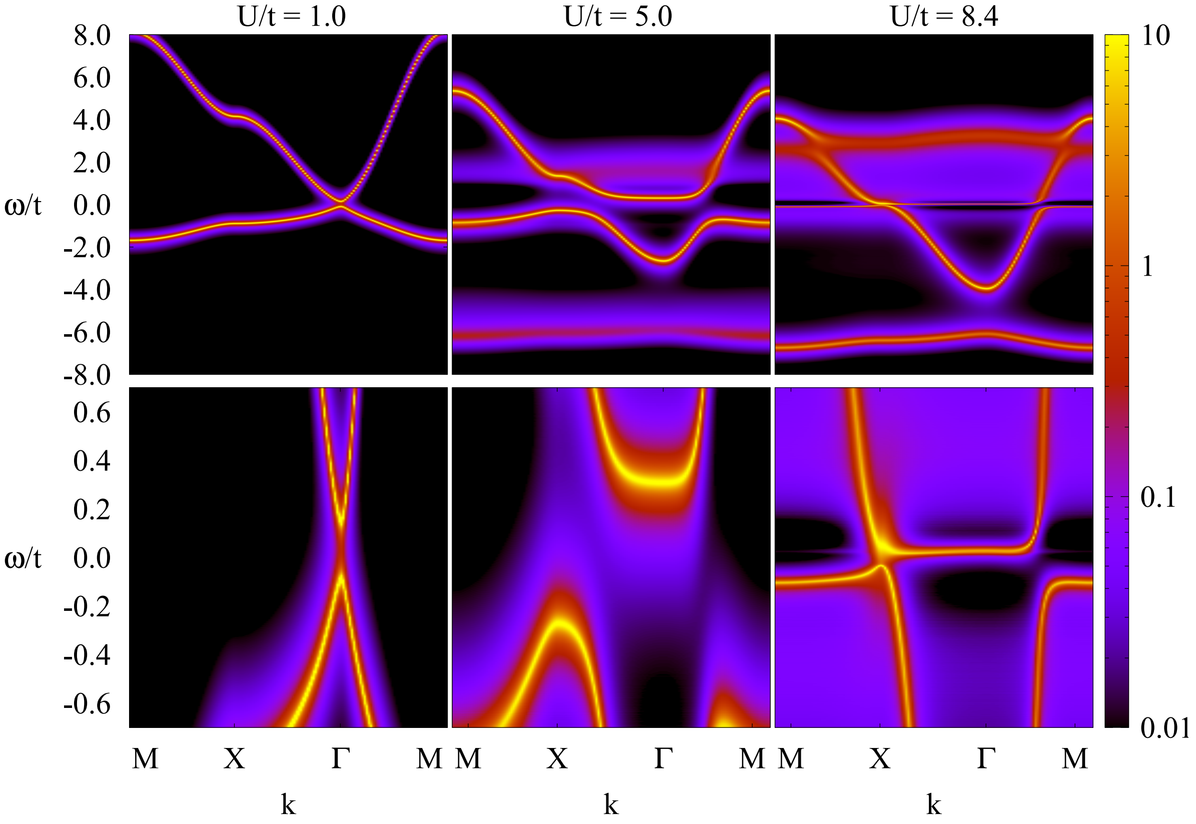

Figure 2.2.10: Spectral function for case iii) ($\varepsilon_0/t = -6.0$) for different values of U at the lowest temperatures. The second row of plots shows the frequency range around $\omega = 0$ in more detail.

conventional band insulator, but rather a topological insulator. Since the topological character of the state is preserved, in the presence of interactions and at half filling the system is hence in a topological heavy fermion state; that is, a topological Kondo insulator.

As discussed in Sec. 2.2.6.3, due to its topological nature, this state gives rise to topological edge states inside the gap between the heavy bulk bands.

2.2.6.2 Temperature Dependence of Topological Properties

In this part, the relation between the heavy fermion state and topological properties of bulk topological Kondo insulators are investigated in more detail. Of particular interest is be the temperature dependence of spectral and topological properties. The above model is be studied with periodic boundary conditions here, and with open boundary conditions in Sec. 2.2.6.3. The interaction strength U is chosen in the range from $U/t = 5.0$ to $U/t = 8.4$.

To this end, the quantity N_s defined in Eq. (1.3.10) is considered. It is plotted in Fig. 2.2.11a

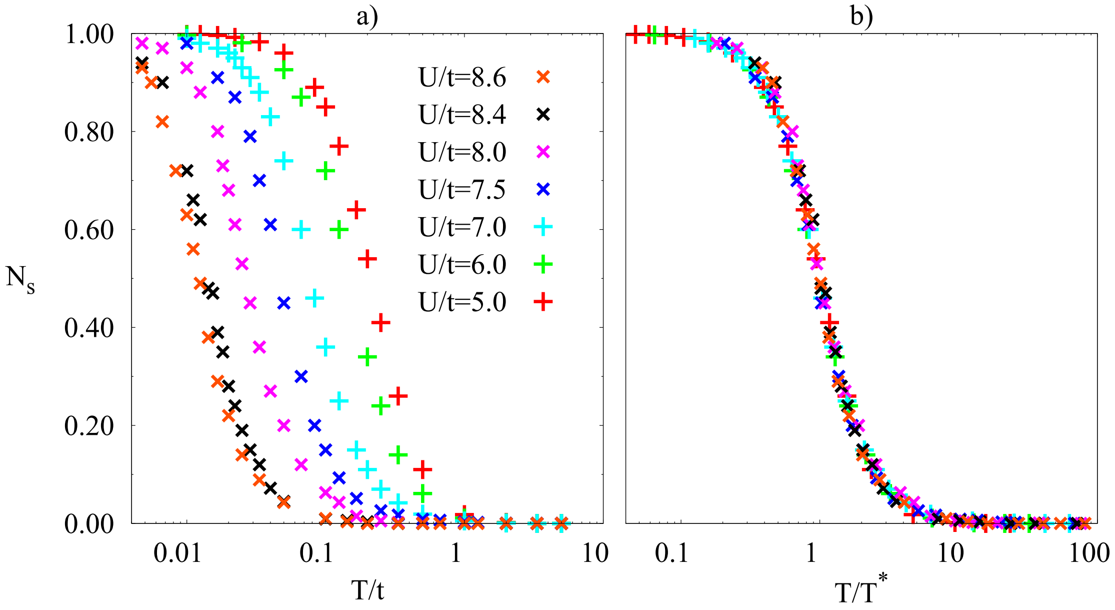

Figure 2.2.11: N_s topological invariant for case iii) ($\varepsilon_0/t = -6.0$), for different interaction strength U, a) as a function of temperature, b) with the temperature rescaled by T^*.

as a function of temperature for a range of interactions U.

From the data, one can define a temperature scale T^* for the emergence of the topological state in the bulk via

$$N_s(T^*) = 1/2. \tag{2.2.17}$$

Rescaling the temperature with respect to T^*, as is done in Fig. 2.2.11b, yields a very nice data collapse. This hints at the possibility that the emergence of the topological band structure with lowering of the temperature is governed by a single scale.

The temperature scale in question might well be the quasiparticle coherence scale T_{coh} of the heavy fermion state. Starting at $T = 0$, with increasing temperature, the topological state is expected to disappear at a temperature $T \sim \Delta_g$; that is, the bulk band gap. At higher temperatures, the system becomes metallic, because electrons can be thermally excited to unoccupied states. However, since the band gap $\Delta_g \sim T_{\text{coh}}$, the coherence temperature should equally be the temperature scale relevant for the emergence of the topological state.

That this is indeed the case can be seen by comparing T^* with the inverse effective mass, ${m_{\text{eff}}}^{-1} \sim T_{\text{coh}}$ in Fig. 2.2.12. Here, the different energy scales, which can be extracted from the simulation results, are shown. It becomes apparent that the two scales T^* and T_{coh} are the same up to a constant prefactor.

This observation signifies, that T^* can be employed as a measure for the Fermi liquid co-

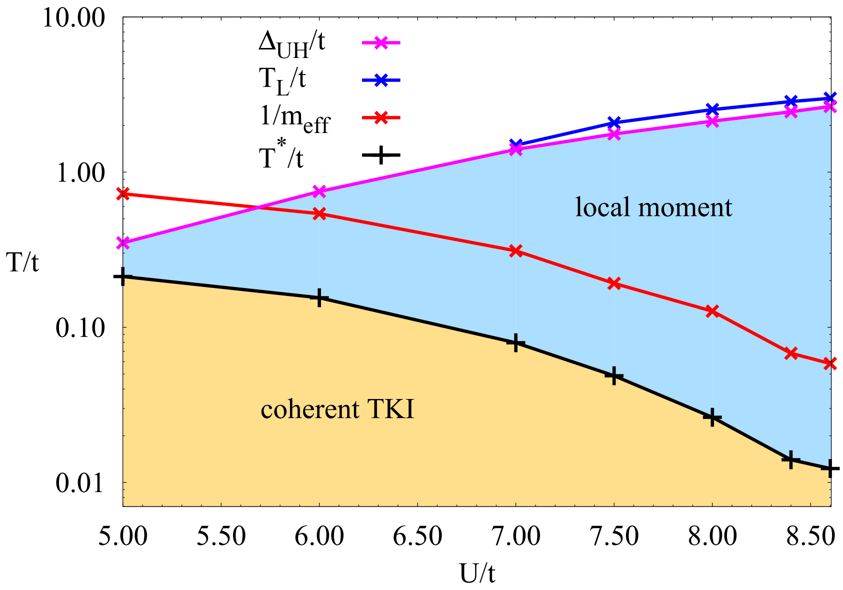

Figure 2.2.12: Comparison of different energy scales of the topological Kondo insulator.

herence scale, which is the only low energy scale. Thus, the topological property N_s turns out to be an independent and convenient measure of coherence.

Meanwhile, by comparing the local moment scale T_L with the energy difference between the upper Hubbard band and the chemical potential,

$$\Delta_{\mathrm{UH}} = \varepsilon_0 + U - \mu \tag{2.2.18}$$

it becomes evident that both scales are very similar. Hence, the local moment formation can be equally captured by Δ_{UH}. This seems plausible, since Δ_{UH} is more or less the energy necessary to excite charge fluctuations.

Thus, Fig. 2.2.12 summarizes the main findings about the bulk topological Kondo insulator. It combines the different energy scales inherent to the model of topological Kondo insulators to a complete temperature phase diagram.

The local moment scale and coherence scale are well separated at large U. Hence, the temperature range of the local moment regime can be nicely distinguished from the coherent Fermi liquid state. As U becomes smaller, both scales become comparable. While the ground state is still a Fermi liquid, charge fluctuations play a significant role, and prohibit the formation of local moments. The magnitude of charge fluctuations is related to the coherence scale. As the coherent quasiparticles are established, spectral weight is shifted from the chemical potential towards the quasiparticle bands. This shift can be assessed from the evolution of the density of states with temperature, which is shown in Fig. 2.2.13. For $U/t = 5.0$ the large

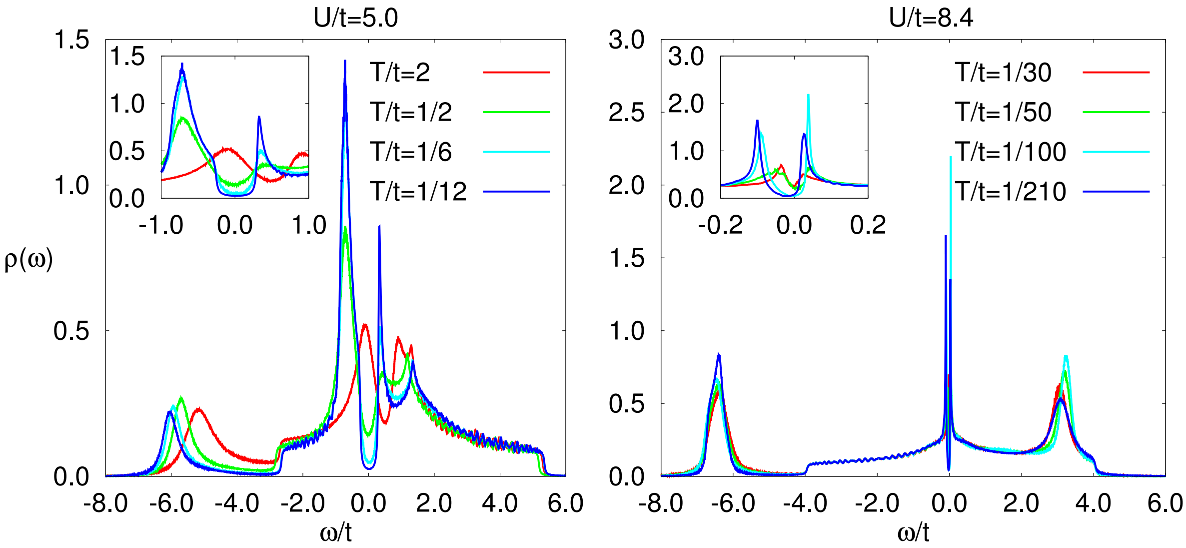

Figure 2.2.13: Bulk density-of-states as a function of temperature for $U/t = 5.0$ ($T^*/t \approx 0.21$) and $U/t = 8.4$ ($T^*/t \approx 0.014$).

value of T_{coh} is mirrored by a large transfer of spectral weight, which takes place during the formation of the hybridization gap. Here, charge fluctuations cannot be neglected due to the upper Hubbard band being located very close to the chemical potential.

In contrast, the spectral weight transfer for $U/t = 8.4$ is very small, owing to the strong renormalization; that is, a small coherence scale $T_{\text{coh}} \ll T_L$. Hence, charge fluctuations are frozen out for $T < T_L$. In this case, the separation of the two energy scales is clearly visible, as the upper Hubbard band is far away from the chemical potential, while the quasiparticle peaks are close to the chemical potential and very narrow.

2.2.6.3 Topological Surface States

In this section, the emergence of the topological surface states and its relation to the onset of coherence in the bulk is investigated. To this end, results for case iii) with open boundary conditions are present, which are obtained using the site-dependent DMFT. In x-direction, the system is periodic, while it has open boundaries in the y-direction. Therefore, k_x is a good quantum number, while this is not the case for k_y. The number of sites in y-direction is chosen in the range from $N_y = 8$ to $N_y = 24$, and is given in each figure.

To make the appearance of the topological surface states visible, total spectral function is considered.

$$A_{\text{tot}}(k_x, \omega) = \frac{1}{N_y} \sum_{i=1}^{N_y} \sum_{\alpha=c,f} \left[A_{\alpha,i}(k_x, \omega) \right] \tag{2.2.19}$$

This quantity is obtained from analytical continuation of the layer-dependent self-energy. In Fig. 2.2.14, $A_{\mathrm{tot}}(k, \omega)$ is plotted for $U/t = 5.0$. The same quantity is shown in Fig. 2.2.15 for $U/t = 8.4$. The different values of U correspond to different positions in the phase diagram.

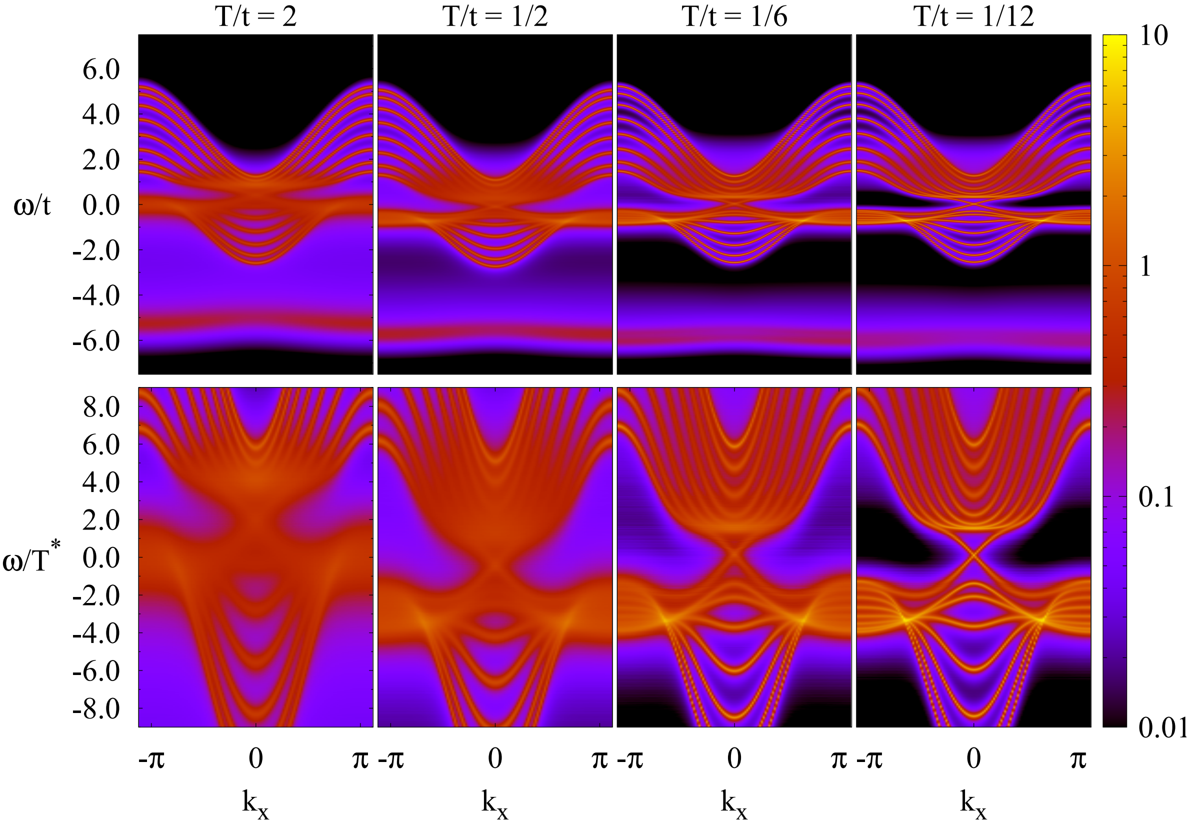

Figure 2.2.14: Spectral density as a function of temperature for $U/t = 5.0$, where $N_y = 8$, and $T^*/t \approx 0.21$.

For the smaller value, $U/t = 5.0$, the system is in the mixed valence regime, wile $U/t = 8.4$ is in the local moment regime. The results are shown for a series of temperatures ranging from well above to far below the bulk coherence scale, which is given in the caption.

Moving from high to low temperatures, one sees a considerable sharpening of features, in particular in the vicinity of the chemical potential. While at first the surface states with the crossing point at $k_x = 0$ are completely washed out, they become more easily visible as the temperature crosses the coherence scale.

In the mixed valence regime at $U/t = 5.0$, the importance of charge fluctuations becomes apparent in the shift of the whole band structure as the temperature is lowered from $T/t = 2$ to $T/t = 1/2$.

For $U/t = 8.4$ the emergence of the topological surface states happens in the same way, only at much lower temperatures. This is due to the smaller value of the coherence scale. Hence, the surface states equally appear at temperatures $T \approx T_{\text{coh}}$. A shift of the band structure due to charge fluctuations is almost completely absent in this temperature range as the energy scales are well separated, i. e. $T_L \gg T_{\text{coh}}$.

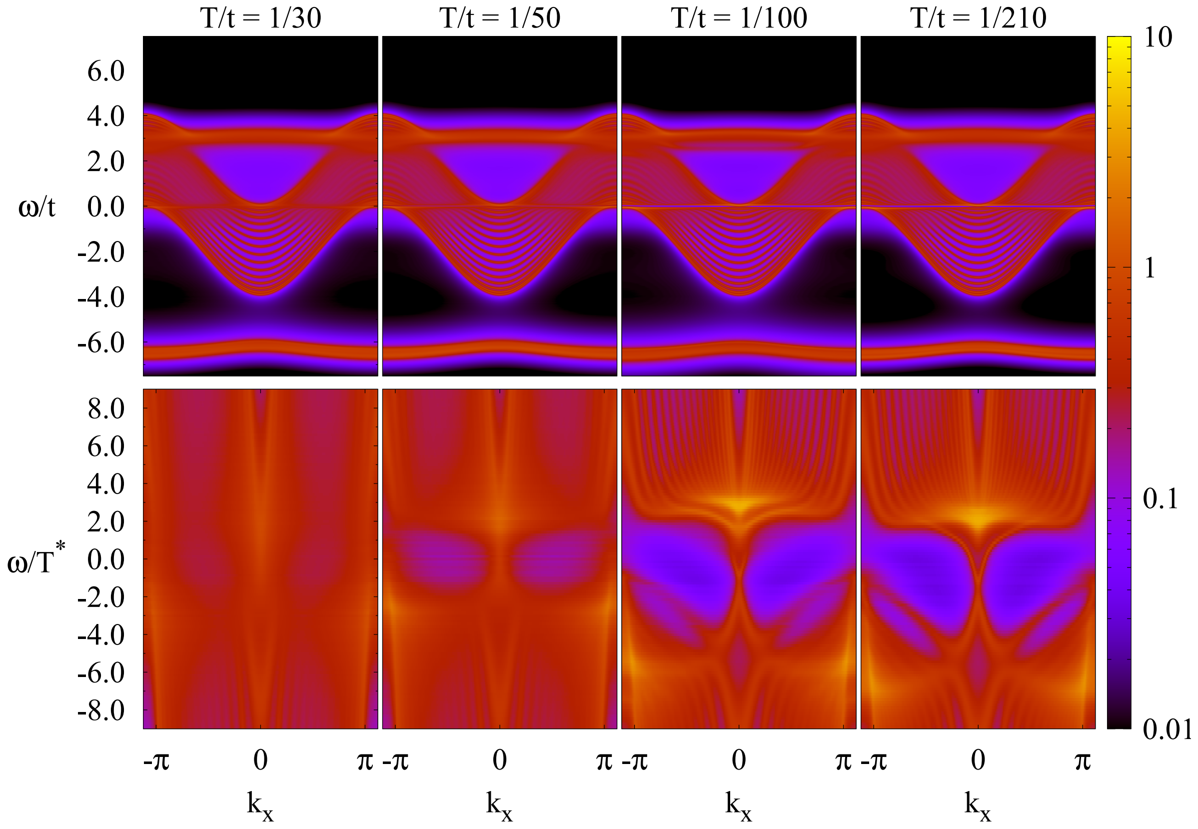

Figure 2.2.15: Spectral density as a function of temperature for $U/t = 8.4$, where $N_y = 16$, and $T^*/t \approx 0.014$.

In the case of $U/t = 8.4$, the width of the ribbon is increased to $N_y = 16$. This is necessary due to the penetration depth ξ of the surface states, which correlates with the inverse coherence scale $\xi \sim T_{\text{coh}}{}^{-1}$. While for $U/t = 5.0$, ξ is small, such that the overlap between the surface states on opposite sides of the ribbon $\sim e^{-2N_y/\xi}$ is negligibile, for $U/t = 8.4$ this is only the case at larger N_y.

2.2.7 Discussion

The model proposed in Eq. (2.2.6) contains the most important ingredients for topological Kondo insulators. These are the spin-orbit coupling, which gives rise to a non-diagonal, momentum-dependent form factor, and the Hubbard interaction. As the results presented in the previous sections clearly show, this conceptually simple model yields a number of very interesting results. In particular, as discussed in Sec. 1.2.3.2, the presence of the lattice symmetry leads to distinct topological phases, the Γ-phase and M-phase. These phases differ in the parity eigenvalues at high-symmetry points in the Brillouin zone. This allows for driving the system through quantum phase transitions by tuning the interactions, from non-topological to topological states as well as between different topological phases. During the transitions, the bulk band gap has to close at some of the high-symmetry points. In the absence of time-reversal symmetry breaking, this is the only way that the corresponding parities can change.

By tracking the evolution of the bulk band gap, the adiabatical connection of the strongly renormalized Kondo insulator to the non-interacting topological insulator could be established. Hence, by appropriately tuning the parameters, the system can be driven smoothly into the strong coupling regime while retaining the topological properties. No phase transition, in particular no breaking of time-reversal symmetry takes place.

The adiabatical connection to the non-interacting, topologically non-trivial state is exploited in order to extend the definition of the topological invariant N_s to the case with interactions and finite temperatures. The data for this quantity at finite temperature allow to define a characteristic temperature scale T^* for the emergence of the topological state. By rescaling the temperature with T^*, the data for different values of the interaction parameter collapsed to a single curve. This suggests that T^* is a universal low-energy scale.

In fact, T^* is precisely the characteristic energy scale of the coherent Fermi liquid state, the coherence scale T_{coh}. Because of this relation, the topological properties can provide a convenient, independent way for accessing T_{coh}. This is of particular importance in the mixed valence regime, where different energy scales are of the same magnitude. In this case, extracting T_{coh} from other measures is not possible.

The tight locking of the two energy scales also means that the appearance of the topological surface states, which is observed in the spectral function, takes place at the same temperature as the onset of bulk coherence. Hence, in order for the surface states to emerge, the coherent quasiparticle bands have to be established. Therefore, with increasing renormalization of the quasiparticles in the bulk, which become heavy fermions, the appearance of the topological surface states is shifted to lower temperatures as well.

List of Figures

List of Tables

Bibliography

[1] G. Aeppli and Z. Fisk: *Kondo Insulators*. Comments on Condensed Matter Physics **16**, 155 (1992).

[2] V. Alexandrov, M. Dzero and P. Coleman: *Cubic Topological Kondo Insulators*. Physical Review Letters **111**, 226403 (2013).

[3] J. W. Allen, B. Batlogg and P. Wachter: *Large low-temperature Hall effect and resistivity in mixed-valent SmB6*. Physical Review B **20**, 4807 (1979).

[4] A. Altland and B. Simons: *Condensed Matter Field Theory*. Cambridge University Press (2006).

[5] P. W. Anderson: *Localized Magnetic States in Metals*. Physical Review **124**, 41 (1961).

[6] P. W. Anderson: *Basic Notions Of Condensed Matter Physics*. Benjamin/Cummings (1984).

[7] F. F. Assaad and H. G. Evertz: *World-line and Determinantal Quantum Monte Carlo Methods for Spins, Phonons and Electrons*. In H. Fehske, R. Schneider and A. Weiße (eds.): *Computational Many Particle Physics* vol. 739 of *Lecture Notes in Physics* p. 277. Springer 2008.

[8] P. Augustinský and J. Kuneš: *Improved Green's Function Measurement for Hybridization Expansion Quantum Monte Carlo*. Computer Physics Communications **184**, 2119 (2013).

[9] E. Bauer and M. Rotter: *Magnetism of complex metallic alloys: crystalline electric field effects*. Script for a lecture given at CMA Euroschool 2007.

[10] G. Baym: *Self-Consistent Approximations in Many-Body Systems*. Physical Review **127**, 1391 (1962).

[11] G. Baym and L. P. Kadanoff: *Conservation Laws and Correlation Functions*. Physical Review **124**, 287 (1961).

[12] K. S. D. Beach: *Identifying the maximum entropy method as a special limit of stochastic analytic continuation*. arxiv:cond-mat/0403055 (2004).

[13] K. S. D. Beach and F. F. Assaad: *Bilayer Hubbard model for 3He: a cluster dynamical mean-field calculation*. arxiv:0905.1127 (2009).

[14] K. S. D. Beach and F. F. Assaad: *Orbital-selective Mott Transition and Heavy-Fermion Behavior in a Bilayer Hubbard Model for 3He*. Physical Review B **83**, 045103 (2011).

[15] A. Benlagra and C. Pépin: *Model of Quantum Criticality in He3 Bilayers Adsorbed on Graphite*. Physical Review Letters **100**, 176401 (2008).

[16] A. Benlagra and C. Pépin: *He3 bilayers as a simple example of deconfinement*. Physical Review B **79**, 045112 (2009).

[17] B. A. Bernevig, T. L. Hughes and S.-C. Zhang: *Quantum Spin Hall Effect and Topological Phase Transition in HgTe Quantum Wells*. Science **314**, 1757 (2006).

[18] G. Biroli, O. Parcollet and G. Kotliar: *Cluster dynamical mean-field theories: Causality and classical limit*. Physical Review B **69**, 205108 (2004).

[19] J. C. Budich *et al.*: *Fluctuation-induced topological quantum phase transitions in quantum spin-Hall and anomalous-Hall insulators*. Physical Review B **86**, 201407 (2012).

[20] J. C. Budich and B. Trauzettel: *From the adiabatic theorem of quantum mechanics to topological states of matter*. Physical Status Solidi (RRL) **7**, 109 (2013).

[21] J. C. Budich, B. Trauzettel and G. Sangiovanni: *Fluctuation driven topological Hund insulator*. Physical Review B **87**, 235104 (2013).

[22] F. Chen *et al.*: *Coexistence of nontrivial two-dimensional surface state and trivial surface layer in Kondo insulator SmB6*. arxiv:1309.2378 (2013).

[23] K.-S. Chen, J. Werner and F. F. Assaad: *Optical conductivity of topological Kondo insulating states*. Physical Review B **90**, 115109 (2014).

[24] P. Coleman: *Introduction to Many Body Physics*. Cambridge University Press (2012).

[25] P. Coleman and A. H. Nevidomskyy: *Frustration and the Kondo Effect in Heavy Fermion Materials*. Journal of Low Temperature Physics **161**, 182 (2010).

[26] J. D. Denlinger *et al.*: *SmB6 Photoemission: Past and Present*. arxiv:1312.6636 (2013).

[27] J. D. Denlinger *et al.*: *Temperature Dependence of Linked Gap and Surface State Evolution in the Mixed Valent Topological Insulator SmB6*. arxiv:1312.6637 (2013).

[28] S. Doniach: *The Kondo lattice and weak antiferromagnetism*. Physica B **91**, 231 (1977).

[29] M. Dzero and V. Galitski: *A new exotic state in an old material: A tale of SmB6*. Journal of Experimental and Theoretical Physics **117**, 499–507 (2013).

[30] M. Dzero, K. Sun, P. Coleman and V. Galitski: *Theory of topological Kondo insulators*. Physical Review B **85**, 045130 (2012).

[31] M. Dzero, K. Sun, V. Galitski and P. Coleman: *Topological Kondo Insulators*. Physical Review Letters **104**, 106408 (2010).

[32] E. Frantzeskakis *et al.*: *Kondo hybridisation and the origin of metallic states at the (001) surface of SmB6*. Physical Review X **3**, 041024 (2013).

[33] L. Fu: *Topological Crystalline Insulators*. Physical Review Letters **106**, 106802 (2011).

[34] L. Fu and C. L. Kane: *Topological insulators with inversion symmetry*. Physical Review B **76**, 045302 (2007).

[35] S. Fuchs *et al.*: *Spectral properties of the three-dimensional Hubbard model*. Physical Review B **83**, 235113 (2011).

[36] S. Fuchs, T. Pruschke and M. Jarrell: *Analytic continuation of quantum Monte Carlo data by stochastic analytical inference*. Physical Review E **81**, 056701 (2010).

[37] A. Georges, G. Kotliar, W. Krauth and M. J. Rozenberg: *Dynamical mean-field theory of strongly correlated fermion systems and the limit of infinite dimensions.*. Reviews of Modern Physics **68**, 13 (1996).

[38] F. Goth, D. J. Luitz and F. F. Assaad: *Single magnetic impurities in the Kane-Mele model*. Physical Review B **88**, 075110 (2013).

[39] E. Gull *et al.*: *Continuous-time Monte Carlo methods for quantum impurity models*. Reviews of Modern Physics **83**, 349 (2011).

[40] E. Gull, P. Werner, A. J. Millis and M. Troyer: *Performance analysis of continuous-time solvers for quantum impurity models*. Physical Review B **76**, 235123 (2007).

[41] V. Gurarie: *Single-particle Green's functions and interacting topological insulators*. Physical Review B **83**, 085426 (2011).

[42] H. Hafermann, K. R. Patton and P. Werner: *Improved estimators for the self-energy and vertex function in hybridization-expansion continuous-time quantum Monte Carlo simulations*. Physical Review B **85**, 205106 (2012).

[43] M. Z. Hasan and C. L. Kane: *Colloquium: Topological insulators*. Reviews of Modern Physics **82**, 3045 (2010).

[44] K. Haule: *Quantum Monte Carlo impurity solver for cluster dynamical mean-field theory and electronic structure calculations with adjustable cluster base*. Physical Review B **75**, 155113 (2007).

[45] K. Haule and G. Kotliar: *Coherence–incoherence crossover in the normal state of iron oxypnictides and importance of Hund's rule coupling*. New Journal of Physics **11**, 025021 (2009).

[46] M. H. Hettler, M. Mukherjee, M. Jarrell and H. R. Krishnamurthy: *Dynamical cluster approximation: Nonlocal dynamics of correlated electron systems*. Physical Review B **61**, 12739 (2000).

[47] M. H. Hettler *et al.*: *Nonlocal dynamical correlations of strongly interacting electron systems*. Physical Review B **58**, 7475 (1998).

[48] A. C. Hewson: *The Kondo Problem to Heavy Fermions*. Cambridge Univ. Press (1997).

[49] M. Hohenadler and F. F. Assaad: *Correlation effects in two-dimensional topological insulators*. Journal of Physics: Condensed Matter **25**, 143201 (2013).

[50] M. Hohenadler, T. C. Lang and F. F. Assaad: *Correlation Effects in Quantum Spin-Hall Insulators: A Quantum Monte Carlo Study*. Physical Review Letters **106**, 100403 (2011).

[51] M. Hohenadler *et al.*: *Quantum phase transitions in the Kane-Mele-Hubbard model*. Physical Review B **85**, 115132 (2012).

[52] M. Hohenadler, F. Parisen Toldin, I. F. Herbut and F. F. Assaad: *Phase diagram of the Kane-Mele-Coulomb model*. arxiv:1407.2708 (2014).

[53] H. Ibach and H. Lüth: *Festkörperphysik*. Springer (2009).

[54] J. Jiang *et al.*: *Observation of possible topological in-gap surface states in the Kondo insulator SmB6 by photoemission*. Nature Communications **4**, 3010 (2013).

[55] V. Juričić, A. Mesaros, R.-J. Slager and J. Zaanen: *Universal Probes of Two-Dimensional Topological Insulators: Dislocation and π Flux*. Physical Review Letters **108**, 106403 (2012).

[56] C. L. Kane and E. J. Mele: *Quantum Spin Hall Effect in Graphene*. Physical Review Letters **95**, 226801 (2005).

[57] C. L. Kane and E. J. Mele: *Z2 Topological Order and the Quantum Spin Hall Effect*. Physical Review Letters **95**, 146802 (2005).

[58] D. J. Kim *et al.*: *Surface Hall Effect and Nonlocal Transport in SmB6: Evidence for Surface Conduction*. Scientific Reports **3**, 3150 (2013).

[59] D. J. Kim, J. Xia and Z. Fisk: *Topological surface state in the Kondo Insulator Samarium Hexaboride*. Nature Materials **13**, 466 (2014).

[60] T. Kita, T. Ohashi and N. Kawakami: *Mott transition in three-orbital Hubbard model with orbital splitting*. Physical Review B **84**, 195130 (2011).

[61] J. Kondo: *Resistance Minimum in Dilute Magnetic Alloys*. Progress in Theoretical Physics **32**, 37–49 (1964).

[62] M. König *et al.*: *Quantum Spin Hall Insulator State in HgTe Quantum Wells*. Science **318**, 766 (2007).

[63] G. Kotliar *et al.*: *Electronic structure calculations with dynamical mean-field theory*. Reviews of Modern Physics **78**, 865 (2006).

[64] G. Kotliar, S. Y. Savrasov, G. Pálsson and G. Biroli: *Cellular Dynamical Mean Field Approach to Strongly Correlated Systems*. Physical Review Letters **87**, 186401 (2001).

[65] A. M. Läuchli and P. Werner: *Krylov implementation of the hybridization expansion impurity solver and application to 5-orbital models*. Physical Review B **80**, 235117 (2009).

[66] M. Legner, A. Rüegg and M. Sigrist: *Topological invariants, surface states, and interaction-driven phase transitions in correlated Kondo insulators with cubic symmetry*. Physical Review B **89**, 085110 (2014).

[67] G. Li *et al.*: *Quantum oscillations in Kondo Insulator SmB6*. arxiv:1306.5221 (2013).

[68] F. Lu *et al.*: *Correlated Topological Insulators with Mixed Valence*. Physical Review Letters **110**, 096401 (2013).

[69] T. Maier, M. Jarrell, T. Pruschke and M. H. Hettler: *Quantum cluster theories.* Reviews of Modern Physics **77(3)**, 1027 (2005).

[70] C.-H. Min *et al.*: *Importance of Charge Fluctuations for the Topological Phase in SmB6.* Physical Review Letters **112**, 226402 (2014).

[71] H. Miyazaki *et al.*: *Momentum-dependent hybridization gap and dispersive in-gap state of the Kondo semiconductor SmB6.* Physical Review B **86**, 075105 (2012).

[72] M. Neumann *et al.*: *Magnetic Susceptibility of Heavy Fermion 3 He-Bilayers.* Journal of Low Temperature Physics **158**, 207 (2010).

[73] M. Neumann, J. Nyéki, B. Cowan and J. Saunders: *Bilayer ^{3}He: A Simple Two-Dimensional Heavy-Fermion System with Quantum Criticality.* Science **317**, 1356 (2007).

[74] M. Neupane *et al.*: *Surface electronic structure of the topological Kondo-insulator candidate correlated electron system SmB6.* Nature Communications **4**, 2991 (2013).

[75] P. Nozières and D. Pines: *The theory of quantum liquids.* Westview Press (1999).

[76] J. Otsuki, H. Kusunose and Y. Kuramoto: *Evolution of a Large Fermi Surface in the Kondo Lattice.* Physical Review Letters **102**, 017202 (2009).

[77] N. Parragh *et al.*: *Effective crystal field and Fermi surface topology: A comparison of d- and dp-orbital models.* Physical Review B **88**, 195116 (2013).

[78] N. Parragh, A. Toschi, K. Held and G. Sangiovanni: *Conserved quantities of SU(2)-invariant interactions for correlated fermions and the advantages for quantum Monte Carlo simulations.* Physical Review B **86**, 155158 (2012).

[79] E. Pavarini, E. Koch, F. Anders and M. Jarrell (eds.): *Correlated Electrons: From Models to Materials* vol. 2 of *Modeling and Simulation.* Verlag des Forschungszentrum Jülich (2012).

[80] M. Potthoff: *Self-energy-functional approach: Analytical results and the Mott-Hubbard transition.* European Physical Journal B **36**, 335 (2003).

[81] M. Potthoff: *Self-energy-functional approach to systems of correlated electrons.* European Physical Journal B **32**, 429 (2003).

[82] M. Potthoff: *Non-perturbative construction of the Luttinger-Ward functional.* Condensed Matter Physics **9**, 557 (2006).

[83] M. Potthoff, M. Aichhorn and C. Dahnken: *Variational Cluster Approach to Correlated Electron Systems in Low Dimensions*. Physical Review Letters **91**, 206402 (2003).

[84] M. Potthoff and W. Nolting: *Dynamical mean-field study of the Mott transition in thin films*. European Physical Journal B **8(4)**, 555 (1999).

[85] X.-L. Qi and S.-C. Zhang: *Topological insulators and superconductors*. Reviews of Modern Physics **83**, 1057 (2011).

[86] A. Rançon-Schweiger, A. Benlagra and C. Pépin: *Activation gap in the specific heat measurements for 3He bilayers*. Physical Review B **83**, 073102 (2011).

[87] P. S. Riseborough: *Heavy fermion semiconductors*. Advances in Physics **49**, 257 (2000).

[88] M. Roger, J. H. Hetherington and J.-M. Delrieu: *Magnetism in solid 3He*. Reviews of Modern Physics **55**, 1 (1983).

[89] A. Roth *et al.*: *Nonlocal Transport in the Quantum Spin Hall State*. Science **325**, 294 (2009).

[90] A. N. Rubtsov, M. I. Katsnelson and A. I. Lichtenstein: *Dual fermion approach to nonlocal correlations in the Hubbard model*. Physical Review B **77**, 033101 (2008).

[91] A. N. Rubtsov, V. V. Savkin and A. I. Lichtenstein: *Continuous-time quantum Monte Carlo method for fermions*. Physical Review B **72**, 035122 (2005).

[92] S. Rößler *et al.*: *Hybridization gap and Fano resonance in SmB6*. Proceedings of the National Academy of Sciences of the United States of America **111**, 4798 (2014).

[93] A. W. Sandvik: *Stochastic method for analytic continuation of quantum Monte Carlo data*. Physical Review B **57**, 10287 (1998).

[94] A. P. Schnyder, S. Ryu, A. Furusaki and A. W. W. Ludwig: *Classification of topological insulators and superconductors in three spatial dimensions*. Physical Review B **78**, 195125 (2008).

[95] P. Sémon, G. Sordi and A.-M. S. Tremblay: *Ergodicity of the hybridization-expansion Monte Carlo algorithm for broken-symmetry states*. Physical Review B **89**, 165113 (2014).

[96] Q. Si and S. Paschen: *Quantum phase transitions in heavy fermion metals and Kondo insulators*. Physica Status Solidi B **250**, 425 (2013).

[97] Q. Si and F. Steglich: *Heavy Fermions and Quantum Phase Transitions*. Science **329**, 1161 (2010).

[98] R. N. Silver, D. S. Sivia and J. E. Gubernatis: *Maximum-entropy method for analytic continuation of quantum Monte Carlo data*. Physical Review B **41**, 2380 (1990).

[99] R.-J. Slager, A. Mesaros, V. Juričić and J. Zaanen: *The space group classification of topological band insulators*. Nature Physics **9**, 98 (2013).

[100] J. L. Smith and Q. Si: *Spatial correlations in dynamical mean-field theory*. Physical Review B **61**, 5184 (2000).

[101] G. R. Stewart: *Heavy-fermion system*. Reviews of Modern Physics **56**, 755 (1984).

[102] P. Sémon, C.-H. Yee, K. Haule and A.-M. S. Tremblay: *Lazy skip lists, a new algorithm for fast hybridization-expansion quantum Monte Carlo*. arxiv:1403.7214 (2014).

[103] K. Takegahara, Y. Aoki and A. Yanase: *Slater-Koster tables for f electrons*. Journal of Phyics C: Solid State Physics **13**, 583 (1980).

[104] S. Thomas *et al.*: *Weak Antilocalization and Linear Magnetoresistance in The Surface State of SmB6*. arxiv:1307.4133 (2013).

[105] D. J. Thouless: *Exchange in solid 3He and the Heisenberg Hamiltonian*. Proceedings of the Physical Society **86**, 893 (1965).

[106] A. Toschi, A. A. Katanin and K. Held: *Dynamical vertex approximation: A step beyond dynamical mean-field theory*. Physical Review B **75**, 045118 (2007).

[107] M.-T. Tran, T. Takimoto and K.-S. Kim: *Phase diagram for a topological Kondo insulating system*. Physical Review B **85(12)**, 125128 (2012).

[108] M. Troyer and U.-J. Wiese: *Computational Complexity and Fundamental Limitations to Fermionic Quantum Monte Carlo Simulations*. Physical Review Letters **94**, 170201 (2005).

[109] M. Vojta: *Orbital-Selective Mott Transitions: Heavy Fermions and Beyond*. Journal of Low Temperature Physics **161**, 203 (2010).

[110] L. Wang, X. Dai and X. C. Xie: *Frequency domain winding number and interaction effect on topological insulators*. Physical Review B **84**, 205116 (2011).

[111] L. Wang, X. Dai and X. C. Xie: *Interaction-induced topological phase transition in the Bernevig-Hughes-Zhang model*. Europhysics Letters **98**, 57001 (2012).

[112] X. Wang *et al.*: *Antiferromagnetism and the gap of a Mott insulator: Results from analytic continuation of the self-energy*. Physical Review B **80**, 045101 (2009).

[113] Z. Wang, X.-L. Qi and S.-C. Zhang: *Topological Order Parameters for Interacting Topological Insulators*. Physical Review Letters **105**, 256803 (2010).

[114] Z. Wang and B. Yan: *Topological Hamiltonian as an Exact Tool for Topological Invariants*. Journal of Physics: Condensed Matter **25**, 155601 (2013).

[115] Z. Wang and S.-C. Zhang: *Simplified Topological Invariants for Interacting Insulators*. Physical Review X **2**, 031008 (2012).

[116] Z. Wang and S.-C. Zhang: *Strongly correlated topological superconductors and topological phase transitions via Green's function*. Physical Review B **86**, 165116 (2012).

[117] H. Weng *et al.*: *Topological Crystalline Kondo Insulator in Mixed Valence Ytterbium Borides*. Physical Review Letters **112**, 016403 (2014).

[118] P. Werner *et al.*: *Continuous-Time Solver for Quantum Impurity Models*. Physical Review Letters **97**, 076405 (2006).

[119] P. Werner, E. Gull, M. Troyer and A. J. Millis: *Spin Freezing Transition and Non-Fermi-Liquid Self-Energy in a Three-Orbital Model*. Physical Review Letters **101**, 166405 (2008).

[120] P. Werner and A. J. Millis: *Hybridization expansion impurity solver: General formulation and application to Kondo lattice and two-orbital models*. Physical Review B **74**, 155107 (2006).

[121] P. Werner and A. J. Millis: *Efficient Dynamical Mean Field Simulation of the Holstein-Hubbard Model*. Physical Review Letters **99**, 146404 (2007).

[122] P. Werner and A. J. Millis: *High-Spin to Low-Spin and Orbital Polarization Transitions in Multiorbital Mott Systems*. Physical Review Letters **99**, 126405 (2007).

[123] P. Werner and A. J. Millis: *Dynamical Screening in Correlated Electron Materials*. Physical Review Letters **104**, 146401 (2010).

[124] K. G. Wilson: *The renormalization group: Critical phenomena and the Kondo problem*. Reviews of Modern Physics **47**, 773 (1975).

[125] S. Wolgast *et al.*: *Low-temperature surface conduction in the Kondo insulator SmB*. Physical Review B **88**, 180405(R) (2013).

[126] N. Xu *et al.*: *Surface and bulk electronic structure of the strongly correlated system SmB6 and implications for a topological Kondo insulator*. Physical Review B **88**, 121102 (2013).

[127] S. J. Yamamoto and Q. Si: *Global Phase Diagram of the Kondo Lattice: From Heavy Fermion Metals to Kondo Insulators*. Journal of Low Temperature Physics **161**, 233 (2010).

[128] M. M. Yee *et al.*: *Imaging the Kondo Insulating Gap on SmB6*. arxiv:1308.1085 (2013).

[129] T. Yoshida, S. Fujimoto and N. Kawakami: *Correlation effects on a topological insulator at finite temperatures*. Physical Review B **85**, 125113 (2012).

[130] T. Yoshida, R. Peters, S. Fujimoto and N. Kawakami: *Topological antiferromagnetic phase in a correlated Bernevig-Hughes-Zhang model*. Physical Review B **87**, 085134 (2013).

[131] T. Yoshida, R. Peters, S. Fujimoto and N. Kawakami: *Topological phase in a two-dimensional metallic heavy-fermion system*. Physical Review B **87**, 165109 (2013).

[132] X. Zhang *et al.*: *Hybridization, Inter-Ion Correlation, and Surface States in the Kondo Insulator SmB6*. Physical Review X **3**, 011011 (2013).

[133] Z.-H. Zhu *et al.*: *Polarity-Driven Surface Metallicity in SmB6*. Physical Review Letters **111**, 216402 (2013).